A STUDY OF THE TARGET DETECTION CAPABILITIES OF AN AIRBORNE LIDAR BATHYMETRY SYSTEM

A Thesis
Presented to
The Academic Faculty

by

Domenic Anthony Carr

In Partial Fulfillment
of the Requirements for the Degree
Master of Science in the
School of Electrical and Computer Engineering

Georgia Institute of Technology
May 2013

A STUDY OF THE TARGET DETECTION CAPABILITIES OF AN AIRBORNE LIDAR BATHYMETRY SYSTEM

Approved by:

Dr. Gisele Bennett, Advisor
School of Electrical and Computer Engineering
Georgia Institute of Technology

Dr. Gregory Durgin
School of Electrical and Computer Engineering
Georgia Institute of Technology

Dr. Benjamin Klein
School of Electrical and Computer Engineering
Georgia Institute of Technology

Dr. Stephen Ralph
School of Electrical and Computer Engineering
Georgia Institute of Technology

Date Approved: March 14, 2013

ACKNOWLEDGEMENTS

First, I would like to thank my advisor, Dr. Gisele Bennett, for serving as my thesis advisor and for giving me the opportunity to work at EOSL. I have greatly enjoyed working at EOSL, a laboratory filled with exceptional colleagues and mentors. I appreciate all the time, effort, and support she has given me while at EOSL, providing me with every opportunity to pursue the research I enjoy. Having her support has undoubtedly opened new and exciting doors for my research moving forward.

Next, I would like to thank Dr. George Vachtsevanos, who assisted in getting me in contact with Dr. Bennett when I first visited Georgia Tech. His recommendation to Dr. Bennett on my behalf will never be forgotten.

I would also like to thank Dr. Grady Tuell, who served as my supervisor on the IRAD project. I appreciate his patience with me and allowing me to learn about and explore airborne lidar bathymetry while supporting his project.

I would like to thank Dave Roberts, who served as an invaluable mentor to me. I greatly appreciate all of our daily discussions on optics and lidar engineering, as his insights helped me learn and comprehend the material I was researching.

I would also like to thank all of my colleagues who assisted in the development of the data processing architecture. The combined product of all of our work will hopefully lead to greater opportunities at EOSL in the future.

I would like to thank Jason Zutty, a colleague of mine at EOSL, for shifting his work schedule forward to produce the target detection algorithm earlier in the design process and for his assistance in optimizing the algorithm's parameters.

I would like to say a very special thank you to Jennifer Hurt and Dr. Ed Clarkson, colleagues of mine at EOSL, for their assistance in integrating my simulation models with TMT. I sincerely appreciate their patience and effort, as they were extremely gracious with the time they devoted to helping me.

I would like to thank all of my family and friends for their support during my Master's studies. Every phone call, every conversation, and every visit helped keep me focused on achieving this degree.

I would like to thank my parents whom I love so dearly. They have contributed more than they will ever know to my advancement toward this degree. Their endless love and support drives me to places I never thought achievable. Their confidence in me motivates my successes and helps me stay the course when times are difficult. They have served as an inspiration my entire life, and without their support, I would not be the person I am today.

Finally, and most importantly, I would like to thank my Lord and Savior, Jesus Christ. Through Him all things are possible, and it is only through His blessings that I have been able to produce this document.

TABLE OF CONTENTS

LIST OF TABLES

LIST OF FIGURES

LIST OF SYMBOLS

β_π	Backscattering Coefficient
cm	Centimeter
dB	Decibel
GHz	Gigahertz
Gsamples/s OR Gs/s	Gigasamples per Second
J	Joule
K_d	Diffuse Attenuation Coefficient
m	Meter
mJ	Millijoule
mrad	Milliradian
μW	Microwatt
MW	Megawatt
Nd:YAG	Neodymium-doped Yttrium Aluminum Garnet
Nd:YVO_4	Neodymium-doped Yttrium Orthvanadate
nm	Nanometer
ns	Nanosecond
s	Second
sr	Steradian
W	Watt

LIST OF ABBREVIATIONS

A/D	Analog-to-Digital
ALB	Airborne Lidar Bathymetry
AOP	Apparent Optical Property
CHARTS	Combined Hydrographic and Rapid Total Surveyed
CZMIL	Coastal Zone Mapping and Imaging Lidar
DEM	Digital Elevation Model
ENVI	Environment for Visualizing Images
EO/ISR	Electro-Optical Intelligence, Surveillance, and Reconnaissance
EOSL	Electro-Optical Systems Laboratory
FOV	Field-of-View
FPGA	Field-Programmable Gate Array
FWHM	Full Width at Half Maximum
GPS	Global Positioning System
GTRI	Georgia Tech Research Institute
GUI	Graphical User Interface
IDL	Interactive Data Language
IHO	International Hydrographic Organization
IOP	Inherent Optical Property
IRAD	Internal Research and Development
MSE	Mean-squared Error
PMT	Photomultiplier Tube
PRR	Pulse Repetition Rate

RPM	Revolutions per Minute
SHOALS	Scanning Hydrographic Operational Airborne Lidar Surveys
SNR	Signal-to-Noise Ratio
TMT	Test Matrix Tool
USACE	United States Army Corps of Engineers
VSF	Volume Scattering Function
XML	Extensible Markup Language

SUMMARY

This work presents my research supporting GTRI's Electro-Optical Systems Laboratory (EOSL) Active EO/ISR Internal Research and Development (IRAD) project.

The first chapter provides background information on Airborne Lidar Bathymetry (ALB) theory and the state-of-the-art systems in existence today. I describe the important system and environmental considerations that affect ALB system design. Building upon that foundation, Chapter 2 presents my efforts in modeling an ALB system. I implemented code in Interactive Data Language (IDL) to simulate bathymetric waveforms produced by state-of-the-art systems, resulting in the development of EOSL's YellowJacketSimulator.

While implementing the theory presented in Chapter 2, I found predicting the signal loss arising from the scatter of transmitted energy out of the receiver's field-of-view (FOV) very time-consuming to compute. In order to overcome this computational challenge, I developed a proxy formulation for this FOV loss contribution as a function of the transmitted pulse's optical path length traveled in the water. Chapter 3 discusses this proxy formulation by detailing its derivation, accuracy, and expected applications.

Finally, Chapter 4 describes the theoretical experiments I performed to analyze an ALB system's target detection capabilities. I embedded the YellowJacketSimulator with my proxy formulation of the FOV loss factor into a testing framework that performed thousands of simulations based on different system, target, and environmental parameters. Using the results from these simulations, I describe the expected target

detection performance of an ALB system by detailing the trends in detection rate as functions of select system, target, and environmental parameters.

I conclude this work in Chapter 5 by summarizing my contributions and offering new directions for future research in ALB.

CHAPTER 1

INTRODUCTION

1.1 Problem Statement

The objective of my research was to characterize the target detection capabilities of an ALB system. Airborne lidar bathymetry is a method used to survey and map coastal and littoral zones. Along with extracting important information about the surveyed zone, such as soil and beach erosion or particle stratification, a fundamental requirement of these surveys is to detect underwater targets, hazards, or obstructions [1]. The ability to detect underwater targets depends on a target's dimensions, the depth and turbidity of the water, system and survey configuration, data processing capabilities, and algorithmic sophistication [1]. Understanding the effects of each of these factors on the performance of underwater target detection is essential in determining the target detection capabilities of a proposed ALB system.

1.2 Origin and History

Airborne Lidar Bathymetry has been used as an effective method of coastal mapping since the mid 1980's. ALB systems measure the depths of shallow, coastal waters from the air by employing a scanned, pulsed laser beam. Groups led by Gordon [2] and Guenther [3] pioneered the development of ALB theory and practice in the United States. These groups introduced the bathymetric lidar equation and explained the effects of different system and environmental factors on the returned waveform. In order to develop a practical system based on the radiometric equation, an understanding of the laser beam's extinction coefficient in water was paramount. Thus, these groups spent a great deal of time researching the optical properties of water that affect an ALB system's return signal.

Around the same time, groups led by Petzold [4], Dolin [5], and Kopelevich [6] published results on the effects of light-water interaction in various types of coastal waters. By gathering in-situ measurements of beam attenuation and spectral scattering and absorption, they began to formulate models for light-water interaction in coastal waters. Based on these models, they also began to derive the statistical interrelationships of coastal water's optical properties. Shortly thereafter, these groups developed methods to parameterize the volume scattering function (VSF) of water. The VSF of a body of water is an inherent optical property (IOP) of water that is an influential factor in determining the flux of radiation upwelling from the water surface [7]. By parameterizing the VSF of water, these groups enabled others performing remote sensing measurements of reflectance to solve the radiative transfer equation in coastal water. Furthermore, parameterization of the VSF allows for the extraction of other IOPs of the water based on a given estimate of the VSF. Presently, these parameterizations of the VSF, along with a parameterization proposed by Sokolov et. al [7], are the only parameterizations based on real measurements.

Successful ALB implementation is dependent on the optical properties of the surveyed water and optical detection systems. Optech International (referred to as Optech hereafter) utilized its expertise in ocean optics and detection systems in response to the United States Army Corps of Engineers (USACE) request to develop ALB surveying technology in the late 1980s. Optech became the leader in ALB with the introduction of its Scanning Hydrographic Operational Airborne Lidar Surveys (SHOALS) lidar [8]. SHOALS was designed for the purpose of accurately measuring water depths, but its capabilities extended to the estimation of seafloor reflectances and diffuse attenuation coefficients in coastal waters [9]. The SHOALS system was based upon the radiative transfer equation presented by Guenther [3], with minor variations accounting for field-of-view (FOV) constraints and pulse-stretching effects [10].

Furthermore, they adopted the Dolin [5] and Kopelevich [6] model of detecting the photons undergoing multiple-forward, single-backscattering processes in coastal water.

The requirements for the SHOALS bathymetric system were to have topographic and kinematic GPS capabilities, as well as seamless operation across land/water boundaries [8]. With these considerations in mind, SHOALS employed a diode-pumped Nd:YAG laser with an infrared output of 5mJ at 1064nm and a simultaneous, collinear, frequency-doubled green output of 5mJ at 532nm. The pulse-repetition rate was 400 pulses per second, and the green pulse width was approximately 7ns. The scan pattern was a segment of a circular arc directed 20 degrees in front of the path of the plane. The sampling frequency of the digitizer used was 1 GHz, and allowed for 10-bits of amplitude resolution. In terms of target detection capabilities, SHOALS was able to achieve 100% target detection of sub-meter objects, as small as 0.5 m in diameter, anywhere within the laser footprint and irrespective of their location in the water column [1]. Although SHOALS provided the first accurate, cost-effective ALB surveying method, accurate, shallow-water depth extraction was very difficult to achieve [11].

In the late 2000's Optech improved upon its SHOALS system by releasing the Coastal Zone Mapping and Imaging Lidar (CZMIL). CZMIL was designed to improve the airborne hydrographic and coastal mapping capabilities of the USACE and United States Navy by improving signal quality in the shallow, turbid water coastal zone without compromise of performance in deep water and to extend the utility of the collected data by developing algorithms and software to produce new environmental information [12]. CZMIL is a multi-sensor system based on the Combined Hydrographic and Rapid Total Surveyed (CHARTS) system developed by the Joint Airborne Lidar Bathymetric Technical Center of Expertise [13].

CZMIL achieved the goals outlined by the USACE and United States Navy by greatly improving the hardware characteristics of the system. CZMIL uses an active, Q-switched, Nd:YVO_4 laser that produces a frequency-doubled beam at 532nm with 3mJ

per pulse [14]. The pulse repetition rate is 10 kHz and the pulse width is under 2ns [14]. CZMIL utilizes a full-circular scan pattern operating at 27 Hz, fixed at an off-nadir angle of 20 degrees [15]. Finally, CZMIL uses nine channels of optical return data digitized by nine parallel 1GHz digitizers that have 10-bit amplitude resolution [16]. Developing and operating a system with these characteristics was far more advanced than had ever been achieved by an ALB system, allowing Optech to produce better data products at more cost-effective prices. Optech has yet to publish target detection capabilities for its CZMIL system, but it is safe to assume that they are at least as good as the capabilities SHOALS had. These characteristics, along with the new environmental information produced by CZMIL's sophisticated data processing algorithm, represent the state-of-the-art in ALB today.

1.3 Overview of Research

EOSL is producing the next generation bathymetric lidar system. To this end, EOSL secured funding for an IRAD project led by EOSL's Remote Sensing Division. Our goal is to develop a scalable ALB architecture, leading to a miniaturized, waveform-resolved, real-time system deployable on unmanned aerial vehicles. My contribution to the project is modeling the returned waveforms based on anticipated system and environmental conditions and developing real-time data processing algorithms that can generate 3D images of the seafloor.

The objective of my research is to characterize the target detection capabilities of a bathymetric lidar system. To accomplish this characterization, I performed a theoretical exploration of these capabilities by studying state-of-the-art ALB systems, researching light-water interaction, developing simulations and models of lidar system waveforms, and assisting in the design of our laboratory bathymetric lidar. By carrying out these tasks, I have developed a solid understanding of the target detection capabilities of an ALB system. My theory has contributed to the development of our group's data

processing algorithms, to the specifications of our laboratory lidar's transmitting and receiving optics, and to the design of the target detection experiments we will perform.

My first priority was to develop a software environment that could produce bathymetric return signals and perform data processing on those signals, as there was no previous infrastructure for modeling or analyzing bathymetric return signals at GTRI. Thus, my first task was to develop a waveform simulator that produced individual bathymetric return waveforms under various system and environmental scenarios. Understanding the radiometric transfer of energy in a bathymetric system was essential in developing a credible waveform simulator. Therefore, I performed a comprehensive study and research of ocean optics and light-water interaction. I focused a great deal of effort researching the published theories regarding light scattering and absorption in various coastal waters. Results published in [5], [6], and [7] provided good starting points in learning how the IOPs of water affect the bathymetric return signal. Understanding how to model the bathymetric return signal mathematically was essential in determining how data processing algorithms can estimate these properties from measured waveforms. Methods published in [9], [17], [18] and [19] provided results, insight, and lessons learned from developing the current, state-of-the-art simulators and extraction algorithms used in CZMIL, which I integrated into my own modeling software. Chapter 2 discusses my implementation of an ALB model in code and presents my software simulation environment, the YellowJacketSimulator.

While designing the YellowJacketSimulator, it became apparent that simulating one waveform by direct calculation of the analytical expression required too much time. In particular, the FOV loss factor term was the limiting factor, causing each simulation to take on the order of minutes to run to completion. Therefore, in order to reduce the computational intensity of simulating one waveform, I spent a great deal of time and effort researching ways to model the FOV loss factor in a novel way since no methods

had been published in literature. Chapter 3 discusses my efforts to empirically characterize the FOV loss factor term in the bathymetric lidar equation.

Finally, after developing the waveform simulator integrated with an empirically-modeled FOV loss factor, the next task was to create a tool that simulated an aircraft employing a circular scanning, pulsed laser system. This tool would provide the coordinate locations of each pulse on the water surface, allowing me to discern how many and which pulses in the scanning pattern would actually strike an underwater target. Since circular scanning patterns have a varying point density across the swath, this tool allowed me to calculate the projected number of pulses that would hit a target in a specific location for a given set of operating system parameters (e.g. off-nadir angle, aircraft height, pulse repetition rate, etc.). As mentioned in the problem statement, the ability to detect underwater targets depends on a target's dimensions, the depth and turbidity of the water, system and survey configuration, data processing capabilities, and algorithmic sophistication [1]. Thus, combining the waveform simulator, which effectively produces the results of a single laser-pulse event, with the scanning simulator, which effectively produces the results due to a sequence of pulses, allowed me to simulate the theoretical results produced by an ALB system employing a scanned, pulsed surveying configuration. Since this configuration is exactly what state-of-the-art ALB systems employ, the theoretical results I produced should be similar to those produced by the systems.

To produce a large and representative data set for all of the various combinations of system, environmental, and target inputs, I leveraged the power of EOSL's Test Matrix Tool (TMT), a software-testing environment that runs on EOSL's cluster network. Using TMT, I produced tens of thousands of runs of my software corresponding to the cross-product of all possible combinations of input parameters. Since I can control micro-level properties of the simulation (i.e. waveform-to-waveform properties) with the waveform simulator and macro-level properties of the simulation (i.e. properties of scanning

pattern) with the scanning simulator, I could vary all of the interesting parameters concerning target detection from within TMT. In other words, upon setting ranges for target, environmental, and system operating variables, TMT simulated every input combination within the ranges specified. Then, using TMT's analysis graphical user interface (GUI), I was able to analyze the effects of variations in each of these variables on the ability of a state-of-the-art ALB system to detect an underwater target. Chapter 4 contains the results I obtained from TMT with all of my associated analysis and insight.

CHAPTER 2

THE MODELING AND IMPLEMENTATION OF AIRBORNE LIDAR BATHYMETRY RETURN SIGNALS IN IDL

ALB systems, like radar or active sonar systems, measure a backscattered, return signal following the transmission of a known signal. The transmitted signal for ALB systems is a high-energy, blue-green laser pulse, which, after interacting with the surveyed water, produces a backscattered return signal that the airborne receiver partially captures. Whereas radar or sonar systems measure the time difference between signal transmission and signal reception to estimate the distance between the transmitting location and the backscattering object's location, ALB systems measure the time difference between two returns, the sea-surface return and the seafloor return, to estimate the surveyed water's depth. To understand the interaction of the transmitted pulse with the surveyed environment, the bathymetric lidar equation, analogous to the radar equation, describes the radiometric transfer of energy for a single pulse-firing event. When thought of in a peak power sense, this equation describes the power received by a system's receiver after the transmitted pulse interacts with the surveyed environment. Interestingly, the bathymetric lidar equation is actually an impulse response function, meaning Linear Systems theory can be applied to treat it as a transfer function. Therefore, the convolution of this equation with the pulse shape function and environmentally induced, pulse-stretching functions ultimately produces the detected bathymetric return signal. In order to design and optimize ALB systems, it is necessary to have a thorough understanding of the true bathymetric return signal and how various system and environmental factors affect it. To this end, I implemented a model of the radiometric transfer of energy from an ALB system's transmitter to its receiver in

Interactive Data Language (IDL) code, culminating in my creation of the YellowJacketSimulator, a software platform that simulates ALB system return signals.

2.1 System Architecture

ALB systems consist of a laser transmitter and its associated transmitting optics, a scanning mechanism, a receiver telescope and its associated receiving optics, a photon detector, a waveform digitizer, and a real time signal processor. These instruments and devices are all integrated into an aircraft flying approximately 400 meters above the water surface. The system's survey area depends on the scanning mechanism's off-nadir angle and the altitude of the aircraft, but is typically between 200 to 300 meters in diameter [3]. The laser transmitter, being pulsed at some kilohertz frequency, samples the surveyed area of the water surface in a fixed pattern set by the scanning mechanism. For each transmitted pulse, the receiving optics detect photons returned within the telescope's FOV after their interaction with the water. The waveform digitizer digitizes the output of the photon detector, typically a photo-multiplier tube, and sends its output to the real-time signal processor, which extracts important information from each waveform. Figure 2.1 shows the surveying configuration for the CZMIL system.

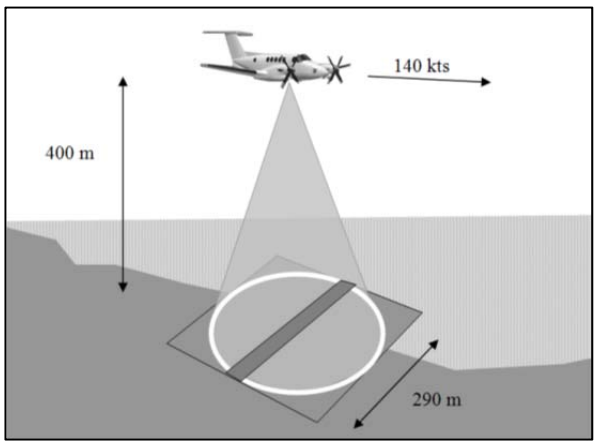

Figure 2.1: ALB Surveying Configuration with Transmit Beam Fixed at 20° off-nadir angle incidence [15]

2.1.1 Transmitter and Transmitting Optics

The spatial and temporal performance characteristics of the laser transmitter and its associated optics are paramount in the deployment of a successful ALB system. High spatial and temporal data resolution requirements for these systems drive the need for high energy, short pulse, and high repetition rate laser transmitters [14]. Moreover, each pulse must be extremely repeatable, both spatially and temporally, within small tolerance intervals. Typical pulse repetition rates are on the order of 1kHz, with temporal extent of less than 2ns and with average energy on the order of 1mJ per pulse. This means that the peak power per pulse approaches the order of $1x10^{-3}J / 1x10^{-9}s = 1x10^{6}$ W, or 1 MW. This type of power is necessary due to the very small fraction of backscattered signal actually captured by the receiver and due to the laser beam extinction characteristics in coastal seawater. The diffuse attenuation coefficient, K_d, an apparent optical property (AOP) of water, dictates a pulse's exponential decay through the water column in correspondence with the Beer-Lambert Law. To mitigate the transmitted pulse's exponential decay in seawater and to ensure maximum depth penetration, ALB systems employ laser transmitters of wavelength 532nm, which roughly corresponds to the spectral minimum of K_d for coastal seawater, as shown in Figure 2.2.

Fortunately, developing a laser transmitter of wavelength 532nm is fairly straightforward, as this wavelength corresponds to a frequency-doubled 1064nm wavelength, which is produced by common Nd:YAG lasers. Optech's SHOALS ALB system employed such a laser as its transmitter. However, to meet the aforementioned sub-2ns pulse requirements, today's state-of-the-art ALB laser transmitter in the CZMIL system uses Nd:YVO_4 as the laser gain medium, since it is the only crystal that provides sufficient gain under CZMIL's operating conditions [14]. Nd:YVO_4 can provide sufficient gain because it has a larger stimulated emission cross-section at 1064nm and a higher absorption coefficient and wider absorption bandwidth at the pump wavelengths,

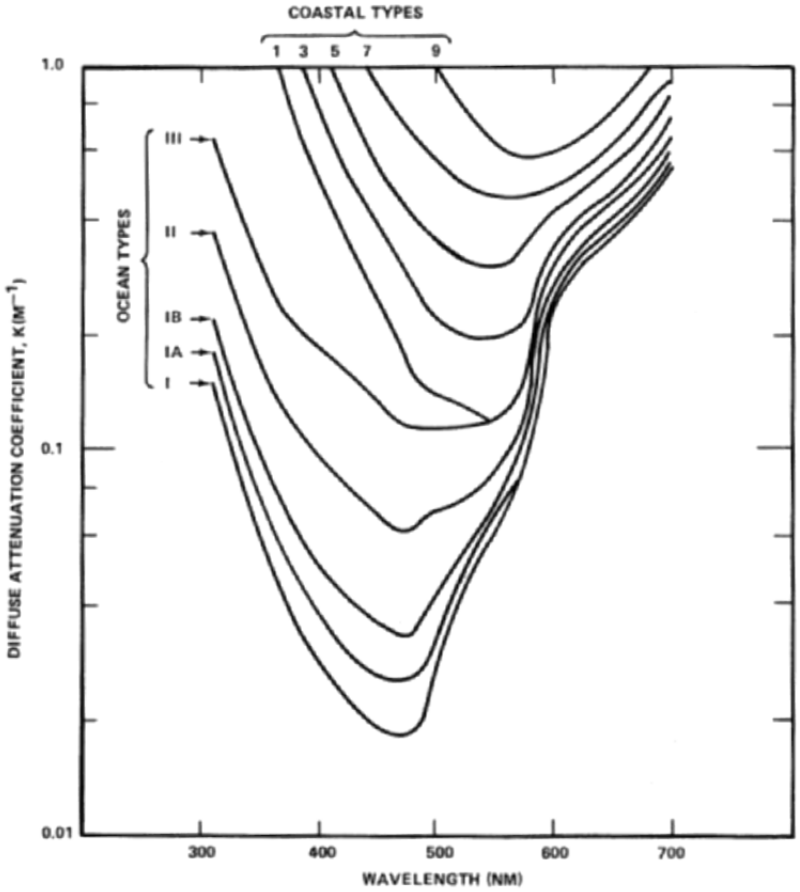

Figure 2.2: Spectral Dependence of the Diffuse Attenuation Coefficient [21] (re-published in [3])

as compared to Nd:YAG [20]. In addition to the second-harmonic generating crystal that produces the required frequency-doubled wavelength, the other optics necessary for the transmitter to produce laser pulses of extremely reproducible distributions of spatial and temporal energy are combinations of mirrors, fibers, oscillators, isolators, and amplifiers. CZMIL uses both a Gaussian temporal and spatial energy distribution in order to facilitate detection of the returning pulse using its segmented detector design [14]. Pulse spot size on the water surface is typically 2-3 meters in diameter, which helps ensure close to 100% surface and seafloor illumination.

2.1.2 Scanning Mechanism

The scanning mechanism is responsible for keeping the laser transmitter at a fixed angle off the nadir while scanning the survey area in a repeated pattern. The main performance considerations that the scanning mechanism must account for are the area survey-rate, the spatial density of pulses on the water surface, and depth penetration [15]. The system parameters that affect these performance metrics are the scanner's RPM, the laser's pulse repetition rate (PRR), the off-nadir angle, and the overlap between successive scans. To illustrate the tradeoffs for some of these system parameters, consider an attempt to increase the number of pulses that strike the sea's surface per unit area (defined as the lidar's point density). This could be achieved by increasing the laser's PRR or the scanner's RPM. However, increasing the PRR decreases the maximum depth penetration, due to lower energy per pulse, while increasing the scanner's RPM decreases the scanner's expected lifetime, due to wear on the scanner's bearing [15]. Another attempt to increase the point density could be to decrease the distance between successive scans (i.e. increase the overlap between scans), but this results in longer flight times to survey the area, which is more expensive.

Scanning mechanisms typically use a fixed angle off the nadir between 15 to 20 degrees for survey patterns [3][15]. This is done in order to mitigate the return signal from the water surface, as seen in Figure 2.3, thereby increasing the maximum depth potential. Scanning patterns vary from forward-looking, arc patterns, which scan back and forth on the front arc of the forward-pointing scanner, or circular scanners, which scan an entire circle beneath and about the aircraft. Figure 2.4 shows both types of scanning patterns. SHOALS used a forward-looking, arc scanner, while CZMIL uses a circular scanner, which provides greater coverage and point density, at the cost of higher complexity in design. Circular scanning mechanisms also introduce non-uniform point densities across the swath. Deciding how to handle this non-uniformity is an important consideration in target detection applications, as discussed in Chapter 4.

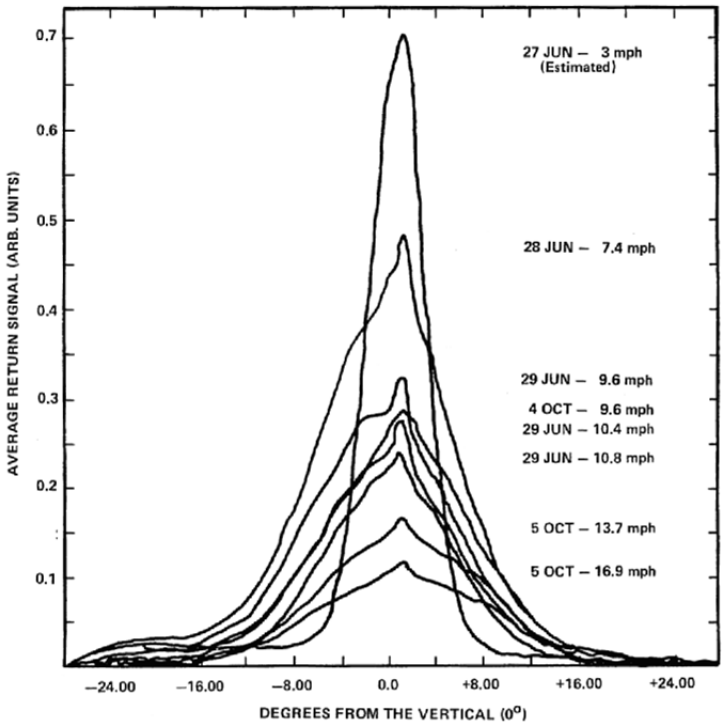

Figure 2.3: Return Signal from Water Surface vs. Off-Nadir Angle [22] (re-published in [3])

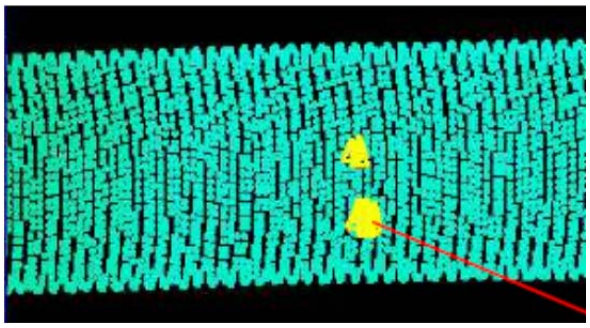

Figure 2.4 (a): ALB System Forward-Looking, Arc Scanning Pattern [1]

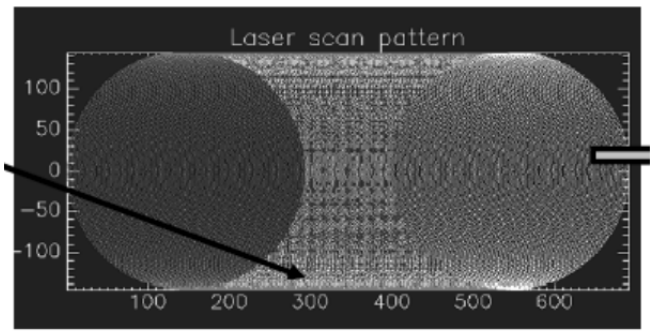

Figure 2.4 (b): ALB System Circular Scanning Pattern [15]

2.1.3 Receiver Telescope, Receiving Optics, & Photon Detection

The receiver and the corresponding receiving optics are responsible for capturing returned signal photons and converting them to electric current. The main performance considerations for these devices are the number of photons captured by the receiver, the efficiency in converting the captured photons to electrons, the ability for the receiver to discriminate signal photons from photons of similar wavelength from spurious sources, and to have an overall short system response [3][16]. The receiver aperture and FOV are important system parameters that greatly affect the detected signal, as will be discussed at length shortly. What is important to note here, however, is that the receiver FOV must encompass a large enough portion of the reflected upwelling energy from the seafloor in order to detect the maximum possible water depth [3][23]. Common FOV values range from 20-80 mrad.

The efficiency in converting the captured photons to electrons, or the optical efficiency of the receiving optics, encompasses the mirror reflectances, the quantum efficiency of the detector, and the transmission characteristics of the narrow-band filter used to suppress noise. Often, ALB systems employ multiple-mirror systems, and if the reflectance of these mirrors is not sufficiently high, significant photon loss occurs. The detector is typically a photo-multiplier tube (PMT), in order to boost the weak return signal from bathymetric measurements and to improve SNR; PMT's in use today have quantum efficiencies on the order of 0.2. Finally, the narrow-band filter, whose purpose is to suppress background noise from the sun's reflection off the ocean, usually has a transmission coefficient of around 0.5. Therefore, typical receivers have optical efficiency values around 0.1 or smaller, resulting from the multiplication of each of these factors. Another important consideration for the receiver is for the PMT response time to be as short as possible, in order to help reduce the overall system response time, allowing for depth extraction in very shallow waters [16].

2.1.4 Waveform Digitizer and Real Time Signal Processing

The waveform digitizer and real time signal processor are responsible for digitizing the returned waveform data and reducing the recorded data to a manageable amount. The main performance considerations for these devices are high-speed and high-resolution [16]. Typical sampling rates are pushing 2 gigasamples per second, and each analog-to-digital (A/D) converter encodes 10-bit amplitude resolution [16]. When considering that CZMIL uses 9 parallel, analog input channels, each with its own A/D converter sampling at 1 Gsamples/s during a 8000 ns interval at 10,000 times per second (the repetition rate of the laser transmitter), it is clear that the volume of data captured per second is enormous [16]. Therefore, real time electronics, such as field-programmable gate array (FPGA) electronics must be used to reduce the volume of data passed to the bus and onto digital storage media. By using properties of the return waveform and by understanding the geometry of the surveying configuration, methods such as range gating, packetization, and feature extraction can be used to decimate the data, while keeping only that which is necessary [3][16]. Furthermore, to perform real time depth extraction or seafloor reflectance estimation, algorithms for waveform-smoothing, such as Savitzky-Golay filtering, and peak detection, such as inflection point-based techniques, must be implemented on the FPGA. All of these events must be carefully synchronized with the laser transmitter and the scanning mechanism in order to work properly.

2.2 The Impulse Response Function

The bathymetric lidar equation expresses the radiative transfer of energy during interaction with the environment after pulse transmission by the laser transmitter until pulse reception by the airborne receiver. It uses the small-angle scattering approximation for radiation transfer, resulting in the community-accepted multiple-forward scattering, single-backscattering model [3][10][24]. The equation accounts for the various system,

environmental, and geometric parameters that affect the bathymetric return signal. It is expressed in literature in various ways, but the most common forms of the equation are shown in Equations 2-1 [17][18] and 2-2 [3][10][24].

$$I(t) = S_o \cdot Z(H,h) \cdot F(h,FOV)\,, \quad t \geq \frac{2H}{v} + 2T \tag{2-1}$$

where,

$I(t)$	is the received optical power at time t
S_o	is the near surface return signal
$Z(H,h)$	is the system attenuation factor
$F(h,FOV)$	is the FOV loss factor
h	is the water depth
H	is the aircraft altitude
T	is the emitted pulse duration

$$P_r = \frac{(m)P_t\eta\rho F_p A_r cos^2(\theta)}{\pi(n_w H+D)^2} e^{-2n(s,\omega_o,\theta)KDsec(\varphi)} \tag{2-2}$$

where,

P_r	is the received optical peak power
P_t	is the transmitted optical peak power
D	is the water depth
H	is the aircraft altitude
ρ	is the reflectance at the laser wavelength
K	is the diffuse attenuation coefficient
θ	is the off-nadir transmit angle
φ	is the refracted beam angle in water
η	is the optical efficiency of the receiving optics
n_w	is the refractive index of water
F_p	is the FOV loss factor
A_r	is the aperture area of the receiver optics
m	is an empirical scaling factor that accounts for air path loss and system detuning
$n(s,\omega_o,\theta)$	is a pulse stretching factor
s	is the scattering coefficient
ω_o	is the single-scattering albedo
F_p	is the FOV loss factor

These equations are equivalent as I will show in the following subsections, and, as Guenther details in [3], are actually impulse response functions. I discuss the implications of this important fact on waveform modeling in Section 2.3.

2.2.1 Propagation Geometry

The geometric characteristics of the transmitted pulse's propagation path play a critical role in the shape and magnitude of the detected return signal. Figure 2.5 shows a well-accepted propagation model for a single laser pulse traveling through the water column. As mentioned earlier, the scanning mechanism of an ALB system holds the

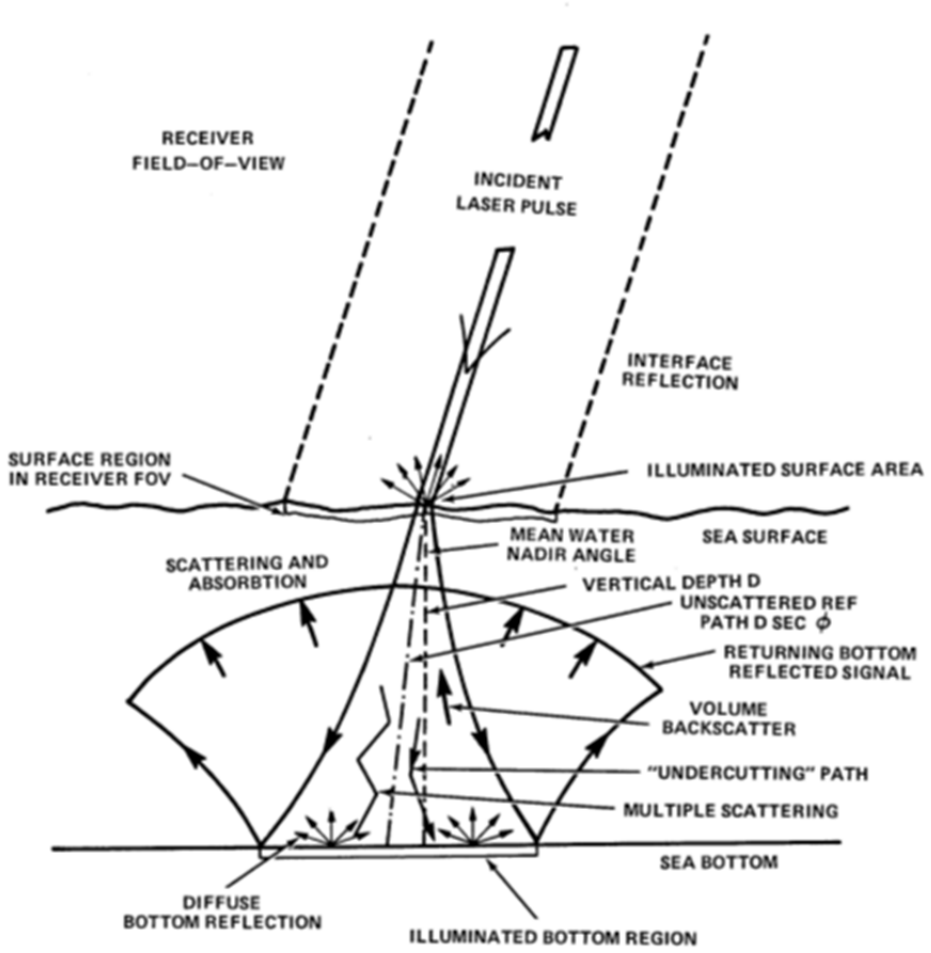

Figure 2.5: Propagation Geometry of a Single Pulse through the Water Column [3]

laser transmitter at a fixed off-nadir angle (Figure 2.1) to mitigate the surface return signal. This off-nadir angle is equal to the angle at which the pulse enters the water with respect to the vertical. Upon reaching the air-water interface, part of the pulse is reflected (assumed to be Lambertian), while the transmitted portion of the pulse is refracted, bending toward the normal, in accordance with Snell's Law. Under typical system characteristics with an off-nadir angle of 20˚, $n_{air} = 1$, and $n_{water} = 1.33$, the angle of refraction into the water is approximately 15˚, and the reflected and transmitted portions of the pulse are 2% and 98%, respectively. Thus, for a water depth D, a pulse will travel $D/cos(\varphi)$, or $Dsec(\varphi)$, to reach the bottom. This distance is referred to as the optical path length traveled in the water, or optical depth.

Once the pulse begins propagation in the water column, it obeys the Beer-Lambert Law for extinction within a medium. The attenuation, or extinction, coefficient, in seawater is the diffuse attenuation coefficient, usually represented by K or K_d. The reason why the diffuse attenuation coefficient is the extinction coefficient that appears in the exponential decay terms as opposed to the beam attenuation coefficient (an IOP of water) is because the receiver FOV accepts returning light from paths other than the principal ray. Put another way, since the pulse is reflected diffusely at any given point in the water column and the receiver FOV is large enough to detect rays of light that travel on different paths to the receiver, the diffuse attenuation coefficient is what determines the pulse's exponential decay in seawater. Being an AOP of water, the diffuse attenuation coefficient varies as a function of the incident radiance distribution [3]. Therefore, measurements of K_d will vary on cloudy days versus clear days. Furthermore, even on clear days, the value of K_d varies as a function of solar zenith angle [3].

Now, discussing the particle nature of light as it relates to photon traversal of the water column, photons are multiply scattered as they propagate in the water column. The multiple scattering of photons results in the beam spreading into an ever-expanding cone of light as the pulse propagates toward the seafloor. This phenomenon has unofficially

been coined as "Gary's Trumpet", in deference to Gary Guenther who detailed this effect in [3]. The spread of the beam of light, or trumpet, is dependent on the volume scattering function (VSF) of the surveyed seawater. For more turbid waters, the cone of light expands faster and wider, while for clearer waters, the cone of light expands more slowly and is smaller. A useful first-order approximation is that the cone of light expands as a function of half of the optical depth [1], although this has been shown to be an overestimate in clearer and optically shallower waters [1][25].

Once the pulse, extended into a wider beam due to multiple scattering, reaches the seafloor, it diffusely reflects upward in all directions. This reflection, like the sea-surface reflection, is assumed to be Lambertian [3]. Typical reflectance values vary from 0.02 to 0.2, depending on the composition of the seafloor, with 0.2 corresponding to a sandy, bright seafloor. Since the pulse extends into a wider beam as the optical depth increases, bottom returns demonstrate considerable dispersive effects, due to the increased difference in optical path lengths traveled [3][10][17][18][24]. These temporal stretching effects will be discussed in section 2.3. Then, to first-order, the only portion of the light reflected from the seafloor that will actually return to the receiver is that which travels upward along the same path on which it traveled downward [2]. This is due to optical reciprocity principles, which require that for photons to exit the water and refract back toward the airborne receiver, the collections of paths on which photons travel downward must be the same as the collection of paths on which photons travel upward as they return. Thus, from this argument, the effective spot size of light on the water surface that will actually refract back toward the airborne receiver is the autoconvolution of the pulse's spot size on the seafloor [3]. It is ultimately this consideration that sets the receiver's minimum FOV requirement, as the receiver's FOV must encompass an area at least the size of this effective spot size to capture the entire bottom-reflected pulse.

2.2.2 The Near Surface Return Signal

The near surface return signal is denoted by S_o in Equation 2-1. It can be expressed as seen in Equation 2-3 [17].

$$S_o = \frac{P_o \eta \beta_\pi \left(1-\rho^{fr}\right)^2 e^{-2\tau_a} A_{rec} cos^2(\theta)}{\pi (H n_w)^2} \tag{2-3}$$

where,

P_o	is the peak power transmitted
η	is the optical efficiency of the receiving optics
β_π	is the backscattering coefficient
ρ^{fr}	is the Fresnel reflectance at the air-water boundary
τ_a	is the optical thickness of the air
A_{rec}	is the aperture area of the receiver optics
θ	is the off-nadir transmit angle
H	is the aircraft altitude
n_w	is the refractive index of water

Most of the terms that appear in Equation 2-3 are rather self-explanatory and follow directly from simple radiative transfer theory. However, it is important to mention the origin of the term $A_{rec}cos^2(\theta)/\pi(Hn_w)^2$. Essentially, this term arises from the ratio of the solid angle subtended by the airborne receiver from an altitude H to the effective solid angle of the reflected pulse that just passes through the water surface and is reflected back out immediately. The solid angle subtended by the airborne receiver from an altitude H can be expressed as $A_{rec}cos^2(\theta)/\mathrm{H}^2$. Then, the solid angle of the reflected pulse is π, due to the Lambertian reflectance. However, the water index of refraction must be taken into account at the air-water boundary, which results in a factor of n_w^2 increase. Therefore, the effective solid angle of the reflected pulse above the air-water boundary is πn_w^2. Taking the ratio of these two solid angles results in $(A_{rec}cos^2(\theta)/\mathrm{H}^2)/ (\pi\, n_w^2)$, or $A_{rec}cos^2(\theta)/\pi(Hn_w)^2$.

2.2.3 The System Attenuation Factor

The system attenuation factor is the term *Z(H,h)* that appears in Equation 2-1. It can be expressed as seen in Equation 2-4 [17].

$$Z(H,h) = \frac{e^{-2K_d hsec(\varphi)}}{\left(1+\frac{hsec(\varphi)}{n_w Hsec(\theta)}\right)^2} \tag{2-4}$$

where,

K_d	is the diffuse attenuation coefficient or, $a + b_b$
a	is the water's absorption coefficient
b_b	is the water's backward scattering coefficient
h	is the true (current) water depth
H	is the aircraft altitude
φ	is the refracted beam angle in water
θ	is the off-nadir transmit angle
n_w	is the refractive index of water

The numerator of Equation 2-4 is simply the Beer-Lambert Law, taking into account the round trip propagation distance (hence the 2) corrected for optical path length (using $1/cos\varphi = sec\varphi$). The terms in the denominator are related to the denominator of Equation 2-3. Consider the same type of argument as made in the previous sub-section, but in this case we take the ratio of the solid angle subtended by the airborne receiver at a true depth h in the water, to the solid angle of the reflected pulse. The numerator of this ratio would be $A_{rec}/(\mathrm{H}/\cos(\theta) + h/\cos(\varphi))^2$, which can be rewritten as $A_{rec}/(Hsec(\theta) + hsec(\varphi))^2$. As before, the denominator of the ratio is the solid angle of the reflected pulse, which is the Lambertian reflectance corrected for the refraction through the air-water interface, πn_w^2. Taking the ratio of these two terms results in the expression $A_{rec}/\pi n_w^2(Hsec(\theta) + hsec(\varphi))^2$. After removing the contribution of the near surface return, which is $A_{rec}/\pi n_w^2\ (Hsec(\theta))^2$, we arrive at the following expression $(1 + hsec(\varphi)/n_w Hsec(\theta))^2$ in the denominator, which is equivalent to the denominator of Equation 2-4. Thus, the terms in the denominator of Equation 2-4 are simply those

leftover from the ratio of solid angles after grouping the original expression into separate contributions.

2.2.4 The Field of View Loss Factor

The FOV loss factor is denoted by $F(h, FOV)$ in Equation 2-1 and F_p in Equation 2-2. It is a very complicated expression that depends on many parameters of the system and environment in a complex way, as can be seen in Equations 2-5, 2-6, 2-7, and 2-8 [17][18][27].

$$F(h,FOV) = \frac{1}{2}\Psi^2 e^{-2b_f h sec(\varphi)} \int_0^{\infty} [x + \sqrt{1+x^2}]^{\frac{2b_f h sec(\varphi)}{x}} \times \exp\left[\frac{-x^2 m^2}{4}(r_0^2 + R_0^2 + \Theta^2 + \Psi^2)\right] x dx \quad (2\text{-}5)$$

$$\Theta = \frac{DIV}{2}\gamma \; ; \quad \Psi = \frac{FOV}{2}\gamma \; ; \; \gamma = \frac{Hsec(\theta)}{hsec(\varphi)} + \frac{1}{n_w} \quad (2\text{-}6;\ 2\text{-}7;\ 2\text{-}8)$$

where,

b_f	is the water's forward scattering coefficient
h	is the true (current) water depth
H	is the aircraft altitude
φ	is the refracted beam angle in water
θ	is the off-nadir transmit angle
n_w	is the refractive index of water
m	is the water type optical index [17]
r_o	is the radius of the initial beam cross-section
R_o	is the radius of the receiver aperture
FOV	is the field-of-view of the receiver
DIV	is the divergence of the transmitted pulse

I will discuss this function at length in Chapter 3, when I provide an empirical characterization of the function, so I will not provide much discussion here regarding the terms that appear in it. However, it is important to note that this FOV loss function depends on the VSF of the surveyed water. Since the VSF of water is an IOP, it is very difficult to calculate, and many groups rely on estimates or models of the VSF in order to calculate the FOV loss function. During my research, I came across a few

parameterizations of seawater's VSF based on real measurements [4][5][6][7]. After attempting to use the most recent parameterization presented in [7], I found that it did not behave as properly as the parameterization presented in [6] did. Therefore, I decided to use the model proposed by Kopelevich [6], the same parameterization that the designers of CZMIL use.

2.2.5 Equivalency of Expressions

Upon substituting Equations 2-3, 2-4, and 2-5 into Equation 2-1, we arrive at the following expression:

$$\frac{P_o \eta \beta_\pi \left(1-\rho^{fr}\right)^2 e^{-2\tau_a} A_{rec} cos^2(\theta)}{\pi (H n_w)^2} \frac{e^{-2K_d hsec(\varphi)}}{\left(1+\frac{hsec(\varphi)}{n_w H sec(\theta)}\right)^2} F(h, FOV) \tag{2-9}$$

Using the approximation that $A_{rec}/(Hsec(\theta) + hsec(\varphi))^2 \cong A_{rec}cos^2(\theta)/\pi(n_w H + D)^2$ for practical parameter values [1] and substituting into 2-9, we arrive at Equation 2-10.

$$\frac{P_o \eta \beta_\pi \left(1-\rho^{fr}\right)^2 e^{-2\tau_a} A_{rec} cos^2(\theta)}{\pi \left(n_w H+D\right)^2} e^{-2K_d hsec(\varphi)} F(h, FOV) \tag{2-10}$$

Finally, noting that the empirical scaling factor, m, in Equation 2-2 takes into account the air path loss and system detuning (i.e. m $\cong \left(1-\rho^{fr}\right)^2 e^{-2\tau_a}$), treating the empirically-derived, pulse-stretching, $n(s, \omega_o, \theta)$, from the exponential decay term of Equation 2-2 as part of the FOV loss function (i.e. to make $F_p \cong F(h, FOV)$) and understanding that β_π is simply ρ^{fr} at the water surface and ρ at the seafloor, we arrive at the equivalency of Equations 2-1 and 2-2.

2.3 The Bathymetric Return Signal

The bathymetric lidar equation, Equations 2-1 and 2-2, presented in section 2.2 is an impulse response function. Therefore, we can apply Linear Systems theory to treat it as a transfer function when modeling it as a system. This means that the output of the system, or the signal we detect, is (to first-order) the convolution of our input with the impulse response function. Therefore, convolving our transmitted pulse's temporal shape with the impulse response function produces the detected return signal. Guenther termed this result the environmental response function [3], but I will simply refer to it as the bathymetric return signal. In order to make our black-box model more accurate and representative of the true system, we need to take into account any other transfer functions in addition to the impulse response function that lie between our input and output. Figure 2.6 shows the several other transfer functions that affect the bathymetric return signal, including the surface-stretching transfer function, the seafloor-stretching transfer function, and the electronic system's transfer function (including the detector's response) [19]. Using the fact that we can treat transfer functions in series as one overall transfer function by convolving the individual transfer functions, the bathymetric return signal detected by the airborne receiver is the sequential convolution of our laser pulse shape with the individual transfer functions.

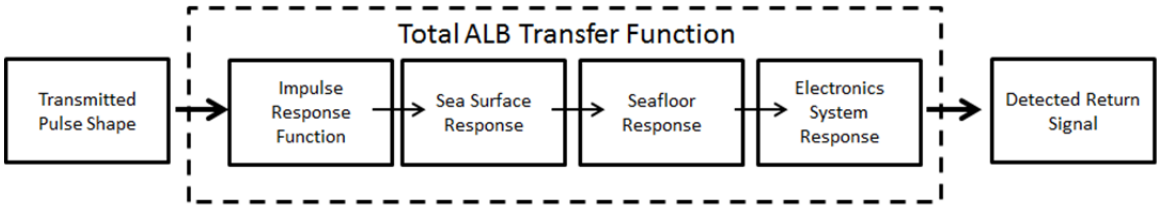

Figure 2.6: A Model of the ALB Transfer Function

2.3.1 Pulse Shape

The temporal pulse shape of the transmitted laser system is the input to my convolution-based model. The temporal extent of a typical pulse used in state-of-the-art

ALB systems is under 2ns, as measured between the full-width half-maximum (FWHM) points. The temporal profile of the transmitted pulse used in the CZMIL system can be seen in Figure 2.7. For my modeling purposes, I simply use a Gaussian pulse shape as the input, with its peak value and FWHM as variable parameters.

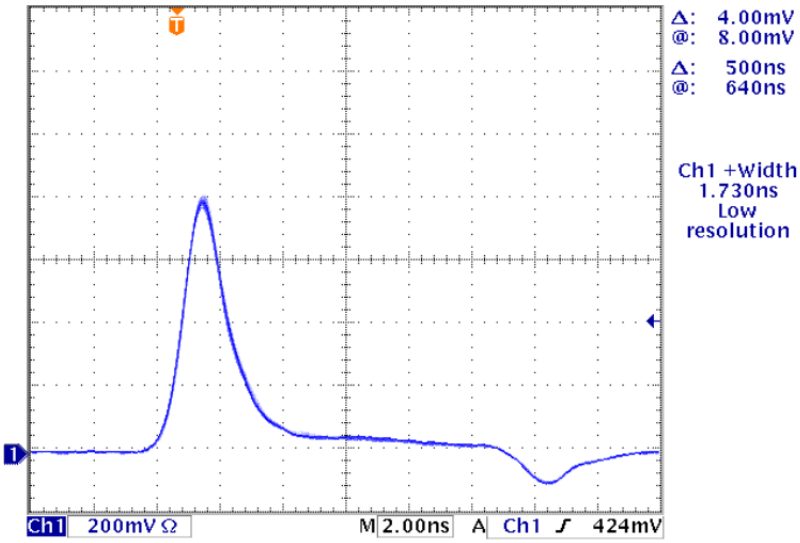

Figure 2.7: Temporal Profile of CZMIL's Transmitted Pulse [14]

The temporal characteristics of the pulse are not the only ones that affect the bathymetric return signal. In fact, the spatial distribution of energy in the beam plays an important role in determining how much energy is actually backscattered as well. When thinking of the water column as a stacked collection of infinitesimally small layers of water, each with its own spatial distribution of backscattering coefficients, β_π, the two-dimensional spatial convolution of the energy profile with the backscattering coefficient distribution in a given layer is actually the total fraction of pulse being backscattered at that given layer. Since real systems use a two-dimensional Gaussian distribution of energy (e.g. CZMIL, Figure 2.8) or a somewhat Super-Gaussian distribution of energy, the true portion of backscattered pulse at a given depth is this Gaussian profile convolved with the β_π distribution at that depth.

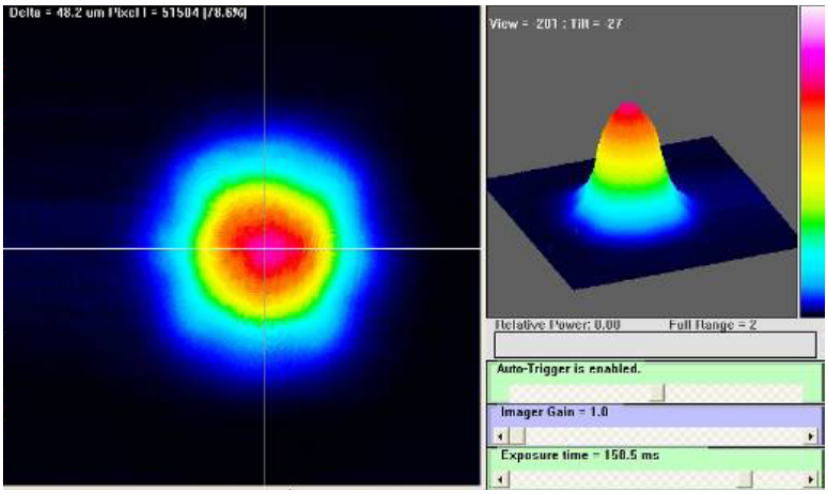

Figure 2.8 The 2-D Spatial Beam Profile used by the CZMIL system [14] – Red represents strongest intensity while blue represents weakest intensity.

To simplify my waveform simulator, I modeled the spatial distribution of energy as a top-hat, or uniform across the beam, and zero elsewhere. This greatly reduced the difficulty of implementing the simulator, as I no longer needed to perform successive 2-D spatial convolutions in conjunction with the temporal convolution to determine the true backscatter. Using the top-hat approximation for the spatial distribution of energy, while in reality is not true, provides an accurate enough input to first- or second-order.

2.3.2 Surface-Stretching Effects

The interaction of the pulse with the air-water interface is a transfer function that must be taken into account in order to produce an accurate waveform. This interaction results in a pulse-stretching effect as a consequence of the surveying configuration's geometry. Consider a 2-ns pulse, which has a spatial extent of approximately 60cm in the propagating direction. Since the pulse travels at an angle of 20˚ off-nadir, as it enters the water only the leading edge of the pulse closest to the water begins its interaction with the water. As the beam continues to pass through the interface, part of the pulse has already been refracted into the water, while some of it remains above the water. In order

to maintain continuity of the pulse across the boundary using electromagnetic theory, the wavefronts must bend across the air-water boundary (Figure 2.9).

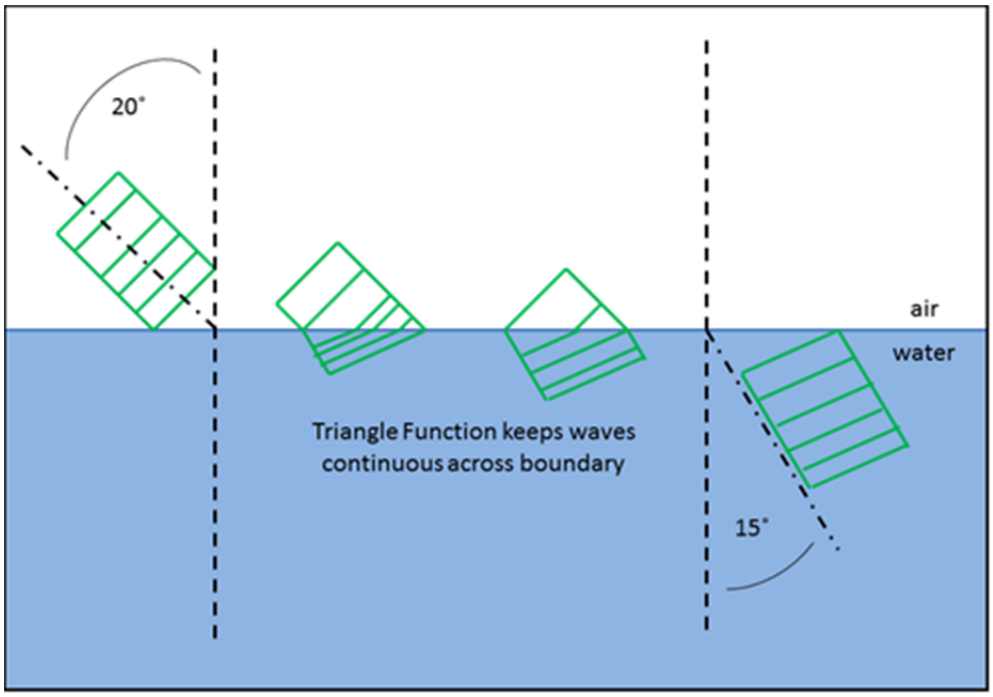

Figure 2.9: Pulse Stretching at Air-Water Boundary

Thus, the effective pulse-stretching behavior can be modeled by a triangle function. The only parameter of this triangle function that has to be determined is its temporal extent, which can be calculated by determining the time difference between the time the leading edge of the pulse hits the interface and the time the trailing edge of the pulse hits the interface. Assuming a circular pulse beam diameter D, Equation 2-11 can be used to calculate the effective temporal extent of the geometric-induced, pulse stretching at the water surface.

$$t_{stretch} = \frac{ct_{pulse} + w_{beam}\tan(\theta)}{c} \tag{2-11}$$

where,

c	is the speed of light
t_{pulse}	is the full-width, half-max of the pulse

w_{beam} is the beam diameter
θ is the off-nadir transmit angle

2.3.3 Seafloor-Stretching Effects

Reflection at the seafloor also induces stretching effects on the pulse [17]. Because the airborne detector can detect photons that have traveled on multiple paths, those photons that are reflected back toward the receiver by locations farthest away from the principal ray will take the longest to arrive. Therefore, there is an effective pulse-stretch in the return waveform due to the differing arrival times of photons reflected from the seafloor. My current simulator does not yet use a convolution to describe this process. Instead, I assume an idealized return from the seafloor over a longer interaction interval to model the seafloor-stretching behavior. This is a reasonable approximation, but in reality, this is not what occurs. Thus, I need to develop a depth-dependent convolution that takes into account the increase in reflection-induced dispersion from deeper seafloor returns.

2.3.4 Electronic System Response

Once the backscattered photons return to the airborne receiver, it is the job of the receiver optics to convert the incident radiation to electrical current. This process can be thought of as the electronics system's response. The electronics system's response is comprised of three separate impulse response functions: (1) the impulse response of the detector; (2), the impulse response of the signal amplifier; and, (3) the impulse response of the digitizer [6]. In my waveform simulator, I treat the impulse response of the PMT and the transimpedance amplifier as one stage. In this stage, the detected optical power is converted to the corresponding number of incident photons. Then, converting all of these photons to electrons (recall that I have already taken the quantum efficiency of the PMT into account in the optical efficiency factor) and multiplying this value by the PMT's gain, I determine the anode current. This current feeds into the transimpedance amplifier,

producing the detected output voltage, whose magnitude is the feedback resistor multiplied by the current. Finally, for the digitizer impulse response, I model it by a comb function sampling the detected voltage at the digitizer's sampling rate, and then I quantize the values into discrete amplitude bins based on the amplitude resolution of the desired digitizer. Currently, I do not include any of the temporal stretching effects in my simulator from either of these devices, though this occurs in reality. As I continue to improve the simulator by adding new features to it, including stretch factors due to these components will certainly be at the top of the list. Once our group proceeds to characterize and test our devices, I will have a better understanding of these components' responses.

2.3.5 The Resulting Observed Signal

By combining the material presented in the previous sub-sections, the true bathymetric lidar transfer function is simply the convolution of the impulse response function with the surface-stretching function, the seafloor-stretching function, and the electronics system's response function (Equation 2-12). Therefore, the resulting (noiseless) signal detected by the airborne receiver, is the convolution of the laser pulse shape (I_{laser}) with this overall transfer function, expressed in Equation 2-13.

$$H_{total} = H_{irf} * H_{surface} * H_{seafloor} * H_{electronics} \tag{2-12}$$

where,

H_{irf}	is the impulse response function (Equations 2-2 & 2-3)
$H_{surface}$	is the transfer function of the air-water interface
$H_{seafloor}$	is the transfer function of the seafloor
$H_{electronics}$	is the total transfer function of all the system's electronics

$$P_{observed} = I_{laser} * H_{total} \tag{2-13}$$

2.3.6 Noise Sources

There are several sources of noise that affect ALB systems, three of which are discussed in this section. The first source of noise is due to solar background. Some of the sun's radiation reflects off of the sea surface and happens to fall within the accepted wavelengths of the narrow-band filter [3][17][26], thus our system will detect these photons. Solar background noise appears as a randomly fluctuating signal in the optical domain with some average, which essentially sets a noise floor for the system. A typical value for the solar irradiance reflected from the water column is 0.02 W^2/m^2-nm-sr, which, for standard operating parameters, results in an average background noise of 0.7μW. This value does not include solar glint off waves, which would also add to the noise. My waveform simulator currently uses this value as an additive noise in Equation 2-13.

A second source of noise is the non-uniformity in the water column itself. Equations 2-2 and 2-3 both assume constant IOPs and AOPs for a given water column. However, in reality, the particle concentration changes as the photons travel through the water, meaning that the effective backscattering coefficient, β_π, changes as a function of depth. In the detected return signal, this noise appears as a non-smooth exponential decay during volume backscatter. In other words, the exponential decay is very jittery between the surface and bottom returns. To model this behavior in my simulator, I use an average β_π value, and then randomly generate normally distributed β_π values that the pulse interacts with as it traverses the water column. For more noise in the water column, I can increase the standard deviation of the β_π distribution; for less noise in the water column, I can decrease the standard deviation of the β_π distribution.

Finally, the electronics used in the receiver introduces another source of noise, which appears in the electrical domain. These noise sources include thermal, dark, and shot noise. Currently my waveform simulator assumes shot noise from the PMT as the dominant noise mechanism. I model this noise using Poisson statistics. First, by using

the specifications provided in our Hamamatsu 9880U PMTs, I calculate the square root of the anode's current in each time bin, which serves the variance of the noise current for that time bin. Then, I generate a normal distribution and use a random number generator to select the number of standard deviations the noise at a given time bin should be. Upon scaling the noise current vector by these randomly generated numbers, I then add each bin with its corresponding anode current value to produce the total current produced from the PMT. One noise condition I do not yet take into account for the PMT is the after-effects of saturating the device due to a very large signal, which introduces spurious signals for a few time bins thereafter [1]. A situation like this could arise due to solar glint on the water surface reflecting back a very strong interface return. Such a scenario could cause inaccurate waveforms and false depth measurements, but I view this as a detail that I do not need to account for yet.

2.4 The YellowJacketSimulator

After building up the radiometric models to simulate the detected return power from a single, pulse-firing event in IDL, I then proceeded to design a GUI that would serve as a nice, front-end visualization tool for the simulated bathymetric return signals. The GUI would provide the capability of dynamically displaying return signals in both the optical and electrical domains based on all of the system and environmental parameters that affect a bathymetric return signal. Having this capability is a staple of leading ALB groups, marked by Optech's use of Ocean Scientific [28], and later WaveSim [19], to predict ALB system performance. I created a software package in IDL called the YellowJacketSimulator, which is the combination of my GUI and radiometric modeling code. The YellowJacketSimulator follows in the same approach as Ocean Scientific and WaveSim in that it attempts to estimate the effectiveness of an ALB system under different operating conditions, both system and environmental. I based the

design of my simulator on the examples of Ocean Scientific and WaveSim provided in ALB literature [19][28].

Figure 2.10 shows a screenshot of the YellowJacketSimulator at startup. Currently, it is a simple, one-window GUI. The window is laid out such that there is one plotting display in the upper-left corner, while the input controls appear in text boxes on the right of the display. The input parameters are partitioned into five groups: receiver properties,

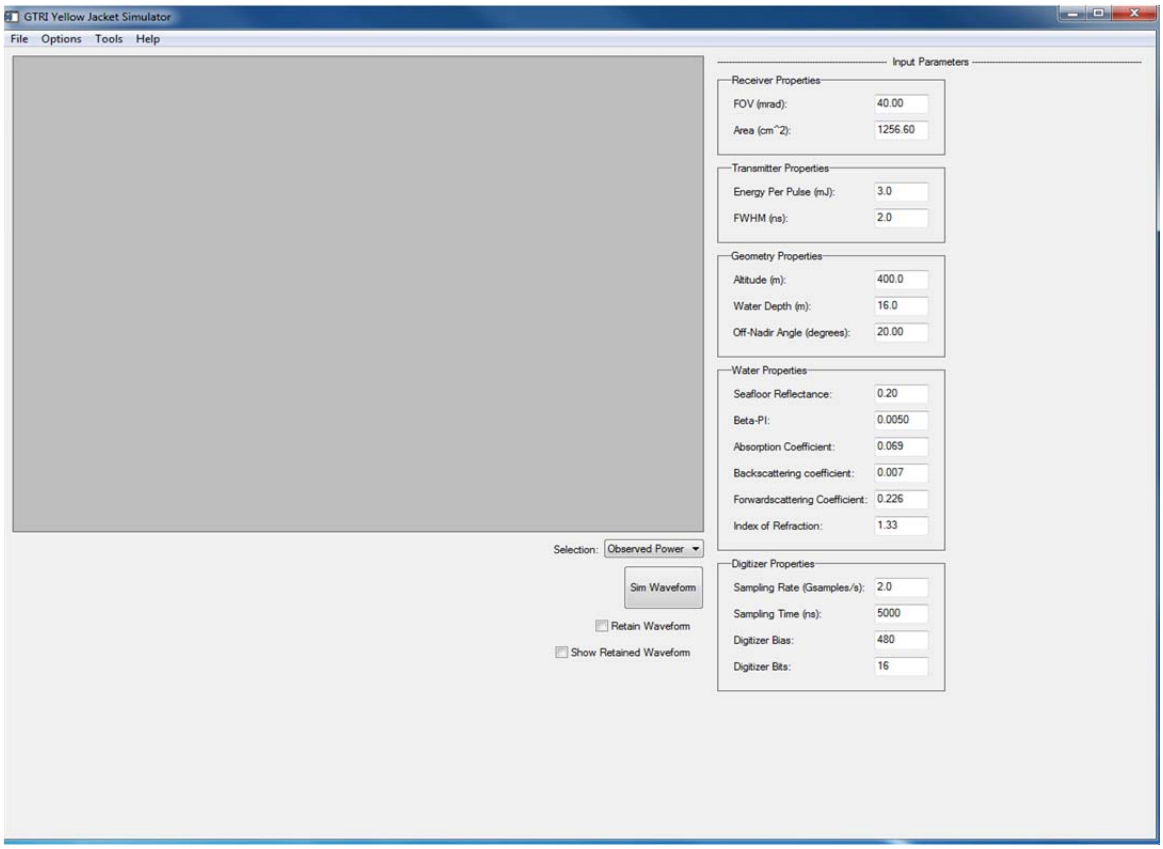

Figure 2.10: The YellowJacketSimulator GUI

transmitter properties, geometry properties, water properties, and digitizer properties. Beneath the plotting display, the “Sim Waveform” button simulates a return waveform based on all of the values entered in the text boxes at the time the user pushes the button. The plotting display will show either the observed power incident on the receiver or the

electronic output of the digitizer, depending on the user's choice of "Selection", the dropdown box beneath the plotting display. Finally, the checkboxes "retain waveform" and "show retained waveform" provide the user the ability to save and compare waveforms of different parameter values. Figures A.1 through A.3 in the Appendix demonstrate the stated capabilities of the GUI by showing waveforms of various inputs parameters plotted in the plotting window of the GUI. There is plenty of room for improvement with the GUI, which will be discussed in Section 5.2, Future Work, but the important things I considered when developing it was to keep its design flexible for future growth while simultaneously demonstrating an acceptable proof-of-concept.

CHAPTER 3

AN EMPIRICAL CHARACTERIZATION OF THE FIELD-OF-VIEW LOSS FACTOR IN THE BATHYMETRIC LIDAR EQUATION

The FOV loss factor in the Bathymetric Lidar Equation is a consequence of the multiple-forward-single-backscattering processes that describe photon traversal of the water column. It arises due to photons being forward scattered multiple times, ultimately redirecting them outside of the airborne receiver's FOV. Assuming a sufficient receiver FOV to capture the cross-section of the transmitted beam on the water surface, the FOV loss factor does not result in significant loss of received optical power at shallower depths. Conversely, the FOV loss factor does result in large losses at larger depths, thereby affecting the maximum detectable water depth by an ALB system. In lieu of an efficient method to calculate the FOV loss factor using the analytical formula, I developed a method to characterize the FOV loss factor empirically, reducing the analytical formula to a collection of ten coefficients for a given FOV. These ten coefficients completely describe the FOV loss function over FOVs ranging from 20 mrad to 55 mrad, over coastal waters ranging from K_d 0.05 m^{-1} to 0.16 m^{-1}, and for depths up to 30 meters. A transfer function representation of this model is shown in Figure 3.1. The

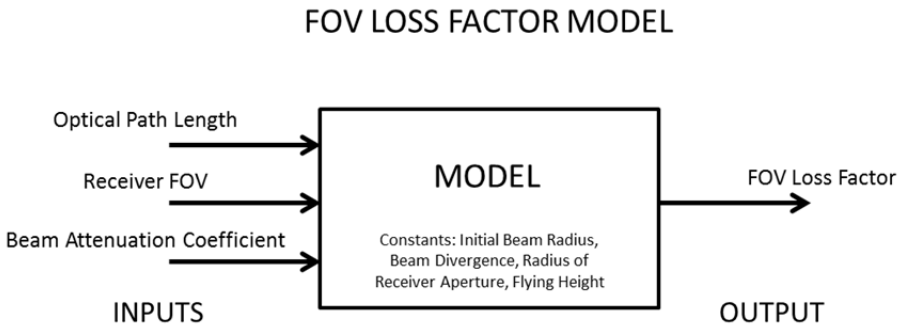

Figure 3.1: Transfer function representation of the proposed FOV loss factor model

method used to characterize the FOV loss function can be extended to a wider range of FOVs, K_d values, and depths; thus, this method can be used in the future as an efficient and effective way to estimate the FOV loss factor for a given ALB system.

3.1 Motivation

The FOV loss factor in the Bathymetric Lidar Equation has a complicated analytical formula that varies as a function of the inherent optical properties of the surveyed water, the water depth, the field of view of the airborne receiver, the radius of the receiver aperture, the flying altitude of the survey, the initial diameter of the transmitted laser beam, and the divergence of the transmitted laser beam [26]. It is a difficult formula from which to derive meaningful insights into how the FOV loss factor changes as a function of one of the above variables. More importantly, however, is that direct computation of the FOV loss factor from the analytical formula is extremely computationally intensive and cannot be performed in real time. The consequences of this are two-fold: (1) it severely limits the ability to design a bathymetric lidar system efficiently and effectively, as simulations of return waveforms based on the radiative transfer require too much time for practical use in the design process; and, (2) it prohibits estimating seafloor reflectance values in real time.

An explicit method for calculating this function does not exist in the literature concerning the modeling of airborne lidar bathymetry (ALB) return signals [3][17][19][26]. While it is possible that state-of-the-art ALB system designers compute the modeled return waveform using a direct computation of the analytical formula, it is far more likely that look-up-tables of FOV loss factor functions have been generated, thereby rendering real-time calculation of the function unnecessary. However, this method is inherently cumbersome and does not allow for flexibility in the design process, as the designer is limited to the pre-generated FOV loss functions, which have fixed input

parameters. Having the ability to alter the input parameters to the FOV loss function and viewing real time estimates of the change in received optical power would provide the engineer another knob to adjust in the design process and would be a significant contribution to the field of ALB. In order to accomplish this goal, a model of the FOV loss factor as a less complicated and less computationally intensive function must be generated, simultaneously maintaining the integrity of the analytical formula. This section explains the model I developed, detailing its derivation and expected accuracy, and discusses future implications of using such a technique to model the FOV loss factor.

3.2 Introduction

The Bathymetric Lidar Equation, first proposed in [4], can be expressed as seen below in Equation 3-1 [17]:

$$I(t) = S_o \cdot Z(H,h) \cdot F(h,FOV),\ t \geq \frac{2H}{v} + 2T \tag{3-1}$$

where,

$I(t)$	is the received optical power at time t
S_o	is the near surface return signal
$Z(H,h)$	is the straightforward attenuation factor
$F(h,FOV)$	is the FOV loss factor
h	is the water depth
H	is the aircraft altitude
T	is the emitted pulse duration

To elucidate the contributions of each of these terms on the total optical power returned to the receiver, this chapter will use Equation 3-2 to describe the total received optical power at time t, along with relations 3-3 through 3-8. These equations can be derived by rearranging and algebraically manipulating Equations 2-3, 2-4, and 2-5.

$$P(2t,FOV) = S(t) \cdot \hat{Z}(t) \cdot \hat{F}(t,FOV),\ t > t_0 \tag{3-2}$$

$$S(t) = \frac{P_0 \eta \beta_\pi (1-\rho)^2 e^{-2\tau_a} A_{rec} cos^2(\theta)}{\pi\left(Hn_w + v(t-t_0)\cos(\varphi)\right)^2} \tag{3-3}$$

$$\hat{Z}(t) = e^{-2K_d v(t-t_0)} \tag{3-4}$$

$$\hat{F}(t, FOV) = \frac{1}{2}\Psi^2 e^{-2b_f v(t-t_0)} \int_0^\infty [x + \sqrt{1+x^2}]^{\frac{2b_f v(t-t_0)}{x}} \times \exp\left[\frac{-x^2 m^2}{4}(r_0^2 + R_0^2 + \Theta^2 + \Psi^2)\right] x dx \tag{3-5}$$

$$\Theta = \frac{DIV}{2}\gamma \; ; \qquad \Psi = \frac{FOV}{2}\gamma \; ; \quad \gamma = \frac{H}{v(t-t_0)} + \frac{1}{n_w} \tag{3-6; 3-7; 3-8}$$

where,

t_0	is the time the pulse hits the water
P_0	is the peak transmitted pulse power
η	is the optical conversion efficiency
β_π	is the backscattering coefficient
ρ	is the surface reflectance
τ_a	is the optical thickness of air
A_{rec}	is the area of the receiver aperture
θ	is the off-nadir angle in air
φ	is the refracted off-nadir angle in water
H	is the flying altitude of the aircraft
n_w	is the index of refraction of water
v	is the velocity of the pulse in water
K_d	is the diffuse attenuation coefficient
FOV	is the field of view of the receiver
DIV	is the divergence of the transmitted pulse
m	is the water type optical index [17]
r_0	is the radius of initial beam cross-section
R_0	is the radius of the receiver aperture
b_f	is the forward scattering coefficient in water

Although these equations can seem rather daunting at first glance, upon closer examination they are rather straightforward. *S(t)* describes the return signal due to reflection and backscattering at a given time t, while accounting for the reduction in solid angle subtended by the airborne receiver as the pulse travels farther away from the aircraft (deeper into the water). $\hat{Z}(t)$ is simply Beer-Lambert's Law, accounting for the

round-trip exponential decay in optical signal through the water column. Finally, $\hat{F}$, the subject of this chapter, is the FOV loss factor. The multiplication of these three terms results in the optical return signal at time *2t* (complete round trip time), *P(2t,FOV)*, produced by bathymetric lidar systems.

S(t), the backscattering contribution, is very straightforward to implement in code. It consists mainly of constants, most of which are known before runtime, as they are direct consequences of system parameters. The only values that change are the independent variable, t, which is a function of the system's sampling rate, and the backscattering coefficient, β_π. β_π depends on the composition of particles in the water [17] (i.e. the number of large particles versus the number of small particles). Since the pulse interacts with different compositions of particles as it moves through the water column, the β_π value changes as a function of time. To remove the explicit time dependence, we can assume a homogeneous water column [17], that is, a well-mixed water profile, and therefore treat the β_π values as normally distributed with some spread about an average β_π value. Hence, simulated values of β_π as the pulse propagates through the water can be generated extremely quickly by simply specifying a mean and

$\hat{Z}(t)$, the attenuation contribution, is also very straightforward to implement in code, as it is simply an exponential decay term as a function of time. Thus, using the vector of elapsed time values (the same one used to calculate the backscattering contribution) as the independent variable in Equation 3-4 will produce a vector of attenuation values during pulse propagation in the water. The only real concern with this factor is the accuracy of the diffuse attenuation coefficient, K_d, value, as it is an apparent optical property of water [3]. However, for modeling purposes, it can be treated as the sum of the absorption and backward scattering coefficients of the water [17]. This modeled parameter is called the system attenuation coefficient value, K_{sys}. Finally, it is important to note here that the receiver FOV does have an impact on K_{sys}[3][21][29]. For wider FOVs, the system attenuation coefficient value approaches the diffuse attenuation

coefficient. As the receiver FOV is decreased, the diffuse attenuation coefficient approaches the beam attenuation coefficient value, c, which is an inherent optical property of water. In the limit where the FOV becomes infinitesimally small and only detects photons that travel on the principal ray path, K_{sys} will be the beam attenuation coefficient. Equation 3-9 summarizes the relationship between K_d, K_{sys}, and c. For

$$K_d \leq K_{sys} \leq c \tag{3-9}$$

future work dealing with the effects of decreasing the receiver FOV on ALB systems, the interrelationship between FOV and the attenuation factor's contribution will be an important consideration.

$\hat{F}(t, FOV)$, the FOV loss factor, is not nearly as straightforward to implement in code as the previous two functions. In fact, depending on the language of implementation, it can be very awkward to calculate. To begin, the independent variable appears both inside and outside of the integral. Thus, the integral evaluated out to infinity must be calculated for every time value in the independent variable vector. The total number of integrations that must be performed is rather large, as one might as expect, because the time it takes the pulse to reach the seafloor at common depths is around 90 nanoseconds and typical time step values are sub-nanosecond. Therefore, performing approximately 200 integrations would be expected for one simulation. Moreover, since there is no closed-form, analytic solution to Equation 3-5, the integral must be computed numerically until convergence (e.g. using a numerical integration procedure such as qromo). This requires passing values to the numerical integrating procedure via common blocks in memory, since numerical integrating procedures typically restrict their input only to a pointer to the function that will be integrated. Thus, calculating the FOV loss factor requires around 200 complicated numerical integrations until convergence using an inherently slow method of data passing, while also being required to use an iterative loop to calculate the FOV loss at each time step, instead of

being able to calculate it vectorially (or in parallel). Making a reasonable estimate of 0.33 seconds per one FOV loss factor calculation (including all memory management) implies that to calculate the entire FOV loss function alone would require 200*0.33 = 66 seconds. While this value is not significant in an absolute sense, its relative magnitude is representative of the amount of time it takes to calculate the FOV loss factor using the analytic formula.

Making design changes and not knowing the expected changes in system performance in near-real time is a severe limitation in a design process. As described above, calculating the FOV loss factor directly from the analytic formula requires too many computations, which in turn takes too long to complete (not even close to real time). Thus, using the method above to calculate the FOV loss factor is not conducive to efficient and effective ALB system design. Generating look-up tables is one possible solution to the problem, but this results in designers being stuck with FOV loss functions corresponding to the handful of input combinations that were simulated at a previous time. Alternatively, developing a model of (i.e. empirically characterizing) the FOV loss factor that requires fewer computations yet is still faithful to the analytic formula could prove very useful for ALB system design. Furthermore, using the latter approach could result in the ability for ALB systems to estimate seafloor reflectance values in real time, since the FOV loss factor would now be predicted in real time. With these benefits in mind, the next section of this chapter will discuss in detail the derivation and implementation of a FOV loss factor model in Interactive Data Language (IDL). Then, the Results section will briefly discuss the accuracy and boundaries of the model.

3.3 Deriving the Model

The FOV loss factor in analytic form is expressed in Equation 3-5 [17][26]. Since it is difficult to visualize what this function looks like, Figure 3.2 shows the FOV loss factor versus depth for a hypothetical ALB system. By inspection, the FOV loss function

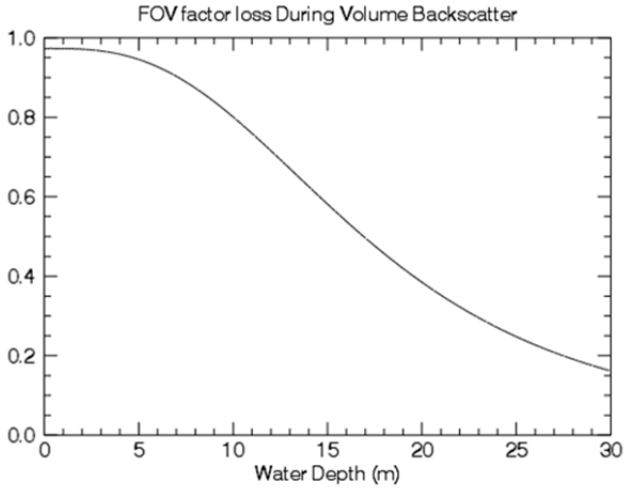

Figure 3.2: FOV Loss Factor for a Hypothetical 40-mrad System in Coastal Water with Diffuse Attenuation Coefficient, K_d, of 0.12 m^{-1}

does not depart much from unity at shallower depths; therefore, it does not contribute a significant loss term to the overall received power (Equation 3-2). However, the deeper the water depth, the more significant the FOV loss factor becomes. For example, while the 3-dB loss depth for this system is approximately 17 to 18 meters, the additional increase in depth beyond 18 meters to cause another 3-dB loss is only 7 meters. Thus, an ALB system in relatively clear waters should easily detect the seafloor in waters up to 20 meters, but every incremental increase in depth beyond that gets much more difficult for the system to detect the seafloor. Clearly, the straightforward attenuation factor (Equation 3-4) plays a major role in signal loss in deeper waters, as the signal decays exponentially with optical path length, but the FOV loss factor contributes significantly as well. Failure to account for this term will result in overestimation of the maximum detectable water depth for a given system and in inaccurate estimates of seafloor reflectance.

3.3.1 Choice and Justification of Independent Variables

In order to begin forming the model, the best place to start is determining which variables in Equation 3-5 are interesting for a designer to change, which have statistical interrelationships with others (if any), and which can be treated as constant across simulations (if any). The variables that appear in Equation 3-5 are time elapsed, the divergence of the transmitted pulse, the initial beam radius, the FOV of the airborne receiver, the radius of the receiver aperture, the flying height of the aircraft, the forward scattering coefficient of the surveyed water, and the water type optical index. Using the categories previously defined, the variables can be classified as seen in Table 3.1.

Table 3.1: Classification of Variables in the FOV Loss Function

Classification of Variables	
Desirable to Change	Time Elapsed, Receiver FOV, Forward Scattering Coefficient, Water Type Optical Index
Constant Across Simulations	Initial Beam Radius, Divergence of Transmitted Pulse, Radius of the Receiver Aperture, Flying Height of the Aircraft
Statistically Interrelated	Forward Scattering Coefficient, Water Type Optical Index

Time elapsed is clearly a variable of interest for the model because it is directly proportional to the pulse's optical path traveled in the water. The receiver FOV needs to be an independent variable of the model because that is what I am seeking to characterize: how the FOV loss factor changes as a function of FOV. Finally, the forward scattering coefficient and the water type optical index values are necessary input variables to the model because they are characteristics of the surveyed water. Since surveys are conducted in different locations with different water types, these variables need to be inputs so that the model can account for the differences in a surveyed water's

characteristics. Fortunately, as will be discussed shortly, these values are statistically related [17], which helps keep the model simple.

Moving on to the variables that were chosen to be constant across simulations, the primary justification for each of these variables to be treated as constant is that these can all be thought of as fixed parameters of a given system. The instruments used in the system determine the transmitted pulse characteristics (i.e. its initial radius and its divergence) and the receiver aperture radius; the desired swath width determines the flying height of the scan. Thus, these four variables do not need to be included as independent variables to the model.

Finally, the forward scattering coefficient and the water type optical index are classified as statistically interrelated variables. As mentioned above, these variables are indicative of the surveyed water's characteristics. There are well-known statistical relationships that can be used to relate these variables as a function of the beam attenuation coefficient, c, which are expressed in Equations 3-10 through 3-16.

$$\omega_0 = 0.944 - 0.048/c \tag{3-10}$$

$$b = c \cdot \omega_0 \tag{3-11}$$

$$V_l = 1.44 \cdot 10^{-2} + 1.68 \cdot b \tag{3-12}$$

$$V_s = \frac{(b - b_w) - V_l b_l}{b_s} \tag{3-13}$$

$$\beta(\theta) = \beta_s(\theta, 550) \cdot V_s \cdot \left(\frac{550}{\lambda}\right)^{1.7} + \beta_l(\theta, 550) \cdot V_l \cdot \left(\frac{550}{\lambda}\right)^{0.3} + \beta_w(\theta, 550) \cdot \left(\frac{550}{\lambda}\right)^{4.3} \tag{3-14}$$

$$b_f = \int_0^{\pi/2} \beta(\theta) \cdot \sin(\theta)\, d\theta \tag{3-15}$$

$$m = (0.142 - 0.132 \cdot \overline{\cos\theta})^{-1/2} \tag{3-16}$$

where,

$b_s = 1.34\ {}^{1}/_{m}$
$b_l = 0.312\ {}^{1}/_{m}$

$b_s = 1.7 \cdot 10^{-3}\ {}^{1}/_{m}$
$\overline{\cos\theta}$ is the average cosine of the scattering angle.

To explain the process of relating the forward scattering coefficient, b_f, and the water type optical index, m, as a function of the beam attenuation coefficient, c, first let us assume that the beam attenuation coefficient is the defining characteristic of a given water type. We can then use Equations 3-10, 3-11, 3-12, and 3-13 to generate estimates for the parameters of Kopilevech's volume scattering function (VSF) in equation (3-14) [17]. Then, using the tabulated VSF values found in [30], Equation 3-14 can be used to generate the estimate of the VSF. Finally, from the estimate of the VSF, b_f and m can be calculated using Equations 3-15 and 3-16, respectively. Thus, we can use the beam attenuation coefficient value as the only input variable to our model that is related to the surveyed water. This means that our model for the FOV loss factor will be reduced from four variables to three. Additionally, for sake of clarity, let us transform the time elapsed variable, $t–t_0$, into optical distance traveled in the water, l_w, via Equation 3-17.

$$l_w = v \cdot (t - t_0) \tag{3-17}$$

Therefore, we have now arrived at the three independent variables that serve as inputs to the model: optical path length traveled, receiver FOV, and the beam attenuation coefficient of the surveyed water. Figure 3.2 shows a transfer function representation of the FOV loss factor model.

3.3.2 Choice and Justification of Mathematical Model

The first attempt to model the FOV loss factor was to use a polynomial function of depth. This idea was borne out of a desire to keep the model as simple as possible. Unfortunately, higher order polynomials (greater than 4^{th} order) were required to fit the function to a reasonable degree of accuracy. Using such a model for this application

would pose two problems: (1) that we would be required to save too many coefficients per FOV-beam attenuation coefficient pair; and, (2) that this was just a classic example of over-fitting a model to the data, resulting in a non-generalizable model to a new, larger dataset. Thus, I did not make any further attempts to use a polynomial model.

The next idea for a model came from inspecting the overall shape of the FOV loss factor as a function of depth. As seen before in Figure 3.1, the FOV loss factor looks similar to the right half of a Gaussian as a function of depth. Initial Gaussian fits were promising for a fixed beam attenuation coefficient. However, upon varying the value of the beam attenuation coefficient, Gaussian fits no longer worked as well because the roll-off with depth became too steep as the beam attenuation coefficient increased. This caused overestimates (larger values) of the FOV loss factor at shallower depths and underestimates at larger depths.

Figure 3.3 illustrates the effect of increasing the beam attenuation coefficient on the FOV loss factor as a function of depth for a given receiver FOV. As one would

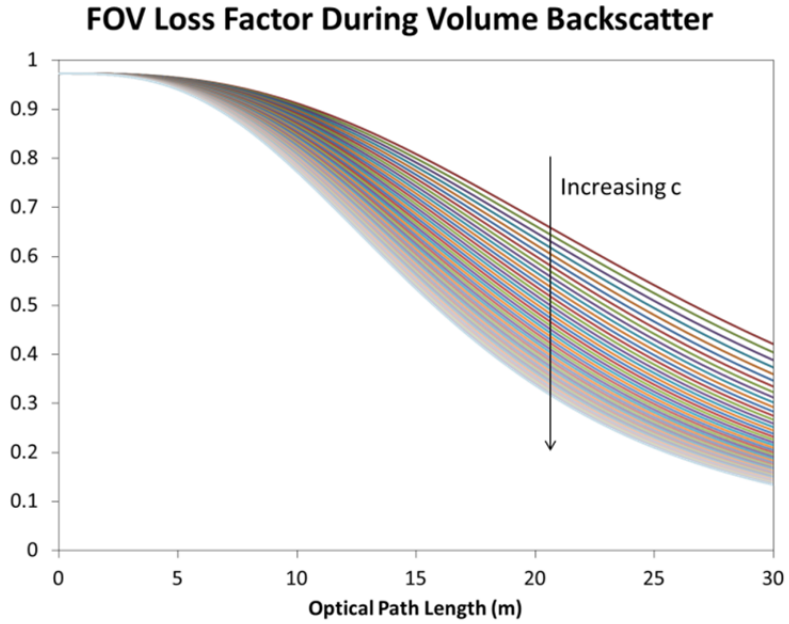

Figure 3.3: The Effect of Increasing the Beam Attenuation Coefficient on the FOV Loss Factor as a Function of Depth for a Constant Receiver FOV

expect, an increase in the beam attenuation coefficient results in a larger FOV loss factor, which is represented by the inward shift of the FOV loss factor curve as *c* is increased. This effect can be explained by the fact that an increase in the beam attenuation coefficient causes an increase in the scattering coefficient, which in turns results in more photons being scattered outside of the receiver FOV. It was for these curves corresponding to larger *c* values that the Gaussian model did not provide accurate estimates of the FOV loss factor.

Since a Gaussian fit nearly succeeded in providing an accurate model for the FOV loss factor, the next attempt was to use an exponential raised to a third-order polynomial. Using the fact that a Gaussian curve can be represented by an exponential raised to a quadratic polynomial, the cubic polynomial in the exponent would provide the model another control knob to fit the data better. As it turns out, this model worked fairly well, as is shown in Figure 3.4 for a specific case.

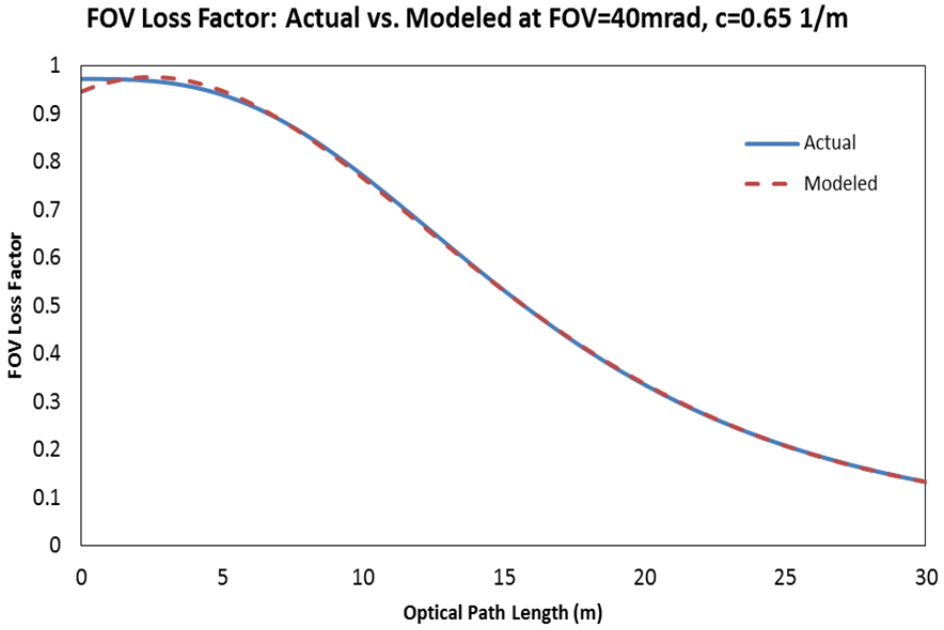

Figure 3.4: Actual vs. Modeled FOV Loss Factor with a FOV of 40-mrad and Beam Attenuation Coefficient of 0.65 m^{-1}.

Furthermore, even as the beam attenuation coefficient varied, this model maintained a reasonable level of accuracy. Thus, for a fixed pair of FOV and beam attenuation coefficient values, four coefficients can accurately model the FOV loss factor as a function of depth. This relation is expressed in Equation 3-18.

$$\widehat{F(l_w)} = \exp(\alpha l_w^3 + \beta l_w^2 + \gamma l_w + \delta) \tag{3-18}$$

where,

$\alpha, \beta, \gamma, \delta$ are functions of FOV & c.

A more important result, however, was that the four coefficients of the cubic polynomial displayed predictable trends as the beam attenuation coefficient varied. Specifically, α varied as a linear function of c, with r^2 equal to 0.9993; β varied as a linear function of c, with r^2 equal to 0.9952; γ varied as a cubic function of c, with r^2 equal to 1; and, δ varied as a cubic function of c, with r^2 equal to 0.9999. All r^2 values refer to regressions performed for a receiver FOV of 40mrad. Plots of these trendline fits to the data are provided in the Appendix. Below, these empirically derived relations are expressed in a general sense for a given FOV.

$$\alpha(c) = \alpha_\alpha c + \beta_\alpha \tag{3-19}$$

$$\beta(c) = \alpha_\beta c + \beta_\beta \tag{3-20}$$

$$\gamma(c) = \alpha_\gamma c^2 + \beta_\gamma c + \gamma_\gamma \tag{3-21}$$

$$\delta(c) = \alpha_\delta c^2 + \beta_\delta c + \gamma_\delta \tag{3-22}$$

where,

$\alpha_\alpha, \beta_\alpha, \alpha_\beta, \beta_\beta, \alpha_\gamma, \beta_\gamma, \gamma_\gamma, \alpha_\delta, \beta_\delta, \gamma_\delta$ are all specific to a given FOV.

$\alpha(c), \beta(c), \gamma(c), \delta(c)$ are estimates of $\alpha, \beta, \gamma, \delta$ in Equation 3-18.

α_β means: "the α coefficient of the regression estimating β."

Since the coefficients of Equation 3-18 behaved predictably in a rather simple manner, it was possible to fit trendlines to the coefficient values as a function of beam attenuation coefficient. Hence, estimating the cubic polynomial coefficients for a given FOV from the beam attenuation coefficient became possible. Therefore, the practical implication of this is that for a given receiver FOV, ten empirically derived coefficients can be manipulated to estimate the FOV loss factor as a function of water type (beam attenuation coefficient) and water depth. This means that instead of having to calculate F analytically, we can now use these ten coefficients to evaluate five equations (the four coefficient equations and the FOV equation) to produce an estimate for the FOV loss factor at a given FOV.

Finally, I looked into how the ten coefficients of Equations 3-19 through 3-22 varied as a function of FOV, hoping to model the variation of these coefficients in a simple way. Unfortunately, however, this was not the case, as many of the coefficients varied in ways consistent with high-order polynomials as a function of FOV. This result was not too much of a drawback, though, since we could simply implement a look-up table of coefficients $\alpha_\alpha, \beta_\alpha, \alpha_\beta, \beta_\beta, \alpha_\gamma, \beta_\gamma, \gamma_\gamma, \alpha_\delta, \beta_\delta, \gamma_\delta$ for each FOV of interest. Although this appears restrictive and seems like the situation we tried to avoid by creating this model, storing these coefficients actually is not too restrictive at all. In fact, it provides us with a two-dimensional space of FOV loss factor values for each FOV desired in the look-up table. This two-dimensional space spans the entire range of beam attenuation coefficient values swept across to generate the trendlines for $\alpha(c), \beta(c), \gamma(c), \delta(c)$ and the range of optical path length values used for $\widehat{F(l_w)}$. Moreover, this two-dimensional space is continuous over the range of simulated values, because the trendlines interpolate between non-simulated values of c, and l_w. Therefore, for N number of FOV rows in the look-up table, one actually has "N times all conceivable combinations of c and l_w in the modeled space" number of FOV loss estimates. Since each FOV row in the look-up table consists of only ten coefficients, 400

stored coefficients, or 40 discrete FOVs, ostensibly produces an uncountable number of unique FOV loss estimates in each space of FOV-(c_{min},c_{max})-($l_{w,min}$,$l_{w,max}$). By comparison, a common length for a single FOV loss function is 200 values. Therefore, storing 400 coefficients using the full FOV look-up table method, only produces two FOV loss factor functions with completely fixed water type characteristics and FOV values. Thus, the utility of my model becomes evident.

3.3.3 Application of the Model

In order to use this model, the first thing that must be done is determine the values for all of the variables of interest (Table 3.1). First, the values that remain constant across simulations, initial beam radius, beam divergence, receiver aperture, and flying height, must be selected. Since this model was developed using parameters similar to CZMIL's [12][14][15][16] in order to simulate the capabilities of a state-of-the-art system, the initial beam radius was selected to be 1.8m, the beam divergence was 0.01mrad, the radius of the receiver aperture was 0.2m, and the flying height was 400m. Then, the ranges of independent variables must be selected. For optical path length, I selected values corresponding to water depths from 0m to 30m; for beam attenuation coefficient, I selected values from 0.2 m^{-1} to 0.65 m^{-1}; and, for receiver FOV, I selected values from 20mrad to 55mrad (increments of 1mrad).

Next, a programming script must be written to calculate all of the necessary coefficients. As stated earlier, I used IDL for this purpose. The script should sweep across all FOV and beam attenuation coefficient values. For a given FOV, the FOV loss factor corresponding to each value of the beam attenuation coefficient must be saved in a vector corresponding to each optical path length value. Thus, for a given FOV, there will be an array of size length(c) x length (l_w), where length(.) signifies the number of elements in the vector. The next step is to take the natural log transform of the two-dimensional array of FOV loss function values. Next, a third-order polynomial fit is

performed for each FOV loss function corresponding to a unique beam attenuation coefficient value. Each of the four coefficients must be saved in a new vector (dim: 1 x 4), which results in an array of dimensions length(c) x 4 for each FOV. Each column of this new array corresponds to the α, β, γ, and δ values as a function of c for a given FOV. Therefore, a linear fit must be performed to the column corresponding to α to produce α_α and β_α; a linear fit must be performed to the column corresponding to β to produce α_β and β_β; a cubic fit must be performed to the column corresponding to γ to produce α_γ, β_γ, and γ_γ; and, a cubic fit must be performed to the column corresponding to δ to produce α_δ, β_δ, and γ_δ. These values represent the ten coefficients necessary to estimate the FOV loss function for a given FOV. Performing these steps across all FOV values, in this case 20mrad to 55mrad, produces all coefficient values that can then be stored in a look-up table. This look-up table can then be used to greatly increase the speed of software that simulates bathymetric waveforms, or to estimate the FOV loss factor when attempting to invert the radiative transfer function to estimate seafloor reflectance.

3.4 Results

The model for the FOV loss factor proposed in this chapter is an exponential raised to a third-order polynomial function of optical path length traveled in the water. Each of the polynomial's coefficients are functions of FOV and beam attenuation coefficient. In particular, for a given FOV, the third- and second-order coefficients are linear functions of beam attenuation coefficient, while the first- and zeroth-order coefficients are cubic functions of beam attenuation coefficient. The tested region of support, or boundaries, for the proposed model extended from FOVs of 20mrad to 55mrad, from beam attenuation coefficients of $0.2m^{-1}$ to $0.65m^{-1}$, and from water depths of 0m to 30m (optical path lengths of 0m to 30m/cos15°). There is nothing significant about the selected values of beam attenuation coefficient or optical path length. In fact, it is desirable to expand these ranges in the future. As for the FOV values, I chose the

selected range of values in order to remain in the realm of sufficient receiver FOV to capture the entire transmitted beam's cross section on the water surface. As briefly discussed, reducing the receiver FOV to smaller values would require a more detailed examination of its effects on k_{sys}, the decay term that appears in the attenuation factor.

While I did not perform an exhaustive measure of the model's accuracy, I did perform a very simplified error analysis by selecting various points in the 2D-space comprised of FOV and beam attenuation coefficient values and testing the accuracy of the model's estimate. To do this, I compared estimates of FOV loss functions for continuum points (central FOVs and central beam attenuation coefficients) and boundary points (boundary FOV values with boundary beam attenuation coefficients values) against their respective actual FOV loss functions. I then recorded the mean-squared-error (MSE) values for each of these comparisons. Table 3.2 contains the results of these comparisons. The Appendix contains plots of the modeled versus actual FOV loss functions for each of these cases.

Table 3.2: A Measure of the Proposed Model's Accuracy for Selected Continuum and Boundary Points in the Region of Support.

MSE Values for Various FOV-Beam Atten. Coeff. Pairs				
FOV	25 mrad		35 mrad	
c (m^{-1})	0.25	0.5	0.3	0.4
MSE	3.25E-04	9.76E-05	1.51E-05	1.73E-04
FOV	40 mrad		50 mrad	
c (m^{-1})	0.3	0.4	0.45	0.6
MSE	1.64E-05	1.53E-04	1.29E-04	4.40E-05

As can be seen in Table 3.2, the MSE values are all extremely small for the tested cases. When considering that the values of the FOV loss function are all on the order

between 0 and 1, these MSE values indicate an extremely accurate model. For example, consider a MSE value of $1x10^{-4}$, roughly the average of the calculated MSE values. This value would represent a 0.02% difference from an actual value of 0.5. Even for extremely deep waters with large scattering coefficients where the FOV loss factor approaches 0.01, an error of $1x10^{-4}$ would still only represent a 1% estimation error, which certainly falls in the range of acceptable error. I will perform more testing of the model's accuracy in the future, as I continue with my research. Specifically, a more comprehensive measure of the accuracy of the model across all combinations of FOV, beam attenuation coefficient, and optical path lengths will be performed in order to analyze and quantify the model's expected error at all of the boundaries. Using an in-house capability, such as using TMT, could provide an extremely useful platform for doing so. This will be important when moving forward into the realm of estimating the FOV loss factor in order to estimate seafloor reflectance in real time. For now, however, these results signify that the model is accurate enough for the purposes of simulating bathymetric return waveforms and quickly understanding the effects of varying the receiver's FOV.

3.5 Conclusion

The FOV loss function plays an important role in the ability of ALB systems to detect the seafloor, as it introduces a significant loss term in the bathymetric lidar equation for deeper and less clear waters. This function cannot be calculated using the analytical formula in real time, as the total computation time necessary to calculate it at all sampling times during pulse traversal of the water column is on the order of many 10's of seconds. This is unacceptable for engineers attempting to design an ALB system efficiently and effectively. Consequently, state-of-the-art ALB design groups have probably relied on look-up tables of FOV loss functions, as no methods of real time calculation have been published in ALB literature. Instead of using that approach, which

restricts designers to pre-generated FOV loss functions with fixed input parameters, this chapter proposed modeling the FOV loss function as a function of receiver FOV, beam attenuation coefficient in the water, and optical path length traveled in the water, keeping the remaining variables that appear in the analytical equation constant. Using this model produces accurate calculations of the FOV loss function in real time for water depths up to 30 meters, receiver FOVs from 20mrad to 55mrad, and for coastal waters of beam attenuation coefficient of $0.2m^{-1}$ to $0.65m^{-1}$ (roughly corresponding to K_d values of $0.05m^{-1}$ to $0.16m^{-1}$).

Thus far, I have only used this model to study the effects of varying the receiver FOV on a simulated bathymetric return waveform. As expected, there is not much of a difference between smaller FOVs and larger FOVs for a given water type at shallower depths. However, as the water depth increases, smaller FOVs produce weaker return signals than systems employing larger receiver FOVs. Similarly, for a constant receiver FOV, there is not much of a difference in return signal at shallower between waters of differing forward scattering coefficient. However, as water depth increases, waters with larger forward scattering coefficient produce weaker return signals.

The method used to model the FOV loss factor is not restricted to the stated ranges of water depth and beam attenuation coefficient. Using the approach outlined in section 3.3.3 with a larger range of values for these variables will produce a model of the FOV loss factor over a wider range of water types and water depths. As for future adjustment of the range of FOV values, users should take great care when decreasing the receiver FOV to a value that results in a subtended size on the water surface smaller than the cross-section of the transmitted beam on the water surface. The FOV loss function will no longer start from a value of near unity at the water surface [26], nor will the K_{sys} value be close to K_d, rendering the application of this model invalid. However, assuming users intend to stay within the boundaries of the model, this method of estimating the FOV loss function could prove very useful for groups attempting to invert the radiative

transfer equation and solve for reflectance in real time. By estimating the optical properties of the surveyed water, perhaps utilizing published climatological data of the water's beam attenuation coefficient or extracting estimates from measured waveforms during a mission, a real time estimate of the FOV loss factor can be generated using this model, which can then be used to generate an estimate of seafloor reflectance. Without a real time estimate of the FOV loss factor, accurate estimates of seafloor reflectance cannot be obtained. Thus, aside from improving the ALB system design process, the utility of this model may ultimately lie in the application of real time seafloor reflectance estimation.

CHAPTER 4

THE TARGET DETECTION CAPABILITIES OF AN AIRBORNE LIDAR BATHYMETRY SYSTEM

Over the past few decades, the popularity of using ALB systems in the remote sensing of coastal zones has increased due to their efficiency in mapping and surveying large areas. The primary objectives of these surveys are to monitor the health of marine ecosystems over time, to provide accurate bathymetric measurements of oft-traveled coastal waters, and to perform rapid reconnaissance of navigation channels [1]. For reconnaissance applications, ALB systems must be able to detect large obstructions in coastal waterways, as they could endanger commercial vessels traveling in these waters. In fact, as part of IHO (International Hydrographic Organization) requirements, all IHO-1 surveys must detect any features larger than 2-meter cubes in depths up to 40 meters [31]. Moreover, IHO Special Order surveys require features as small as 1-meter cubes to be detected [31]. Multiple groups have performed theoretical and experimental tests to examine the effectiveness of ALB systems in satisfying these requirements [1][32][34]. From these tests, it appears that ALB systems perform very well in detecting 1-meter and 2-meter features in a variety of waters and over a large range of depths. There even appears to be evidence of features as small as 0.5-meter cubes being detected. The objective of this chapter is to assess these claims and predict the target detection performance of today's state-of-the-art ALB systems with the constraint that I do not currently have the capability to obtain experimental data. Therefore, I performed a theoretical exploration of the target detection capabilities of ALB systems using my newly designed bathymetric waveform simulator, the YellowJacketSimulator.

4.1 Background

Underwater targets in ALB systems generally fall into three categories: those that are smaller than the beam diameter, those that are comparable to the beam diameter, and those that are significantly larger than the beam diameter. However, when determining the probability of detecting a target, it is difficult to classify one using the size of the target because its location in the water column and the surveyed water's turbidity both determine what proportion of the beam diameter the target fills. As discussed in Chapter 2, this is due to the propagating pulse expanding into a growing cone of light as it travels deeper into the water. This expansion of the beam, or the beam spread function, depends on many parameters, one of which is the water's volume scattering function. For more turbid waters, the volume scattering function exhibits larger off-axis scattering, meaning the pulse will spread much faster. Therefore, a target that is comparable to the beam size in optically shallower water will be smaller than the same beam's size at larger depths. Similarly, a target that is significantly larger than the beam diameter in optically shallower water may be comparable to the beam diameter at some deeper location in the water column. Thus, various groups developed a more refined categorization of targets, one that describes targets consistently across water types and optical depths.

4.1.1 Prior Studies

In 1996, Guenther et. al performed an analytical study of the target detection capabilities of the SHOALS system [32]. In this work, they introduced the concepts of "type-1" and "type-2" detections to describe target classification. Type-1 targets are those that introduce two distinct local maxima in the bathymetric return waveform after the surface response. Type-2 targets are those that produce a single, distorted bottom return in the bathymetric return waveform after the surface response. Figure 4.1 shows example return waveforms for both type-1 and type-2 targets. The significance of using this nomenclature is that it decomposes the overall probability of detecting a given target

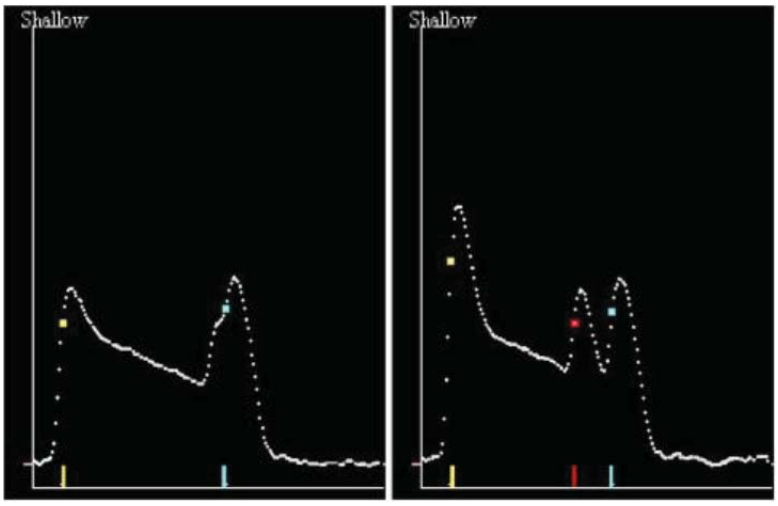

Figure 4.1: Typical Bathymetric Return Waveforms with Target-Induced Distortions [1] – Left: Type-2 Target Return; Right: Type-1 Target Return

into the probability of successful type-1 and type-2 detections, rendering the need to classify the target as large or small relative to the beam diameter unimportant. To calculate a target's detection probability we can simply sum the number of successful type-1 and type-2 detections for a given target and then divide by the total number of trials. We can do this without worrying about the target's size relative to the beam diameter, since the meaning of type-1 or type-2 effectively handles the relative size of the target with respect to the beam.

Consider a 1-meter cube's effect on the return waveform as a function of its location in the water column. Almost anywhere in the water column, the 1-meter cube will produce type-1 waveforms, except for when it nears the seafloor in optically deeper waters, in which case it will probably produce a type-2 detection. In this case, then, the ability to detect the 1-meter cube depends on the probability of both type-1 and type-2 detections. Now, consider the same target in shallower water. The 1-meter cube may only produce type 1-detections wherever it is located in the water, even on the seafloor, because it takes up more of the laser footprint since the beam has not spread as much. In this case, the ability to detect the 1-meter cube depends on the probability of type-1

detections only. The commonality between these scenarios is that we simply need to add the probability of type-1 and type-2 detections to determine the overall probability of detecting the target. Therefore, by determining an ALB system's ability to discern type-1 and type-2 targets in different water environments, we can estimate the probability of detecting a target in any environment.

Guenther et. al followed this type of procedure when determining the target detection capabilities of the SHOALS system [32]. They derived target detection probabilities, the sum of the system's successful type-1 and type-2 detections, based on a geometric model of the system and performing a Monte Carlo simulation. From the Monte Carlo analysis, they determined the following items affect an ALB system's ability to detect a target: (1) the probability of a pulse hitting the target as a result of the scanning pattern; (2) the probability that the target return is resolvable (i.e. a successful type-1 or type-2 detection); and, (3) the detection algorithm's ability to measure the location of the target in the waveform. System-based parameters affect the first and third items. The probability of a pulse hitting the target depends on the type of scanning pattern employed, the scanning rate, and the pulse rate. The detection algorithm's ability to measure the location of the target is dependent upon the sophistication of the algorithms available, both the real time algorithms that supply the important metadata about the waveform and the post-processing algorithms that can automatically identify the anomalies in the waveform. On the other hand, a combination of system and environmental-based parameters affect the second item. Every term that that appears in the bathymetric lidar equation as well as the target's size, reflectance, and location determine the strength of the target signature in the waveform.

The detection probability results obtained by Guenther et. al for 1-m^2 and 4-m^2 circular cylinders (of various heights) are displayed in Figure 4.2. These results span various water conditions and water depths, but the targets were always located

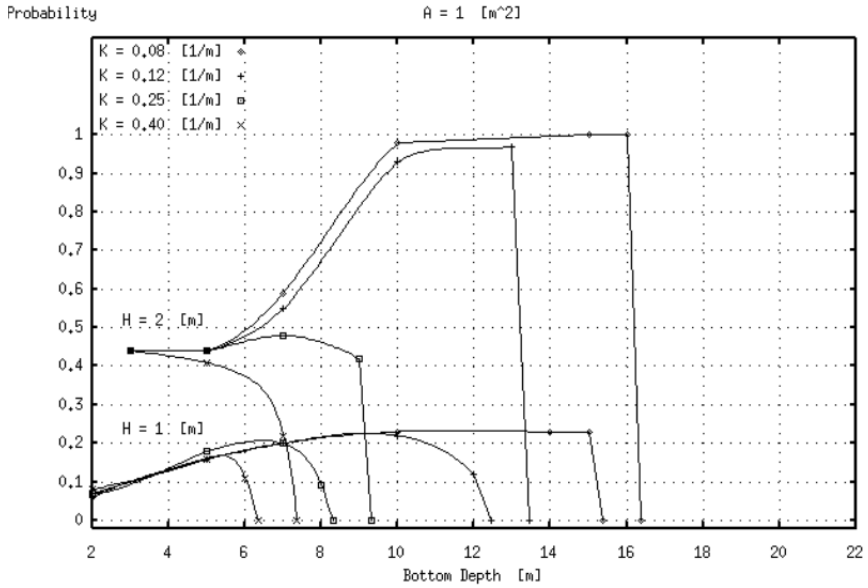

Figure 4.2 (a): Target Detection Probabilities for 1-m^2 Circular Cylinders of 1-m and 2-m Heights in Various Water Clarities [32]

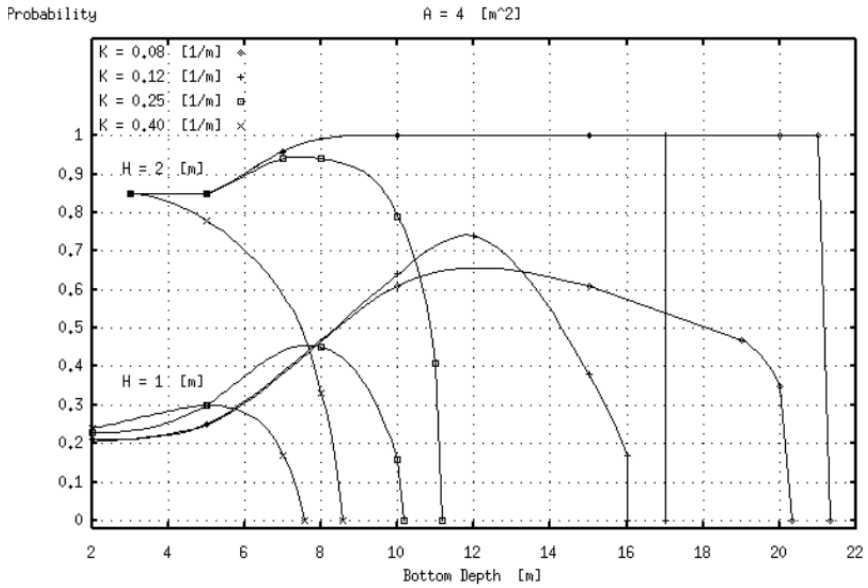

Figure 4.2 (b): Target Detection Probabilities for 4-m^2 Circular Cylinders of 1-m and 2-m Heights in Various Water Clarities [32]

between 0.5 meters to 2 meters above the seafloor. From the plots, it is clear that target detection probabilities are higher for larger target heights (H=2m curves are higher than

H=1m curves in both figures), for larger target areas (the curves in 4.2(b) are higher than their corresponding curves in 4.2(a)), and for less turbid waters (all curves shift outward and upward as the diffuse attenuation value, K, decreases). Detection probabilities increase as the depth increases at lower depths due to the beam-spreading phenomenon. Because the beam spreads into the expanding cone of light, the beam illuminates more of the water column as the pulse travels deeper into the water, meaning there is a greater chance of hitting a target. Since the geometric surface coverage dominates the overall probability of detecting the target at the shallowest depths, it would be expected that performance in this region could be improved by increasing the lidar point density on the surface. Additionally, since very shallow waters present difficulties for algorithms to detect the bottom accurately, target detection suffers in this region as well. Therefore, detection probabilities at shallower depths could also be increased by improving algorithmic performance.

In [1], Yang and LaRocque revisited the target detection capabilities of the SHOALS system after a decade of improvement in both system and algorithmic capabilities. They used the same detection characterizations of type-1 and type-2 target detections, yet they also introduced the idea of Case-1, Case-2, and Case-3 targets. Case-1 targets are those that are identifiable in the lidar's point cloud data as a region of shallower depth due to the target being significantly larger than the beam diameter. Case-2 targets are those that that produce type-1 detections due to the target being of comparable size to the beam diameter. Case-3 targets are all of the remaining targets that produce type-2 detections. In performing the updated SHOALS study, they corroborated much of what Guenther et. al had suggested a decade earlier by stating that the probability of detecting a target depends on the probability that the target will be illuminated by the laser beam and the ability to identify target return signals in the return waveform. They then identified seven key parameters that affect the above considerations: (1) the target's dimensions; (2) water depth; (3) water clarity; (4) system

configuration; (5) survey planning; (6) data processing abilities; and, (7) algorithmic sophistication in automatically identifying bottom anomalies.

Buoyed by advancements in SHOALS configuration and by improvements in data processing algorithms, Yang and LaRocque provided an improved set of detection probabilities for the SHOALS system, as seen in Tables 4.1 and 4.2. From these tables, it

Table 4.1: Target Detection Probabilities for 2-m Cubes by SHOALS System [1]

Target ID	Bottom Depth	2 × 2 Spot Spacing	3 × 3 Spot Spacing	4 × 4 Spot Spacing
1S	5.6 m	100% (7/7) [A]	N/A (0/15) [B]	N/A (0/17) [B]
2S	10.1 m	100% (9/9) [A]	100% (10/10) [C]	100% (9/9) [C]
3S	19.3 m	100% (17/17)	100% (6/6) [D]	100% (8/8)
4S	22.7 m	100% (18/18)	100% (6/6) [D]	91% (10/11)
5S	25.6 m	100% (10/10)	100% (6/6) [D]	100% (13/13)
6S	28.3 m	100% (11/11)	100% (6/6) [D]	73% (8/11)
1N	5.5 m	N/A (0/4) [E]	100% (7/7) [F]	100% (8/8) [F]
2N	12.4 m	100% (3/3)	100% (6/6) [F]	100% (8/8) [F]
3N	19.5 m	100% (5/5)	100% (16/16)	100% (17/17)
4N	20.5 m	100% (3/3)	100% (11/11)	93% (13/14)

Table 4.2: Target Detection Probabilities for 1-m Cubes by SHOALS System [1]

Target ID	Bottom Depth	2 × 2 Spot Spacing	3 × 3 Spot Spacing	4 × 4 Spot Spacing
1S(1m)	5.9 m	100% (11/11)	63% (5/8)	67% (2/3)
2S(1m)	10.2 m	100% (10/10)	70% (7/10)	63% (10/16)
3S(1m)	19.5 m	81% (13/16)	0% (0/6) [G]	0% (0/11) [H]
4S(1m)	22.8 m	100% (18/18)	100% (6/6)	45% (5/11)
5S(1m)	25.4 m	67% (6/9)	33% (2/6)	17% (1/6)
6S (1m)	27.6 m	43% (3/7)	40% (2/5)	38% (3/8)

appears that for sufficient coverage (i.e. higher lidar point densities) on the sea surface, SHOALS detected 2-m cubes 100% of the time to depths of 20 meters and 1-m cubes nearly 100% of the time to depths of 20 meters. Thus, in clear waters the newer SHOALS system exceeded the IHO-1 survey requirements, whereas the hypothetical

version of SHOALS presented in Guenther et. al did not. The biggest reason for the improvement in detection probabilities resulted from hardware advancements that produced higher laser pulse repetition rates, higher point densities, and complete bottom illumination and software advancements that detect subtle target signatures more reliably. Therefore, as expected, target detection results improved by increasing surface coverage and improving data processing capabilities. Optech has since released a new ALB system, CZMIL, that is an upgrade over the SHOALS system [12][34]. Since CZMIL has improved scanning capabilities, better hardware, and improved data processing and algorithmic capabilities, it is reasonable to assume that the target detection capabilities of that system meet and exceed the published capabilities of the SHOALS system [1].

4.1.2 Probability of Illuminating a Target

The most important system parameters that affect the probability of a laser beam illuminating an underwater target are the initial beam radius, the scanning mechanism, the scanning frequency, and the pulse repetition rate. A larger beam radius increases the probability of a single pulse hitting a target because it increases the portion of the water column illuminated by the propagating pulse, resulting in a higher probability of interacting with a target. The remaining parameters all affect the number of pulses that will actually hit the target. Faster scanning rates, higher pulse repetition rates, and circular scanning mechanisms provide higher surface point densities, thereby increasing the probability of producing waveforms that illuminate a target. The most important environmental parameters that affect the probability of a laser beam illuminating an underwater target are the optical properties of the surveyed water. For waters with higher absorption coefficients and backward scattering coefficients, the pulse may not travel deep enough into the water to illuminate the target. On the other end of the spectrum, however, extremely clear waters will not produce the type of beam-expansion in the

water column necessary to ensure 100% illumination of the seafloor for a given point density.

For scenarios in which multiple laser pulses illuminate a specific target, each of these returned waveforms exhibit slightly different target responses due to the change in relative location of the target [32]. Targets located outside of the principal ray path with respect to the nadir point interact with photons that travel longer optical path lengths to reach it and reflect back toward the receiver. Conversely, targets located within the principal ray path with respect to the nadir point interact with photons that travel shorter optical path lengths to reach it and reflect back toward the receiver. Thus, based on the relative location of the target to the principal ray within a given pulse's illuminated footprint, the target will appear deeper or shallower than it really is when the target is beyond or within the principal ray, respectively. These situations also introduce bias into the seafloor depth measurement as well. Consider the case of a target located nearer the nadir point than the unperturbed ray. Since light rays of shorter optical path length than the principal ray interact with the target and reflect back toward the receiver, these rays no longer contribute to illumination of the seafloor. By losing the contribution of these rays at the seafloor, only rays of longer optical path length form the seafloor response in the detected waveform. Therefore, the peak in the detected waveform corresponding to the seafloor return will be biased deep, which is a hazardous error bathymetric surveys must avoid. Analogously, targets that are outside the principal ray with respect to the nadir point bias the seafloor return shallow, since the longer optical path lengths no longer contribute to the seafloor response. This type of error is safer for commercial navigation purposes, but is still an error nonetheless. Assuming multiple pulses do illuminate the target, however, waveform averaging can be used as an effective tool to remove biases contained in individual waveforms.

Since circular scanning mechanisms have non-uniform point densities across the swath [15], the scanning mechanism employed by state-of-the-art ALB systems also

affects the probability of illuminating a target. As shown in Figure 4.3, the point densities on the edges of the swath are much higher than the point densities in the central

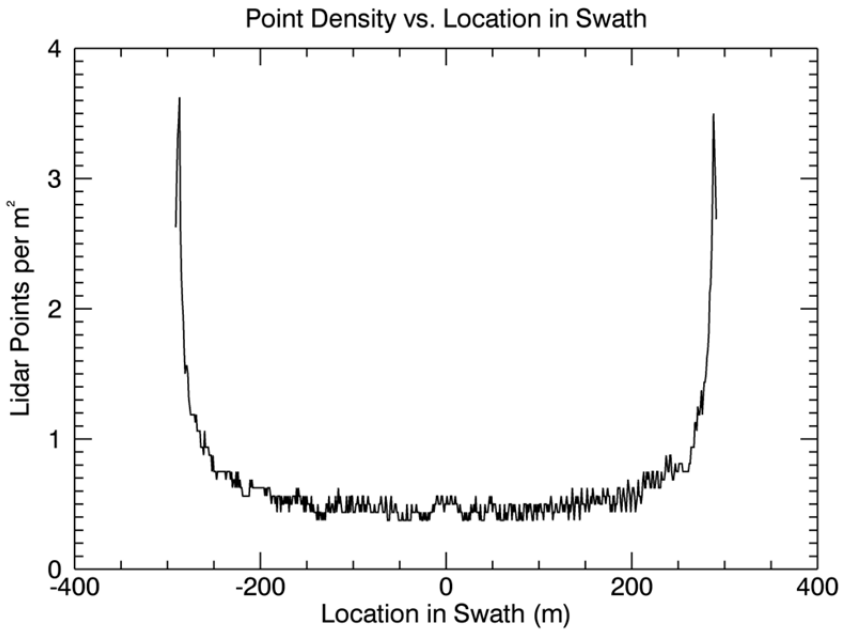

Figure 4.3: Point Density vs. Location in Swath for a Hypothetical ALB system flying at 400 meters, employing a circular scanning mechanism with scan rate of 27 Hz, pulse repetition rate 10 kHz, and 20˚ off-nadir angle.

portion of the scan. This plot was generated using the scanning simulator tool I developed in IDL, which will be discussed in section 4.2.1. Targets that happen to be located in the central portions of the swath will have fewer pulses that actually illuminate it because the point density is smaller. Conversely, targets that happen to be located on the edges of the swath will have more pulses that illuminate it because the point density is larger (approximately 4-6 times larger than the central portion of the swath based on typical parameters).

Finally, the overlap between successive scans, another related survey parameter, also plays a role in the ability to detect a target. Targets located in an overlapped region clearly have more chances of being hit by a laser pulse, as pulses from both the first and

second scans over the region can hit it. This would seem to increase the number of pulses that hit a target by a factor of two. However, overlapped regions do tend to be small, since too much overlap causes excessive flight times and operational costs. This means that the overlapped regions will be confined to the outskirts of the swath, which is where the point density is already the highest. Thus, targets within overlapped regions could be illuminated by two times the edge point density under sufficiently small overlap. Otherwise, the density of pulses that illuminate the target's area will be some combination of an edge point density with a central point density. In any case, targets located in the overlapped should have higher detection rates due to the higher probability of illuminating the target, which means a greater number of pulses can be used in waveform averaging techniques to boost the SNR. To illustrate this, Figure 4.4 shows the point density for the same system parameters as Figure 4.3 but with an overlapped distance of 100 meters between successive scans.

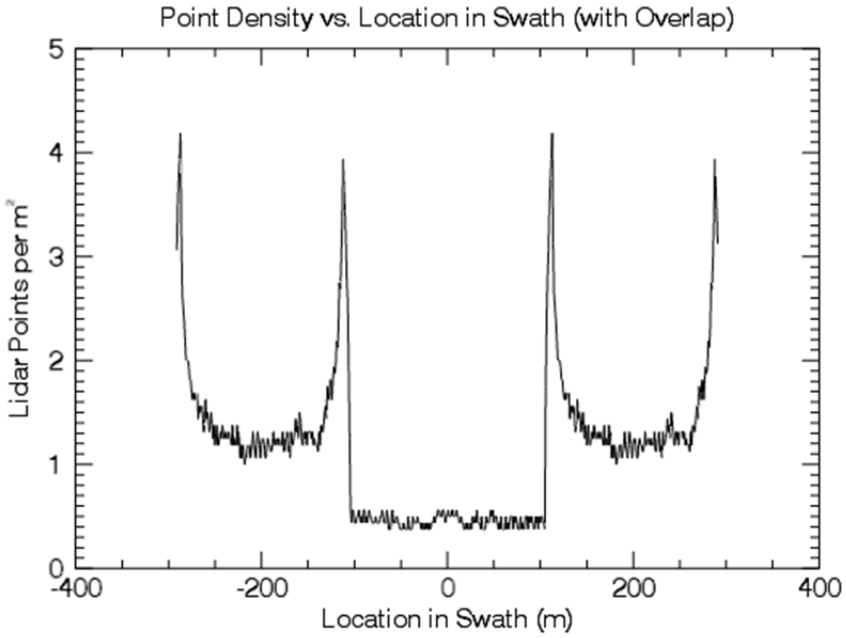

Figure 4.4: Point Density vs. Location in Swath for the same hypothetical ALB system as Figure 4.3 except with an overlap distance of 100 meters between successive scans.

4.2 Target Detection Procedure

Since our group has yet to build a laboratory bathymetric lidar, I used the YellowJacketSimulator to provide sample data of waveforms that interact with targets. In order to generate a representative data set of pulses that would interact with the target based on its location and depth in the water, I designed a circular scanning simulator that simulates the number of pulses that hit the target based on system and environmental parameters. Since there is a large number of environmental, system, and target parameters that affect the detectability of a target, I needed a way to vary all of these inputs to understand the effect of each of them on the probability of detecting a target. Instead of writing my own scripts to vary these parameters, I used EOSL's Test-Matrix-Tool (TMT), a software-testing platform that forms the cross product of all variable parameters and inputs them to the software, to produce tens of thousands of simulations with variable input parameters. Then, using TMT's Analysis GUI, I analyzed the effect of each of the inputs on the target's detectability.

TMT is a simulation-agnostic framework that provides end-to-end support for robust analysis of complex systems [35]. Essentially, TMT simplifies the specification, execution, and analysis of large-scale simulation workloads by forming all of the desired input combinations to be simulated, by executing and monitoring each simulation, by managing the results of each simulation, and by creating customized analysis interfaces that provide filtering capabilities to visualize and compare simulation data. It does these things by abstracting the simulation model into its inputs, outputs, and executable, which are specified in various XML files that are interpreted by TMT's internal scripts. To integrate the YellowJacketSimulator into the TMT framework, I simply specified the inputs and outputs of my system and provided a command-line accessible executable that TMT could call to run each simulation.

4.2.1 Overview

As discussed in Chapter 2, the YellowJacketSimulator models a bathymetric return waveform due to a single pulse. These waveforms are the convolution of the laser pulse with the noisy impulse response function and the stretching functions added to the background solar noise. In order to simulate a return waveform with a target signature in the waveform, I had to make a few adjustments to my radiometric model that generates the impulse response function. Namely, I had to change the volume-backscattering portion of the impulse response function. Instead of the backscattering coefficient simply being a noisy value about a mean backscattering coefficient for the entirety of water column traversal, the backscattering coefficient now had to incorporate information from the target when the pulse interacts with it. Specifically, the backscattering coefficient at a target's location in the water column is now calculated by multiplying the target's reflectance with the cross-section of the beam that the target area fills. Furthermore, the reflected portion of light bouncing off the target is now subtracted out from the remaining light that continues to propagate toward the seafloor. I made the following simplifying assumptions when implementing these changes: (1) this procedure continues to occur for as long the pulse interacts with the target; (2) that no light stretches into the region on the optical path beneath the target (i.e. the energy is completely removed from the propagating pulse); and, (3) that the target location in the water column is oriented in a plane normal to and co-located with the principal ray. Finally, recall my simulator assumes a uniform energy distribution throughout the cross-section of the beam in the water, so the target's cross section in the beam at a given depth is sufficient to describe the proportion of energy backscattered toward the receiver at that depth.

In order to understand the effects of multiple pulses hitting a target, I developed a circular scanning simulator to determine the number of pulses that we can expect would hit the target based on the target's location in the swath and depth in the water. As mentioned earlier, the pulse density for a circular scanner varies as a function of position

in the swath. The pulse repetition rate, the circular scan rate, the off-nadir angle, and the overlap between successive scans are all system parameters that affect the variability in point density across the swath. Additionally, the size of the beam at the target's depth also plays a role in how many pulses will illuminate a target. By using the first-order approximation that the beam diameter stays constant until it reaches a depth of twice its diameter, after which it increases as half of the optical distance traveled [3], we can assume a target's depth is the determining factor in the beam's size at the target depth. This has been shown to be an overestimate in clearer and optically shallower waters, but to first-order this a reasonable approximation of the beam spread function [1]. Thus, the system parameters mentioned above as well as the target depth are the inputs to the circular scanning simulator. Using these inputs, the simulator determines how many pulses would hit the target based on whether or not the center position of the beam on the water surface falls within a specified area that would produce a beam that hits the target.

After determining the number of pulses that would hit a given target, this number serves as the maximum number of waveforms that can be averaged together with a target response in them when calculating an averaged waveform. When a user selects a value smaller than this maximum, the averaged waveform simply does not use all of the information it could be using to produce a waveform with the best SNR. When a user selects a value greater than this maximum, the waveform simulator will produce extra waveforms with no target response in them to reach the desired value. These "target-less" waveforms will then contribute in producing the averaged waveform, lowering the SNR of the averaged waveform. The inspiration for creating averaged waveforms in this way was to mimic the post-processing techniques that will be used when we voxelize the water column. Voxelizations that use too big of voxel sizes average out too much of the local peculiarities, resulting in missed targets, while voxelizations that use too small of voxel sizes contain too much noise to be able to identify targets reliably in the averaged waveform. The circular scanning simulation tool used in conjunction with producing

averaged waveforms serves two important purposes: (1) it provides a reasonable method to aggregate each waveform's contribution to the surveying results by creating an averaged profile of the water column from all of the laser pulses that hit the target during a scan; and, (2) it allows me to quantify the effects of varying operational system parameters such as the scan angle, the scan rate, and the laser's pulse repetition rate on the target detection capabilities of an ALB system.

4.2.2 Integration with TMT

Since my theoretical exportation of ALB system performance in detecting underwater targets requires the specification, execution, and analysis of a large number of simulation test cases, which correspond to the cross product of all system, environmental, and target parameter combinations that affect a target's signature in the bathymetric return waveform, I needed to use a better approach to simulating each of these test cases than creating an *ad hoc* simulation framework. That is, instead of creating a series of nested loops over each of the parameters' range spaces to simulate the cross product of each input, saving the results from each simulation, and then creating parsing tools to parse and analyze the results, I would rather use a modular framework that allows me to simulate across variable range spaces without having to change my scripting, parsing, and visualization code every time. Therefore, I decided to embed my bathymetric waveform simulation environment inside of EOSL's TMT [35].

To embed my simulator in TMT, I used IDL's Linux-based command-line interface to execute my IDL programs. This involved writing code to wrap around the radiometric models to produce waveforms and to output the waveform data to a CSV file. This code was very similar to the code I used when developing the YellowJacket Simulator. In this case, instead of the input data coming from the GUI, the inputs come from text files that TMT produces based on the XML input specification. Additionally, instead of routing the waveform output to a plotting display in a GUI, the output for the

Linux-based code is written into a CSV file so that the target detection algorithm can read in the waveform data through another module of TMT. After completing all of the simulations, TMT can then display the successes and failures of the target detection code for every input combination simulated. Finally, because TMT runs on EOSL's cluster, I could produce results from tens of thousands of unique simulations in parallel and in a very short amount of time.

4.2.3 Detection Algorithm

The industry-standard method of extracting the surveyed water's depth can also be used to detect targets in the water column and on the seafloor [1][32]. This algorithm first involves smoothing the bathymetric return waveforms, via Savitzky-Golay filtering. Savitzky-Golay filters perform localized polynomial fitting to data such that system noise is suppressed, yet peaks and valleys in the data remain intact. The latter point is rather significant, considering the next step in the algorithm requires locating interest points on the smoothed waveform around the peaks corresponding to the surface and bottom returns. The peaks themselves are not used in the estimate of the water depth, because peak locations are too susceptible to noise. Instead, inflection points preceding these peaks, corresponding to the zero-crossings in the waveform's second derivative, serve as the estimates for the sea surface and seafloor locations. From these inflections points, one can then derive an estimate of the optical depth, and then use the geometric correction for off-nadir angle to compute the true water depth.

This same procedure can be used to estimate locations of targets in the water column, then, since Case-2 targets produce multiple peaks after the surface return. Instead of only saving the interest points corresponding to the sea surface and the seafloor, the depth-estimation algorithm now needs to provide the interest point corresponding to a target-induced peak as well, if one exists. Case-3 targets, on the other hand, do not produce multiple peaks after the surface response, but the depth-extraction

algorithm should still provide information about a target's presence, as it should predict a shallower depth as a result of the target-induced, distorted seafloor return. A colleague of mine, Jason Zutty, was the main programmer for the depth-extraction algorithms, including all of the Savitzky-Golay filtering and interest point detection code, which I then integrated into my existing YellowJacketSimulator software suite.

4.3 Results

After integrating the bathymetric lidar waveform simulator and the target detection algorithm into TMT, I produced the target detection results contained in this section by the following procedure:

(1) Instantiate a TMT matrix with a list of all variable parameters.

(2) For a given run, specify each parameter's range of values.

(3) Submit the instance matrix to TMT for simulation.

(4) After all of the simulations finish, run the TMT Analysis GUI to assess and visualize the results.

For case-1 targets, targets that produce elevated seafloors in the Digital Elevation Model, I considered estimates of the seafloor within 10% error of the target's true depth as successful target detections. For case-2 targets, targets that produce type-1 detection returns, I considered estimates of target depth within 10% error of the target's true depth target as successful target detections. For case-3 targets, targets that produce type-2 detection returns, I considered estimates of the seafloor within 10% error of the target's true depth as successful target detections. Finally, "probability of detection", or "detection rate", is defined as the number of successful detections of a target divided by the total number of trials; the term "false alarm rate" is defined as the number of targets identified in false locations divided by the total number of trials; and, the term "discrimination rate" is defined as the total number of successful detections divided by the total number of identified targets.

For simplicity, I made all targets cylinders with circular surfaces suspended in the water column such that they were in a plane normal to and co-located with the transmitted beam's reference ray. Moreover, all targets were located in the non-overlapped, central portions of the swath. All experiments used the following constant system parameters: 20˚ off-nadir angle, 0.1256-m^2 receiver area, optical efficiency of 0.06, average pulse energy of 3mJ, and a pulse FWHM of 2ns. As for the detection algorithm, all experiments used the parameters contained in Table 4.3. Search window, smoothing order, and smoothing window all refer to the input parameters to the Savitzky-Golay filter, while delta refers to the vicinity of samples around a detected peak in which the algorithm will seek to replace it with a stronger peak.

Table 4.3: Parameters Used in Target Detection Algorithm

Algorithmic Parameters	
Delta	500
Search Window	7
Smoothing Order	3
Smoothing Window	7

4.3.1 Dependence on Number of Waveforms that Hit the Target

The first experiment I conducted was to vary the number of waveforms that hit a given target at various depths in 20-meter coastal water. The objective was to observe the effects of changing the number of waveforms used in the waveform averaging process on successful target detection probability. The target had a 1-meter surface diameter, a height of 1 meter, and a reflectance of 0.2. The various environmental and system parameters are summarized in Table 4.4(a) and Table 4.4(b), respectively. Additionally, I varied the degree of inhomogeneity (0.0001 to 0.001m^{-1}-sr^{-1}, stepping by 0.0001m^{-1}-sr^{-1}) in the water column to increase the number of trials performed at a given depth to make the experiment more robust.

Table 4.4 (a): Environmental Parameters used to Determine the Effect of Number of Waveforms Hitting a Target on the Detection Probability.

Environmental Parameters	
a (m^{-1})	0.069
b_b (m^{-1})	0.007
b_f (m^{-1})	0.229
$\beta(\pi)(m^{-1}sr^{-1})$	0.005
depth (m)	20

Table 4.4 (b): ALB System Parameters used to Determine the Effect of Number of Waveforms Hitting a Target on the Detection Probability.

System Parameters	
Altitude (m)	400
FOV (mrad)	40
Scan Rate (Hz)	27
PRR (kHz)	10
Sampling Rate (Gs/s)	2

Figure 4.5 shows the probability of detecting a target located at any position between 3 and 17 meters, spaced at 1-meter intervals, versus the number of waveforms used in the averaging process. As can be seen in the plot, there is a linear trend (coefficient of determination equal to 0.833) between the number of waveforms used in the averaging process and the successful detection of the target. For every additional waveform used in the averaging process, there is a 1.7% increased probability of detecting the target successfully. Of course, we cannot extrapolate these results beyond 15 waveforms used in the averaging process, because at some point using more waveforms will only add noise to the signal due to the finite number of pulses that

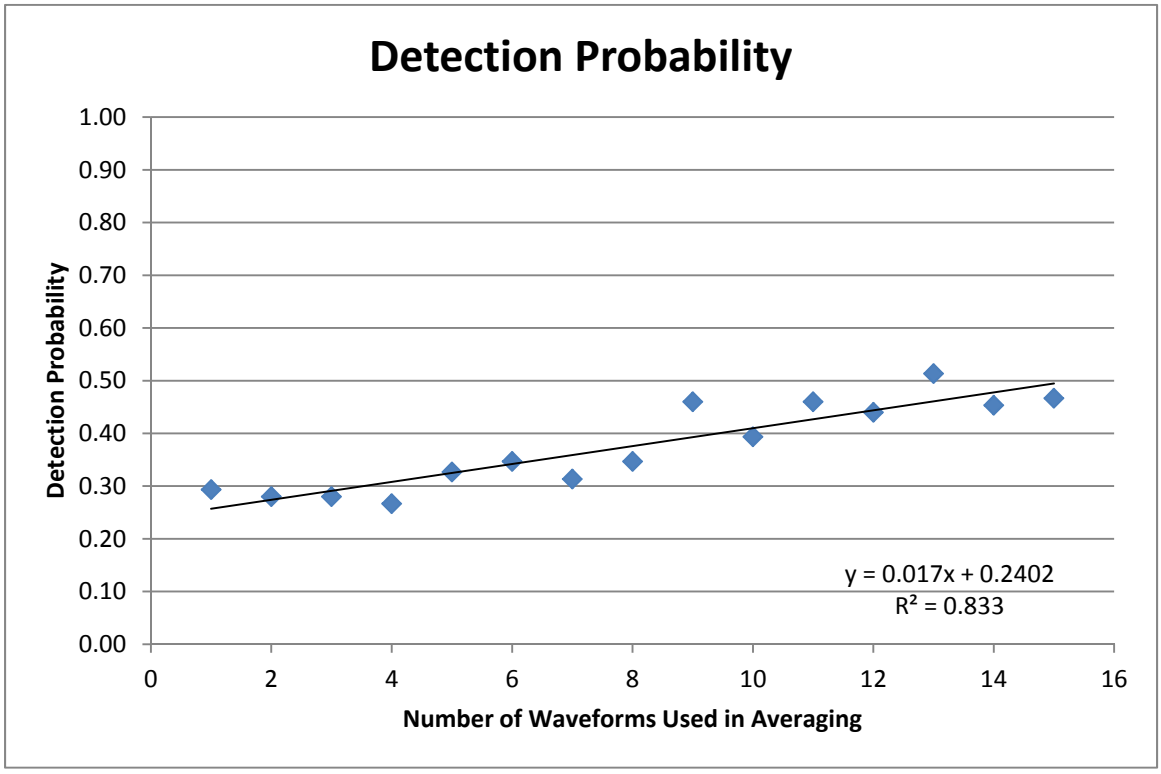

Figure 4.5: Target Detection Probability versus the Number of Waveforms used in the Averaging Process.

actually hit the target. However, these results do support the idea that systems with better coverage rates and redundancy have better chances of successfully detecting a target because more waveforms will actually hit the target, which can then be used in the waveform averaging procedure.

Another important statistic to consider was the "false alarm" rate of the detection algorithm as a function of the number of waveforms used in the averaging process. Using the definition provided in the introduction to this section, Figure 4.6 shows the false alarm rate as a function of the number of waveforms used in the averaging process. As can be seen, the false alarm rate is very low, nearly 0 across all number of waveforms at and above 2. When only one waveform strikes a target, the algorithm is much more susceptible to producing a false alarm (19 out of 150, probability =12.67%), which we

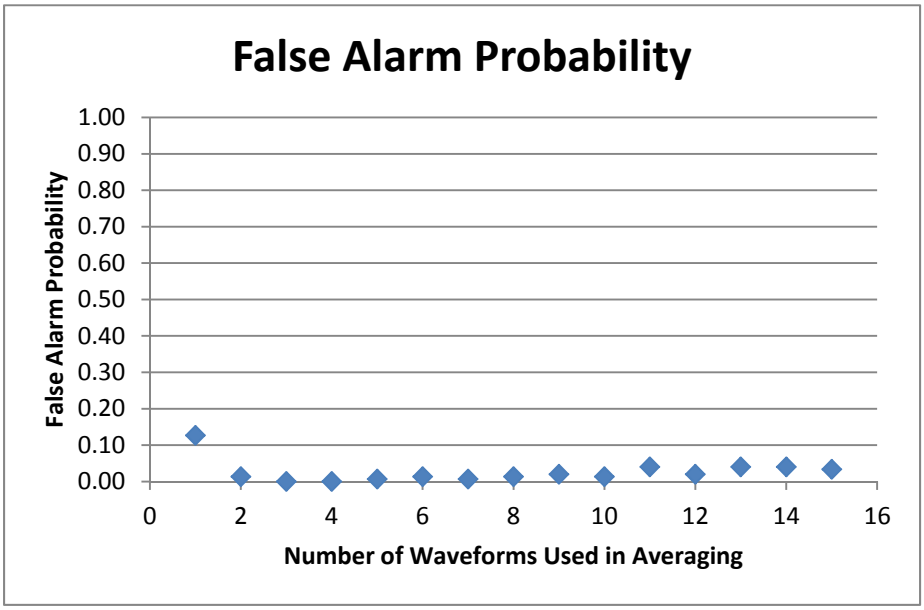

Figure 4.6: False Alarm Probability versus the Number of Waveforms used in the Averaging Process.

would expect as none of the water column noise has been averaged out yet. Since the successful detection rate (Figure 4.5) for only one waveform is 29.33% (44 out of 150), the algorithm is positively identifies a target location 44 out of the 63 times it said there was a target, which represents a 69.8% discrimination rate. In other words, when using only 1 waveform for target detection purposes, 2 out of every 3 target identifications will be correct, which is not an acceptable discrimination rate between successful and unsuccessful detections. However, once two waveforms can be included in the averaging process, the false alarm rate decreases to 1.33% (2 out of 150), while the successful detection rate is 28% (42 out of 150), meaning the algorithm's discrimination rate increases to 95.45% (42 out of 44). This is a much more acceptable level of accuracy when identifying a target within a waveform. Three or more waveforms used in the averaging process maintain the same level of excellent discrimination, while also increasing the number of successful detections. The tables that I used to generate these plots are located in Appendix A.

4.3.2 Dependence on Degree of Inhomogeneity in the Water Column

The next experiment I conducted was to vary the degree of inhomogeneity in the water column (i.e. the degree of variation in the backscattering coefficient, β_π) and observe the effects on the probability of successfully detecting a target. I used the same simulations from the experiment carried out in section 4.3.1, but I sliced the data in a different way to observe these effects. Namely, instead of viewing the detection rate as a function of number of waveforms used in averaging, I viewed the detection rate as a function of target depth in the water column. Then, I split the data into two groups, those with a smaller degree of variation in β_π ($\sigma_{\beta\pi}$ less than or equal to 0.0005 m^{-1}-sr^{-1}) and those with a larger degree of variation in β_π ($\sigma_{\beta\pi}$ larger than 0.0005 m^{-1}-sr^{-1}). Recall, the degree of variation of β_π ranged from 0.0001 to 0.001m^{-1}-sr^{-1}, stepping by 0.0001m^{-1}-sr^{-1}; thus, choosing 0.0005 m^{-1}-sr^{-1} as the midpoint partitioned the data into two subsets of equal size. The objective in doing this was to characterize the difference, if any, in the target detection rate and in the false alarm rate between more homogeneous and less homogeneous coastal waters . To ensure the algorithm was as robust as possible, I only included the simulation results for the averaging of 13, 14, and 15 waveforms in this dataset, since these simulations provided the best target detection results in 4.3.1.

Tables 4.5(a) and 4.5(b) show the target detection and false alarm results as a function of target depth across all degrees of backscattering coefficient variation, respectively. The probability of successfully detecting a target in these conditions is 45.1% (203 out of 450), while the probability of a false alarm is 7.1% (32 out of 450). These values together represent a 86.4% (203 out of 235) discrimination rate in positively identifying a target. The false alarm rate is higher at shallower depths and extremely high at 3 meters (there were no successful detections at 3 meters either). Upon further investigation of the 3-meter target depth simulations, I found that the algorithm identified the target at an estimated depth just outside of the 10% error threshold for all 16 of the

Table 4.5 (a): Detection Probability as a Function of Target Depth for a 1-m target in Waters of Varying Degrees of Inhomogeneity

Target Depth (m)	Detection Probability	Successful Detections	Total Trials
3	0.0000	0	30
4	0.6000	18	30
5	0.5000	15	30
6	0.6667	20	30
7	0.3333	10	30
8	0.3667	11	30
9	0.4000	12	30
10	0.4000	12	30
11	0.3333	10	30
12	0.5333	16	30
13	0.5667	17	30
14	0.7333	22	30
15	0.6667	20	30
16	0.5667	17	30
17	0.1000	3	30

Table 4.5 (b): False Alarm Rate as a Function of Target Depth for 1-m Target in Waters of Varying Degrees of Inhomogeneity

Target Depth (m)	False Alarm Probability	False Detections	Total Trials
3	0.5333	16	30
4	0.0667	2	30
5	0.1333	4	30
6	0.0333	1	30
7	0.0333	1	30
8	0.0000	0	30
9	0.0333	1	30
10	0.1000	3	30
11	0.0667	2	30
12	0.0000	0	30
13	0.0333	1	30
14	0.0000	0	30
15	0.0000	0	30
16	0.0333	1	30
17	0.1000	3	30

false alarm cases. Had the tolerance level been increased slightly (to 12%) all 16 cases would have been re-classified as successful detections.

While I have focused on the absolute values of these probabilities thus far, they are not important when viewed in isolation. The important consideration is to see how these probabilities compare to the corresponding probabilities when the coastal water has smaller variations in the backscattering coefficient. Tables 4.6(a) and (b) show the target detection and false alarm results from for coastal water with less than $0.0005 m^{-1}\text{-}sr^{-1}$ standard deviation in the backscattering coefficient about the mean. The probability of successfully detecting a target in these conditions is 49.3% (111 out of 225), while the probability of a false alarm is 3.1% (7 out of 225). These values together represent a 94.1% (111 out of 118) discrimination rate in positively identifying a target. When comparing these values to their corresponding metrics across all water homogeneities, the successful target detection probability increased (45.1% to 49.3%), the false alarm rate decreased (7.1% to 3.1%), and the discrimination rate increased (86.4% to 94.1%). Thus, the target detection capabilities of an ALB system increase when the coastal water is more homogeneous, which is exactly what we would expect because targets are more easily identifiable in the waveform and spurious noise from the entrained particles are less likely to cause false identification of targets.

Table 4.6 (a): Detection Probability as a Function of Target Depth for a 1-m Target in Relatively More Homogeneous Waters

Target Depth(m)	Detection Probability	Successful Detections	Total Trials
3	0.0000	0	15
4	0.4667	7	15
5	0.4000	6	15
6	0.7333	11	15
7	0.6667	10	15
8	0.4000	6	15
9	0.5333	8	15
10	0.4000	6	15
11	0.5333	8	15
12	0.4667	7	15
13	0.5333	8	15
14	0.8000	12	15
15	0.8000	12	15
16	0.6000	9	15
17	0.0667	1	15

Table 4.6 (b): False Alarm Rate as a Function of Target Depth for 1-m Target in Relatively More Homogeneous Waters

Target Depth(m)	False Alarm Probability	False Detections	Total Trials
3	0.4667	7	15
4	0.0000	0	15
5	0.0000	0	15
6	0.0000	0	15
7	0.0000	0	15
8	0.0000	0	15
9	0.0000	0	15
10	0.0000	0	15
11	0.0000	0	15
12	0.0000	0	15
13	0.0000	0	15
14	0.0000	0	15
15	0.0000	0	15
16	0.0000	0	15
17	0.0000	0	15

4.3.3 Dependence on Target Dimensions

The next experiment I conducted was varying the dimensions of the targets placed in locations between 3m and 17m deep as before in 20-meter coastal water. The objective was to observe the effects of changing the target's cross-sectional area and height on the target probability of successfully detecting a target. I used all combinations of target diameters of 0.5m, 1m, 1.5m, 2m, and 3m with heights of 0.5m, 1m, 1.5m, and 2m. The various environmental and system parameters are summarized in Table 4.7(a) and Table 4.7(b), respectively. Additionally, I varied the reflectance of the targets between values of 0.1, 0.15, and 0.20, and I varied the water's absorption coefficient between values of $0.069m^{-1}$, $0.089\ m^{-1}$, and $0.109m^{-1}$ to increase the number of trials performed at a given depth to make the experiment more robust across different water types. Finally, I decided to use 11 waveforms during waveform averaging.

Table 4.7 (a): Environmental Parameters used to Determine the Effect of Target Dimensions on Detection Probability.

Environmental Parameters	
b_b (m^{-1})	0.007
b_f (m^{-1})	0.229
$\beta(\pi)$ ($m^{-1}sr^{-1}$)	0.005
$\beta(\pi)$-noise ($m^{-1}sr^{-1}$)	0.0005
depth (m)	20

Table 4.7 (b): System Parameters used to Determine the Effect of Target Dimensions on Detection Probability

System Parameters	
Altitude (m)	400
FOV (mrad)	40
Scan Rate (Hz)	27
PRR (kHz)	10
Sampling Rate (Gs/s)	2

Table 4.8 shows the probability of detecting a target with a given cross-sectional diameter at all target depths between 3 and 17 meters. As expected, targets with larger cross-sectional diameter were more likely to be located accurately due to their larger fill factor of the beam as compared to targets of smaller cross-sectional diameter. To get a

Table 4.8: Detection Probabilities for Targets of Various Diameters Located at Depths between 3m and 17m in coastal waters with Absorption Coefficients ranging from $0.069m^{-1}$ to $0.109m^{-1}$

Target Diameter (m)	Detection Probability	Successful Case-1 Detections	Successful Case-2 Detections	Total Trials
0.5	0.0237	8	8	675
1	0.5511	240	132	675
1.5	0.6859	298	165	675
2	0.7378	332	166	675
3	0.7881	407	125	675

better idea of how the target detection probability varies as a function of depth for each target, I plotted the probability of successfully detecting the targets of various cross-sectional diameters versus target depth, as seen in Figure 4.7. From this plot, targets of all cross-sectional diameters were detected with maximum probability 80% over a majority of the shallower target depths and remained at that probability until a precipitous decline to 0%, which varied as a function of diameter. Targets of smaller cross-sectional diameter exhibit detection probability declining to 0% at shallower roll-off depths, while targets with larger cross-sectional diameter exhibit detection probabilities declining to 0% at deeper roll-off depths. This behavior is consistent with what we would expect since larger targets fill a larger portion of the beam size at deeper depths than smaller targets do, thus allowing larger targets to be detected deeper in the water.

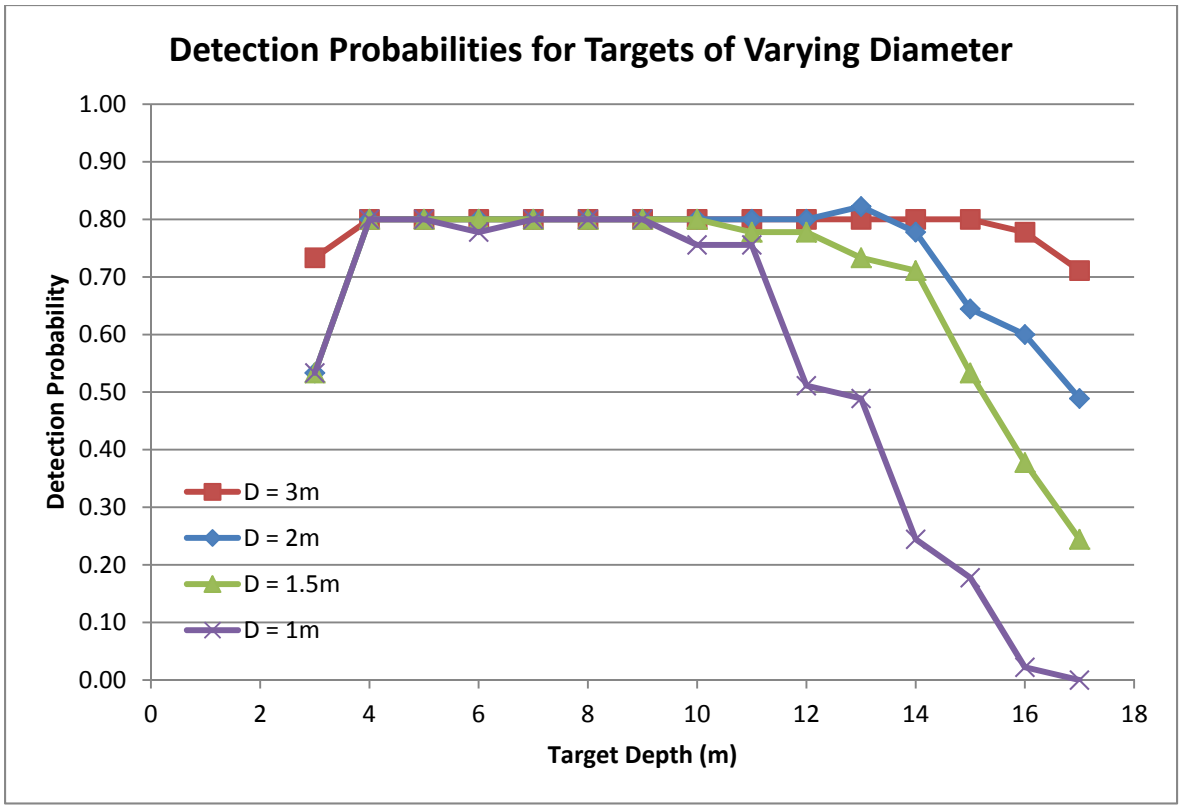

Figure 4.7: The Probability of Successfully Detecting Targets of Various Cross-sectional Diameters versus Target Depth in Waters ranging from Absorption Coefficients of $0.069m^{-1}$ to $0.109m^{-1}$

For more detailed results of successful detections for each target diameter, including the breakdown between case-1 and case-2 detections, Appendix A contains all of the tables with this information. An interesting trend found in those tables is that all targets exhibit the same tradeoff between case-1 and case-2 detections. That is, at shallower depths, target detection is dominated by case-1 detections. However, as the depth increases, case-1 detections begin to decrease and case-2 detections begin to dominate the target detection results. Eventually, case-1 detections cease to occur and only case-2 detections contribute to successful detection of a target. Then, further increasing the depth causes case-2 detections to decrease until they cease to exist as well.

Next, instead of varying the cross-sectional diameter of the target and seeing how the probability of detection changed, I varied the target height and plotted the detection probability as a function of target depth, as seen in Figure 4.8. From these plots, it seems

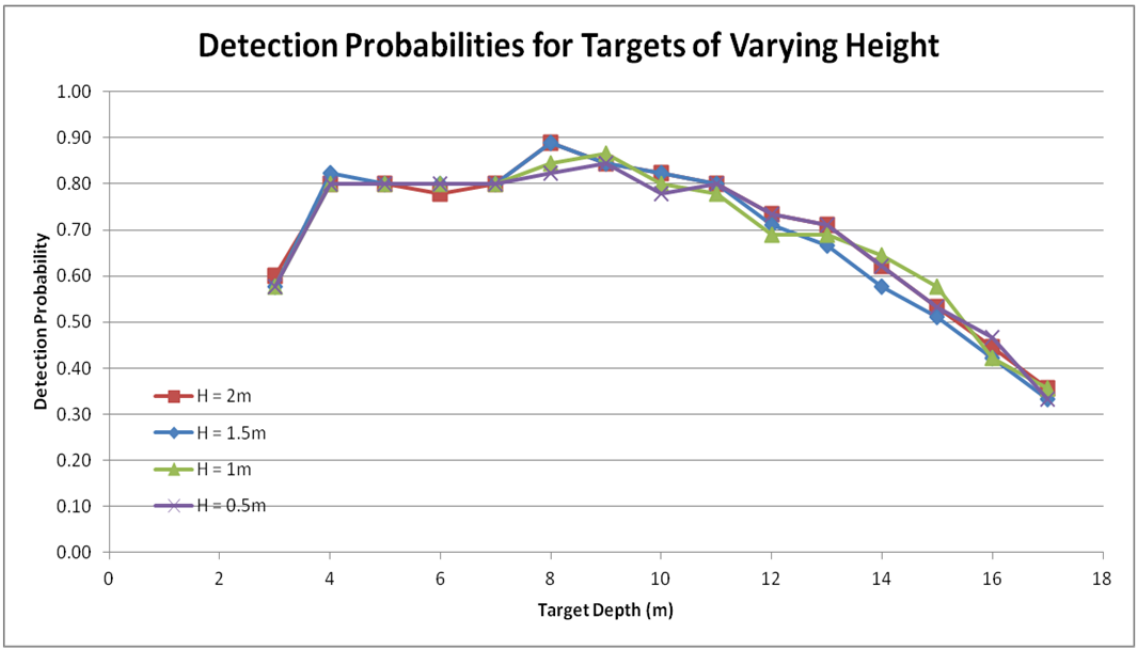

Figure 4.8: The Probability of Successfully Detecting Targets of Various Height versus Target Depth in Waters ranging from Absorption Coefficients of $0.069m^{-1}$ to $0.109m^{-1}$

that target height does not play a role in the probability of successfully detection a target. However, this is merely a function of my simplifying assumptions in the design of the experiment and not representative of reality. Recall that in my experiments all targets are in a plane normally incident and co-located with the transmitted beam's reference ray. Therefore, height has no effect on the fill factor of the beam at a given depth. The only thing height does effect is the amount of energy removed from the signal, as targets with larger height interact with the pulse for a longer amount of time. This should manifest itself in more case-1 detections for targets with larger height, because the seafloor return

is sufficiently weakened so that the algorithm can no longer detect it resulting in the target being labeled as the seafloor. As seen in the tables provided in Appendix A, targets with larger height do produce slightly more case-1 detections than targets of smaller height. In any case, due to my simplifying assumptions, Figure 4.8 is not representative of the way target height affects an ALB system's ability to detect a target.

4.3.4 Dependence on Target Reflectance

The next experiment I conducted was to vary the reflectance of each target and observe the effects on the probability of successfully detecting the target. I used the same simulations from the experiment carried out in section 4.3.3, but I sliced the data in a different way to observe these effects. Namely, instead of viewing the detection rate as a function of the cross-sectional diameter or height, I viewed the detection rate as a function of the target's reflectance. As before, the targets were located at depths between 3m and 17m, spaced at 1-meter intervals, the water's absorption coefficient varied between $0.069m^{-1}$, $0.089m^{-1}$, and $0.109m^{-1}$ and the water depth was 20 meters. Table 4.9 contains the results of this experiment. From these results it can be seen that the probability of detecting a target successfully increases as the target's reflectance value increases. As intuition would suggest, targets with larger reflectance values reflect a greater portion of the incident pulse energy, meaning they should produce distinguishable peaks in the detected return waveform from deeper locations in the water than those that targets with smaller reflectance values would produce. Corroborating this theory, Figure 4.9 shows the detection probability as a function of target depth for the cases of reflectance equal to 0.1, 0.15, and 0.2. All of the curves follow the same general trend: an initial increase in the detection probability, followed by a plateau (aside from reflectance of 0.2 whose curve increases again between and 8 and 10 meters), and then a decreasing roll-off toward 0. It seems that the depth at which roll-off begins to occur is

Table 4.9: Detection Probabilities for Targets of Varying Reflectance Located at Depths between 3m and 17m in coastal waters with Absorption Coefficients ranging from $0.069m^{-1}$ to $0.109m^{-1}$

Target Reflectance	Detection Probability	Successful Case-1 Detections	Successful Case-2 Detections	Total Trials
0.1	0.6400	379	197	900
0.15	0.7011	428	203	900
0.2	0.7389	469	196	900

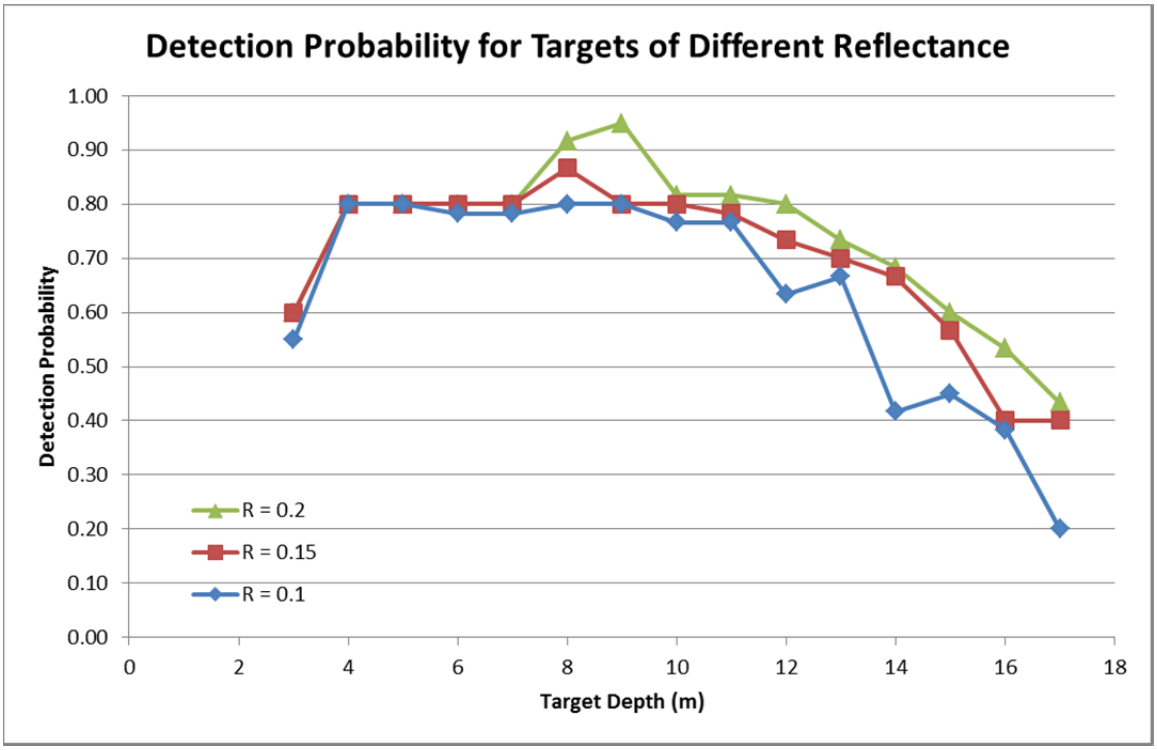

Figure 4.9: The Probability of Successfully Detecting Targets of Various Reflectance Values versus Target Depth in Waters ranging from Absorption Coefficients of $0.069m^{-1}$ to $0.109m^{-1}$

not a function of reflectance, as each of the curves appears to begin its roll-off at the same depth (around 11 meters). However, targets with larger reflectance have a greater detection probability at each of the locations beyond the roll-off point, thus resulting in

the overall greater probability of detecting a target with larger reflectance across the tested range of target depths.

4.3.5 Dependence on Water Turbidity

The next experiment I conducted was varying the turbidity of the water to observe its effects on successfully detecting a given target. To vary the turbidity of the water, I varied the diffuse attenuation coefficient of the water, using the approximation that $K_d = a + b_b$. I examined three separate water conditions: K_d equal to $0.08m^{-1}$, $0.12m^{-1}$, and $0.25m^{-1}$. For this simulation, targets were located between 3m and 25m deep, spaced at 1-meter intervals, in coastal water with a depth of 30 meters. The system parameters I used for this simulation are summarized in Table 4.10. Again, I used 11 waveforms in the averaging procedure.

Table 4.10: System Parameters used to Determine the Effect of Water Turbidity on Successful Target Detection Rates.

System Parameters	
Altitude (m)	400
FOV (mrad)	40
Scan Rate (Hz)	27
PRR (kHz)	10
Sampling Rate (Gs/s)	2

The target detection probability for a 2-meter diameter target with 2-meter height under various water turbidities as a function of the optical path length traveled in the water is plotted in Figure 4.10. As seen in the plot, the probability of successfully detecting this target is unity at shallower depths until a steep roll-off occurs at greater depths. The roll-off depth is a function of the water turbidity, much like the roll-off depth was a function of cross-sectional diameter in section 4.3.3. For less turbid waters, the

roll-off depth is deeper, while for more turbid waters, the roll-off depth is shallower. From my simulation results, waters with K_d of $0.08m^{-1}$ exhibit roll-off after the pulse has traveled approximately 15 meters in the water; waters with K_d of $0.12m^{-1}$ exhibit roll-off after the pulse has traveled approximately 12 meters in the water; and, waters with K_d of $0.25m^{-1}$ exhibit roll-off after the pulse has traveled approximately 8 meters in the water.

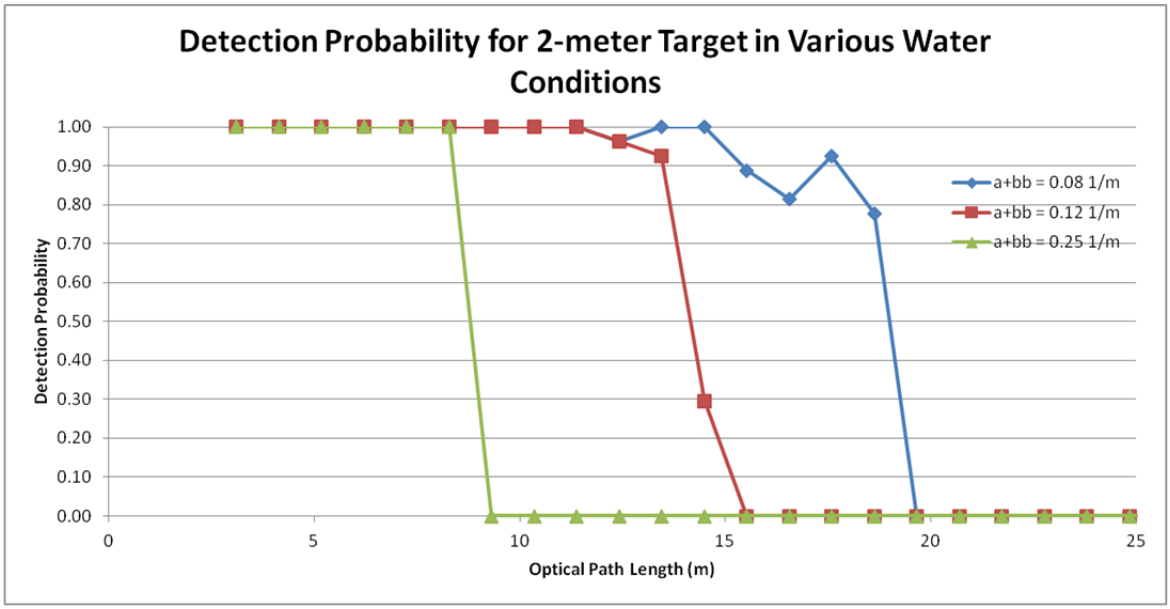

Figure 4.10: The Probability of Successfully Detecting a 2-meter Target in Waters of Varying Diffuse Attenuation Coefficient

The target detection probability for a 1-meter diameter target with 1-meter height under various water turbidities as a function of the optical path length traveled in the water is plotted in Figure 4.11. As is the case with the 2-meter target, the probability of successfully detecting this target is unity at shallower depths until a steep roll-off occurs at greater depths. Again, the roll-off depth is a function of the water turbidity; for less turbid waters, the roll-off depth is deeper, while for more turbid waters, the roll-off depth is shallower. However, the roll-off depths occur at shallower depths for a 1-meter target

than they do for the 2-meter target. From my simulation results, waters with K_d of $0.08m^{-1}$ exhibit roll-off after the pulse has traveled approximately 13 meters in the water; waters with K_d of $0.12m^{-1}$ exhibit roll-off after the pulse has traveled approximately 9 meters in the water; and, waters with K_d of $0.25m^{-1}$ exhibit roll-off after the pulse has traveled approximately 4 meters in the water. Combining the results from both of these

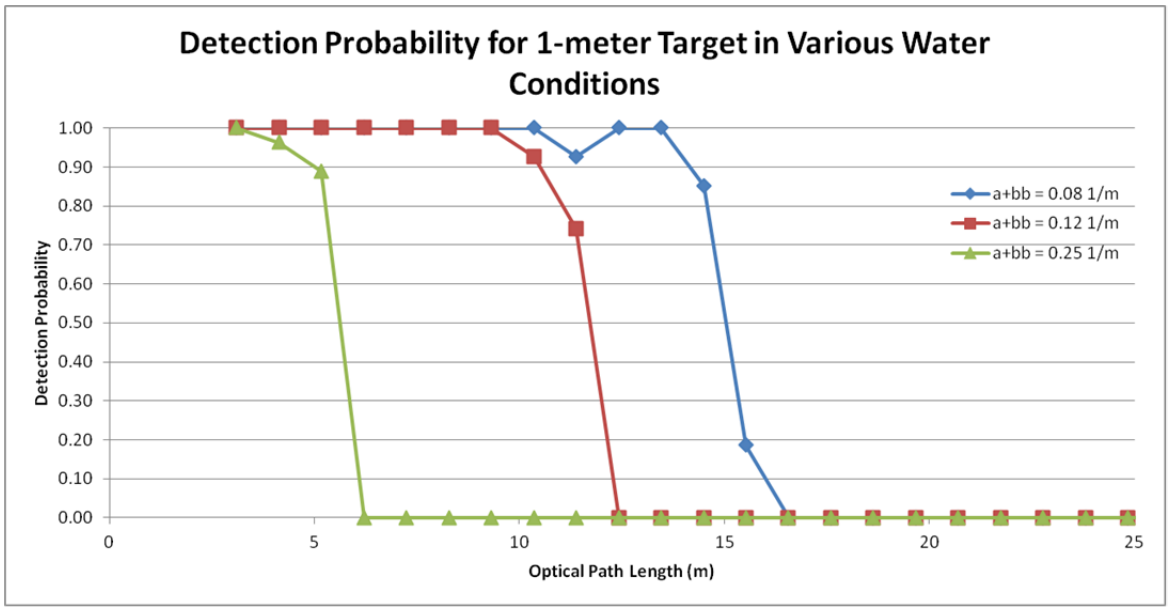

Figure 4.11: The Probability of Successfully Detecting a 1-meter Target in Waters of Varying Diffuse Attenuation Coefficient

plots, it is clear that targets located in less turbid waters have higher probabilities of being detected by an ALB system because targets can be located at greater depths for less turbid waters. Moreover, larger targets can be detected deeper than smaller targets in more turbid waters, consistent with the results presented in section 4.3.3. The tables I used to produce Figures 4.10 and 4.11 can be found in Appendix A.

4.3.6 Dependence on Receiver's Field-of-View

The final experiment I conducted was varying the receiver's FOV to observe the effects on successfully detecting a given target in various water conditions. I used the same three water conditions as described in section 4.3.5. As in that experiment, 1-m targets were located between 3m and 25m deep, spaced at 1-meter intervals, in coastal water with a depth of 30 meters. The system parameters I used for this simulation are summarized in Table 4.11. Again, I used 11 waveforms in the averaging procedure.

Table 4.11: System Parameters used to Determine the Effect of Receiver's FOV on Successful Target Detection Rates.

System Parameters	
Altitude (m)	400
Scan Rate (Hz)	27
PRR (kHz)	10
Sampling Rate (Gs/s)	2

Figures 4.12 – 4.14 plot the effects of varying the receiver's FOV on the probability of detecting a target as a function of optical path length traveled in the water. As can be seen in these three plots, the general shape of the curves is the same across all types of coastal waters: the detection probability is unity at shallow depths until it undergoes a steep roll-off at some depth. For less turbid waters ($K_d = 0.08m^{-1}$), the roll-off depth is deeper in the water, while for more turbid waters ($K_d = 0.25m^{-1}$), the roll-off depth is much shallower. Regardless of water type, larger receiver FOVs can detect targets deeper in the water than smaller FOVs can. However, in clearer waters, the effect of receiver FOV is less pronounced, as the roll-off depth for a 20-mrad system appears to be around 12 meters, while the roll-off depth for a 40-mrad system is around 15 meters. This represents a 25% increase in detection depth for a 100% increase in the receiver

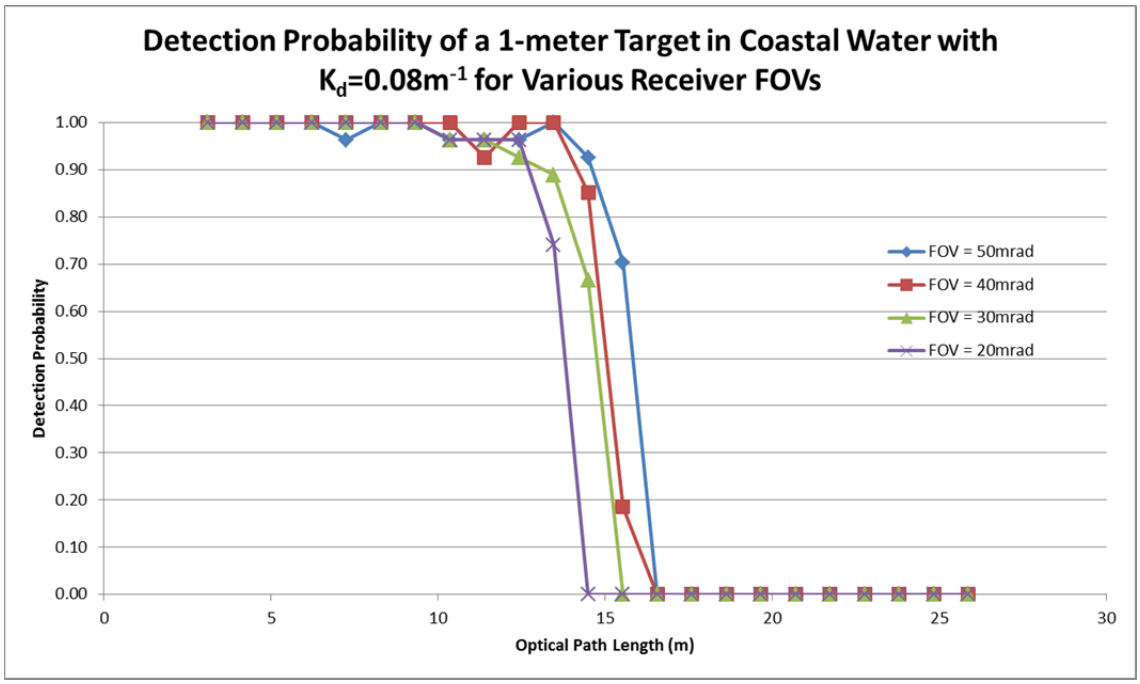

Figure 4.12: The Probability of Successfully Detecting a 1-meter Target with Various Receiver FOVs in Coastal Water with K_d=0.08m^{-1}

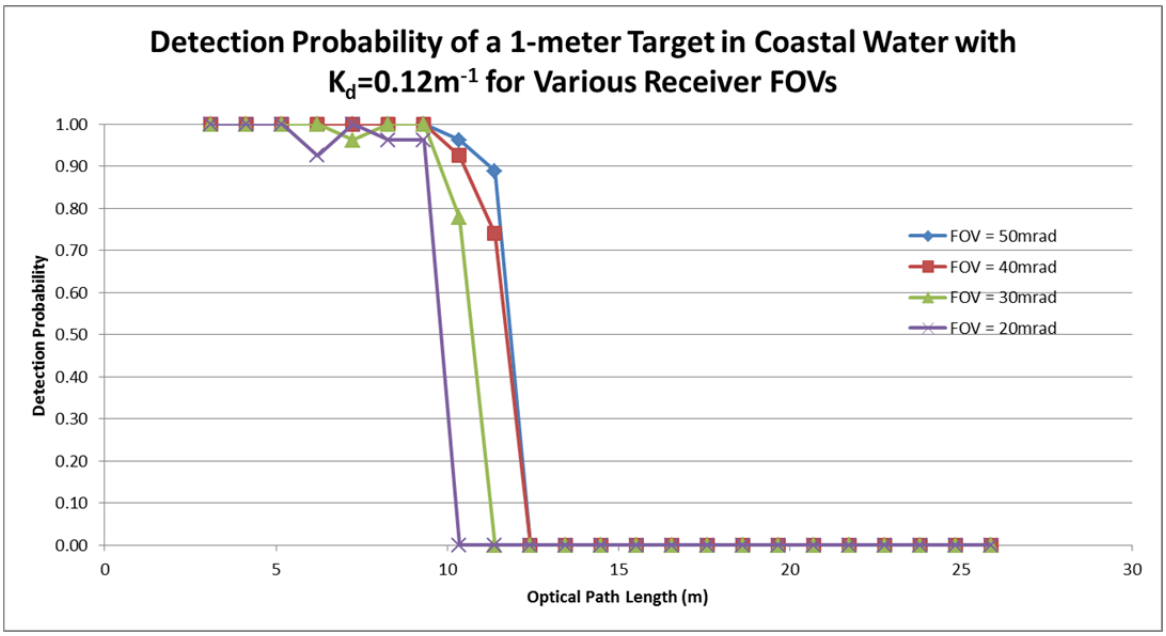

Figure 4.13: The Probability of Successfully Detecting a 1-meter Target with Various Receiver FOVs in Coastal Water with K_d=0.12m^{-1}

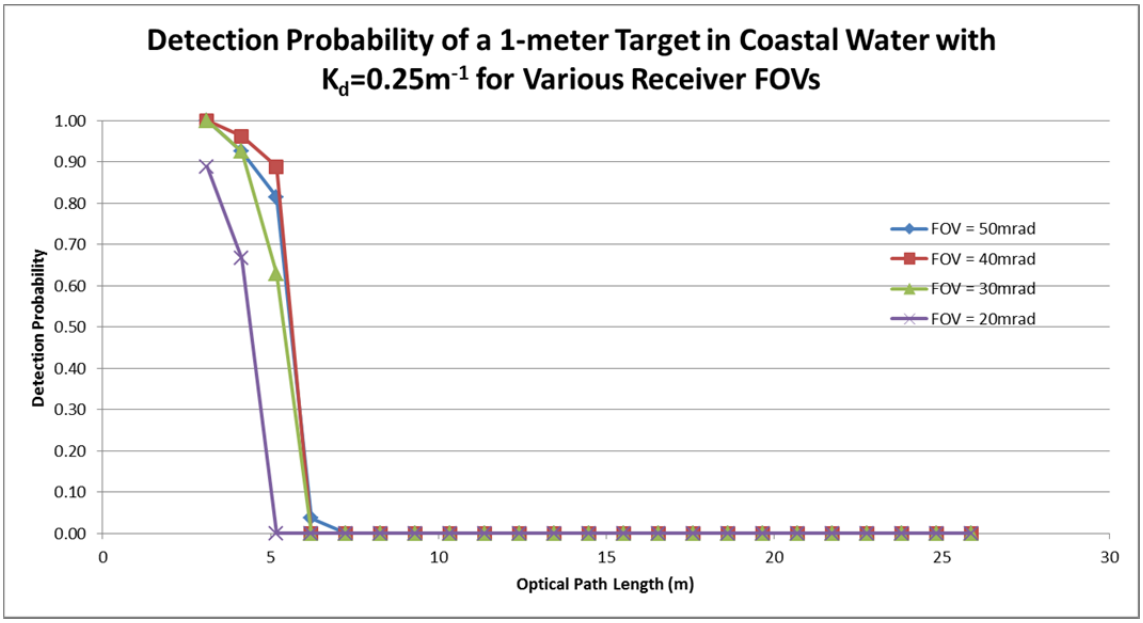

Figure 4.14: The Probability of Successfully Detecting a 1-meter Target with Various Receiver FOVs in Coastal Water with K_d=0.25m^{-1}

FOV. This stands in contrast to the more turbid water case in which the roll-off depth is around 3 meters for the 20-mrad system, while the roll-off depth for the 40-mrad system is approximately 6 meters. This represents a 100% increase in detection depth for a 100% increase in the receiver FOV. Thus, these results suggest that ALB systems employing a larger receiver FOV can detect targets significantly better in shallow, turbid waters than can ALB system employing a smaller FOV. All of the tables that I used to produce these plots can be found in Appendix A.

4.4 Conclusion

The results presented in this chapter are completely theoretical in nature. The YellowJacketSimulator, utilizing my model of the FOV loss factor (Chapter 3), and the Geometric Simulator tool I developed outlined in Chapter 2 and Section 4.2.1,

respectively, produced all of the modeled ALB waveform data. I embedded these simulators in EOSL's TMT, which allowed me to run more than 100,000 simulations over the course of this research, producing a robust set of results for a given ALB system subjected to various environmental- and system-input combinations, under varying noise conditions. Although I could not obtain experimental data to validate my theoretical waveforms at the time of this research, the results contained herein should be representative of the trends in the target detection capabilities of an ALB system. The following list summarizes the trends I found:

1) Targets illuminated by more pulses are better detected by an ALB system, regardless of inhomogeneity of the water column.
2) More inhomogeneity in the water column leads to larger false alarm rates.
3) Targets with larger cross-sectional features are better detected by an ALB system.
4) Targets with larger reflectance values can be detected better than targets with smaller reflectance values. The roll-off point appears to be independent of reflectance. However, targets with larger reflectance have greater detection probabilities than those with smaller reflectance at depths beyond the roll-off point.
5) There is a trade-off between case-1 and case-2 detections until case-1 cease to exist, after which point case-2 detections also cease to exist shortly thereafter.
6) Targets located in more turbid waters are less likely to be detected than targets in less turbid waters. The maximum detectable depths of targets in less turbid waters is greater than the maximum detectable depth in more turbid waters.
7) ALB systems that employ larger receiver FOVs can detect targets deeper in the water than system that employ smaller FOVs. The most pronounced difference between the performances of receivers with different FOVs is in

shallow, turbid waters, where doubling the receiver FOV can result in a doubled maximum detectable depth.

8) Typical detection probability curves exhibit unit probability of detection until some roll-off, after which the decline in probability of detection is very steep. Larger targets cause the roll-off depth to be shifted to greater depths, as do smaller diffuse attenuation coefficient values, and larger receiver FOVs.

All of these results, in terms of trends and shapes of curves, match very well with those presented by Guenther [33] and by Yang and LaRocque [1]. However, it seems the roll-off depths, or maximum detection depths, for my simulated system are shallower than those presented by the aforementioned groups. This is probably due to a lack of algorithmic sophistication, since we have yet to implement improved shallow water detection algorithms or improved case-3 target (type-2 detection) identification procedures.

Moving forward, I would like to be able to estimate the height of the targets. Perhaps this could be derived from the FWHM of the target-induced peak. Additionally, I would like to look into estimating the reflectance of the target, although this will be difficult because the peak intensity depends on the combination of fill factor within the water column and the target's reflectance value. Hopefully when our groups implements our DEM tool, providing us with an aggregation of the waveforms in three-dimensions, we can look at developing algorithms to merge multiple waveforms to estimate cross section and reflectance. Finally, with more time, I would like to characterize the decreasing marginal return of using more waveforms in the averaging process. At some point, the linear increase should slow and actually deteriorate as we add more waveforms in the averaging process, since the new waveforms added to the averaging process no longer contribute information regarding the target. The geometric simulator tool that I developed should allow me to do this, as I simply need to decrease the coverage rate of

the system, restricting the number of pulses that interact with the target to a smaller amount.

CHAPTER 5

CONCLUSION

5.1 Summary of Contributions

In performing the work to complete my research on an ALB system's target detection capabilities, I was the main person responsible for developing our LIDAR team's bathymetric data processing infrastructure. This entailed developing the majority of the IDL code from scratch, developing a waveform simulator that solves the radiative transfer equation under varying system and environmental situations, implementing post-processing algorithms (depth extraction, estimation of IOPs, etc.), and integrating other team members' code into the data processing architecture. I also completed the basic design of the YellowJacketSimulator, the software combination of my waveform simulator with a GUI. I designed the YellowJacketSimulator as a modular data processing architecture that allows for tremendous flexibility in changing system and environmental inputs to examine the effectiveness of an ALB system in different situations. Its seamless integration into TMT to produce the hundreds of thousands of unique simulations used to analyze the target detection capabilities of ALB system is a testament to the modularity and flexibility of the simulation environment I created. Finally, and most importantly, with the creation of the YellowJacketSimualtor, GTRI is now one of the few institutions in the world to possess a bathymetric lidar simulator, a staple of industry-leading ALB system design.

By studying ocean optics, light-water interaction, and the SHOALS and CZMIL ALB systems, I developed an in-depth characterization of the bathymetric lidar equation. I explained the origin of the equation, how the two most prevalent forms of the equation

are equivalent, and how Linear Systems theory can be used to model the return waveform by treating the bathymetric lidar equation as an impulse response function. Additionally, I developed an empirical characterization and approximation of the FOV factor, the important term in the bathymetric lidar equation that accounts for the loss of photons that have scattered outside of the receiver's FOV. This characterization provides GTRI the capability to simulate FOV loss functions in real time, allowing for effective examination of the tradeoffs in the ALB system design space. Furthermore, this capability supports the geophysical inversion of the bathymetric lidar equation to estimate seafloor reflectance, which we may be able to perform in real time in the future, a feat that has yet to be accomplished.

Finally, I have produced a thorough, theoretical exploration of the target detection capabilities of an ALB system. I characterized the trends in an ALB system's target detection capabilities by performing six case studies, each intended to examine an important aspect of target detection, resulting in the simulation of over 100,000 unique simulations. The results and analysis contained in Chapter 4 corroborate previous ALB target detection studies published in literature. However, explicitly showing the dependence of the target detection capabilities of an ALB system on its receiver's FOV in various water conditions is something that has yet to be published in literature, and is thus a borderline novel contribution to the field of ALB. Lastly, this work has contributed to the conceptual design of the ALB system we intend to build at EOSL. Producing these types of results signifies that our group understands the intricacies involved with designing successful ALB systems and improves our credibility with potential sponsors.

5.2 Future Work

Within the coming weeks, our group will begin assembly of the laboratory lidar. I will be assisting in the assembly of the transmitting and receiver optics, both of which I helped design. I will also assist with the characterization of the laser and the PMTs that we purchased, which will allow me to model our system with its realized characteristics in my waveform simulator. After we characterize and assemble our lidar, we will begin performing water tank experiments, one of which we will be a target detection experiment. I hope to use data from this collection to validate the theoretical study I have performed in this work.

In the future, I hope to create a voxelization of the water column that effectively produces averaged waveforms over a water column. Using this new data product, I would subsequently like to use image processing techniques (e.g. Canny edge detection) in multiple planes of the image cube with the intention of discovering anomalies or interest points that otherwise would not have been found. Perhaps some of these interest points will be indicators of targets that were previously undetectable using only the typical depth return measurements. This work would require further coding in IDL and ENVI, creating new software that associates all of the points from the individual waveforms with geospatial locations in a three-dimensional space.

Finally, as a potential for doctorate-level work in the future, I believe that there is an opportunity to examine the FOV loss function in more detail to understand the effects varying a receiver's FOV on the detected return signal. From this research, it could be possible to develop a better model of the FOV loss function and implement a real time algorithm to estimate the FOV loss factor, allowing for real time estimation of seafloor reflectance.

APPENDIX A

SUPPLEMENTARY FIGURES AND TABLES

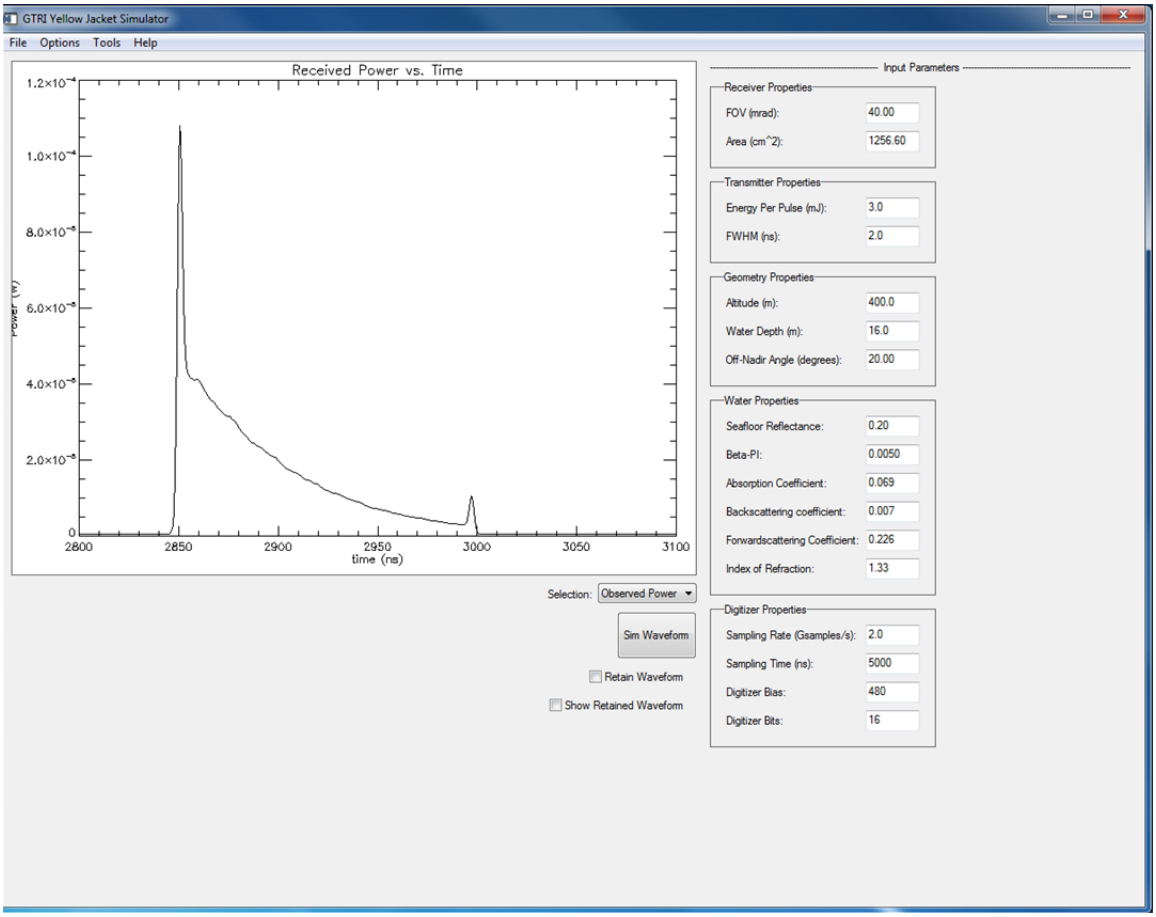

Figure A.1: Screenshot of YellowJacketSimulator Displaying Observed Power Incident on Receiver versus Time for a Given Set of Environmental and System Parameters

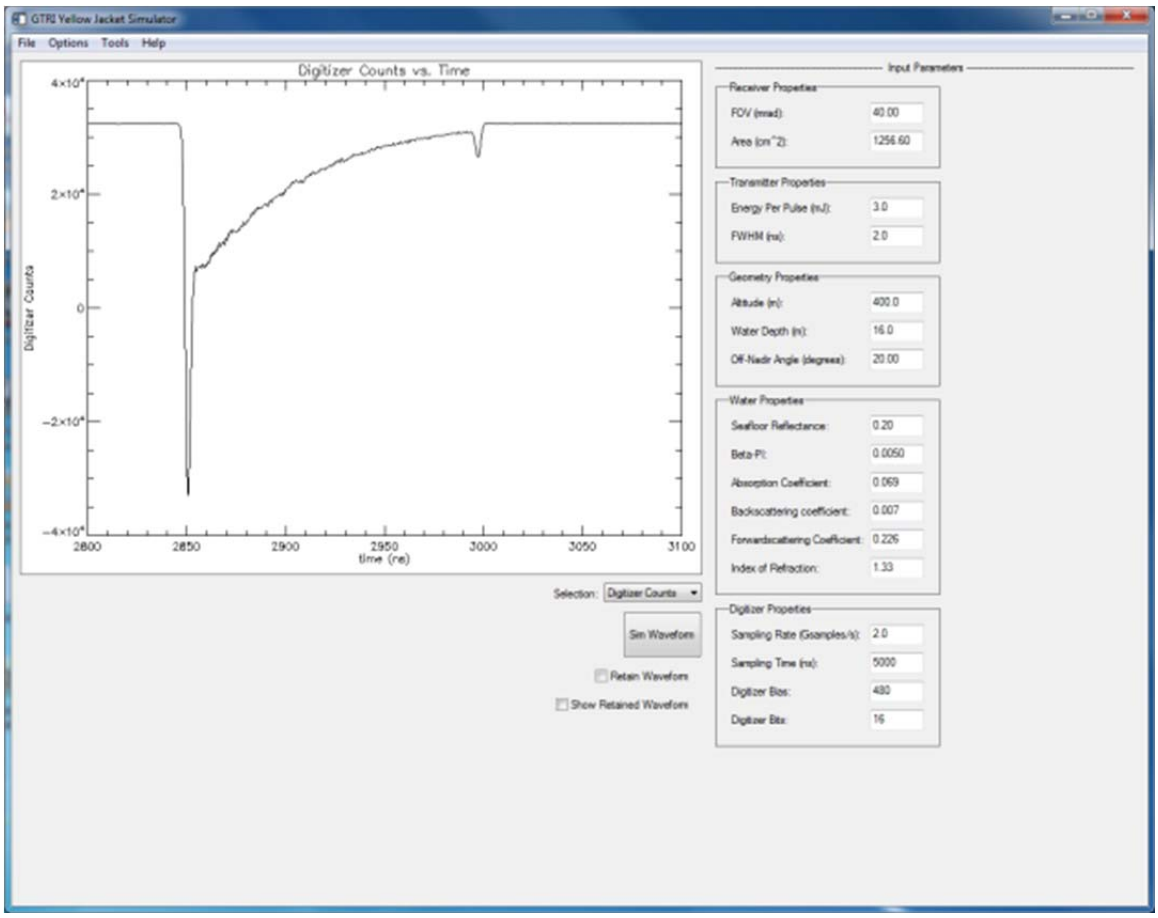

Figure A.2: Screenshot of YellowJacketSimulator Displaying the same Waveform as Figure A.1 except in Digitizer Counts (the output of the Digitizer) versus Time

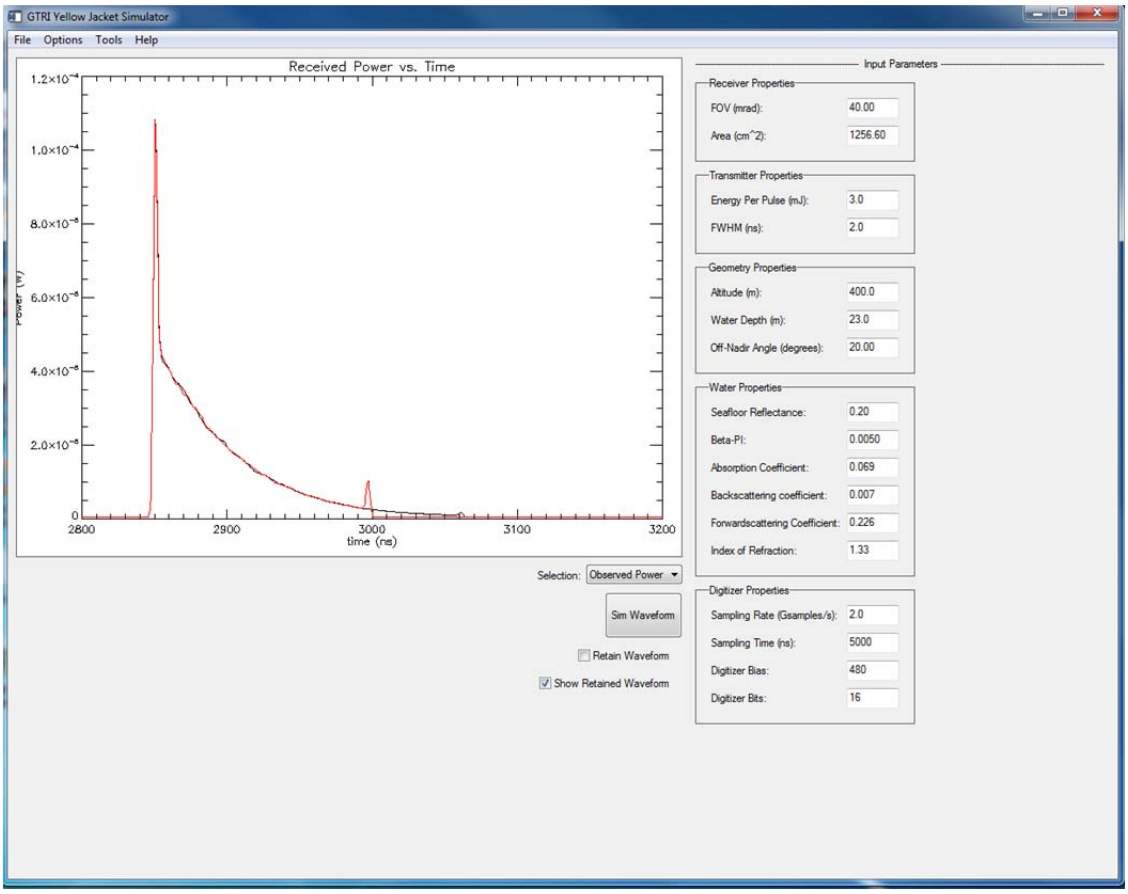

Figure A.3: Screenshot of YellowJacketSimulator Comparing Two Waveforms of Resulting from Different Seafloor Depths (Red Curve is Shallower Depth)

The following four plots show the well-behaved trends of the four coefficients of the FOV loss factor model as a function of beam attenuation coefficient.

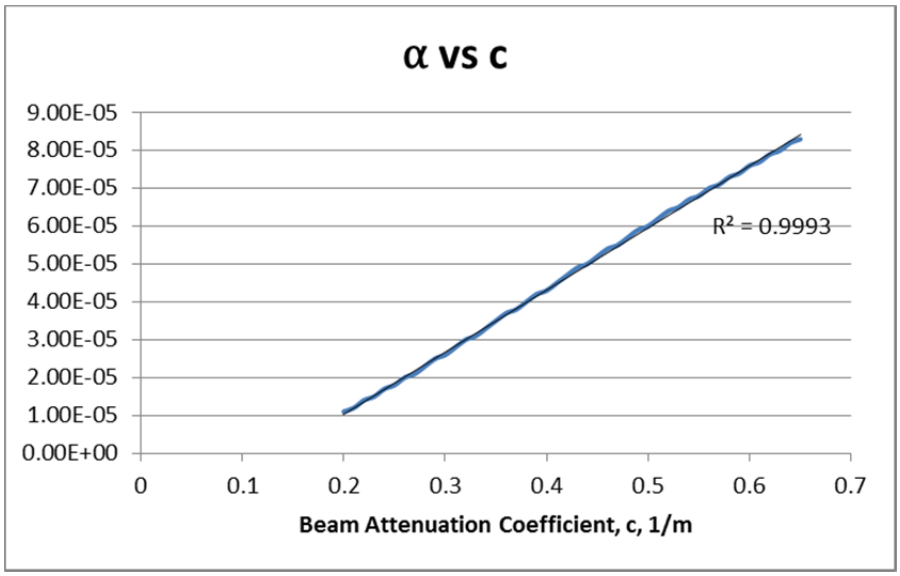

Figure A.4: The Variation of the FOV model's α-coefficient as a function of the seawater's beam attenuation coefficient, c

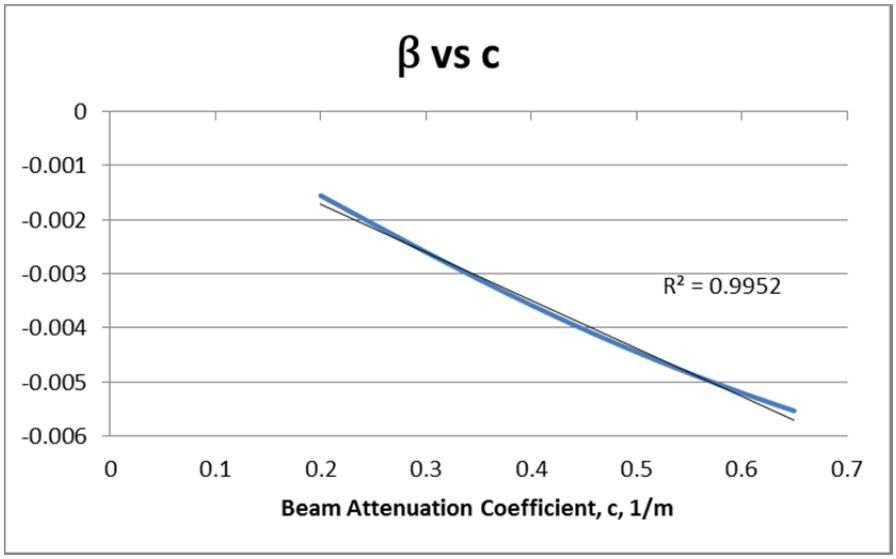

Figure A.5: The Variation of the FOV model's β-coefficient as a function of the seawater's beam attenuation coefficient, c

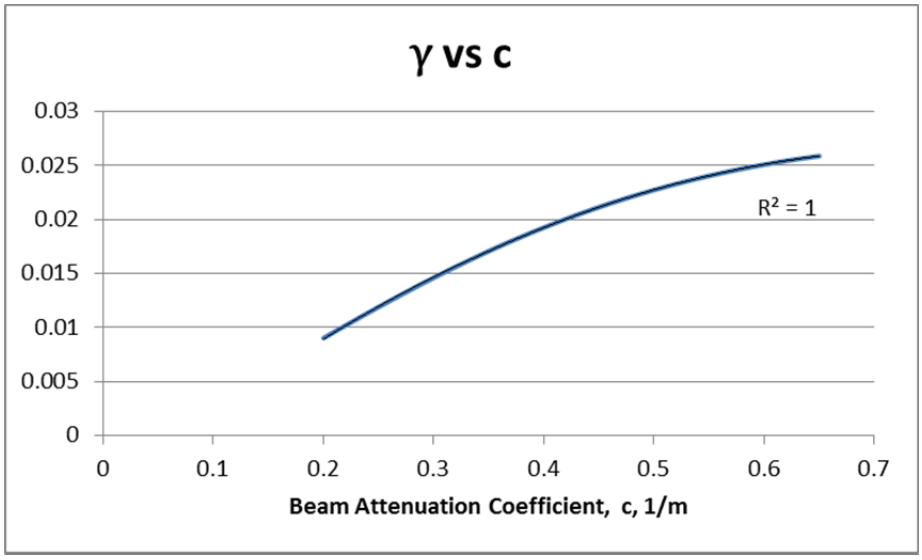

Figure A.6: The Variation of the FOV model's γ-coefficient as a function of the seawater's beam attenuation coefficient, c

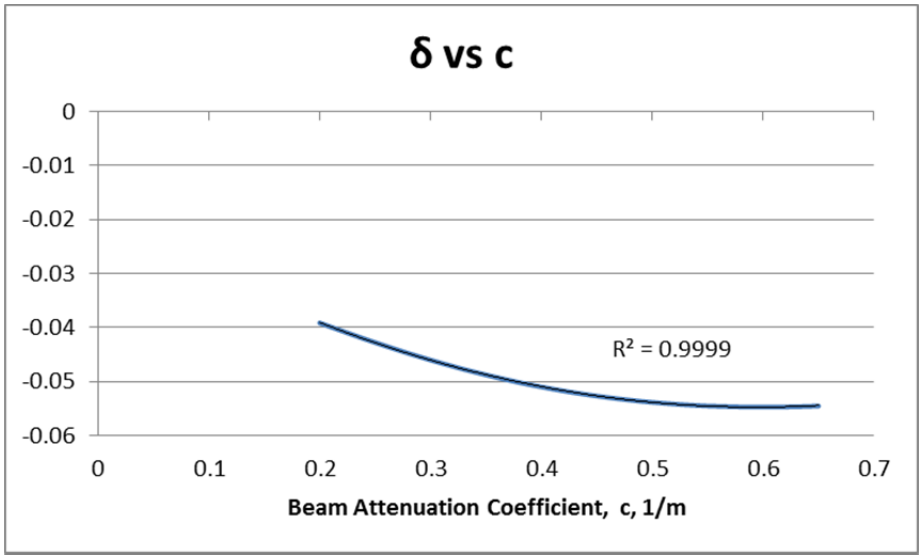

Figure A.7: The Variation of the FOV model's δ-coefficient as a function of the seawater's beam attenuation coefficient, c

The following eight plots correspond to each of the eight cases presented in Table 3.2, highlighting the accuracy of the proposed FOV model with the actual FOV loss function.

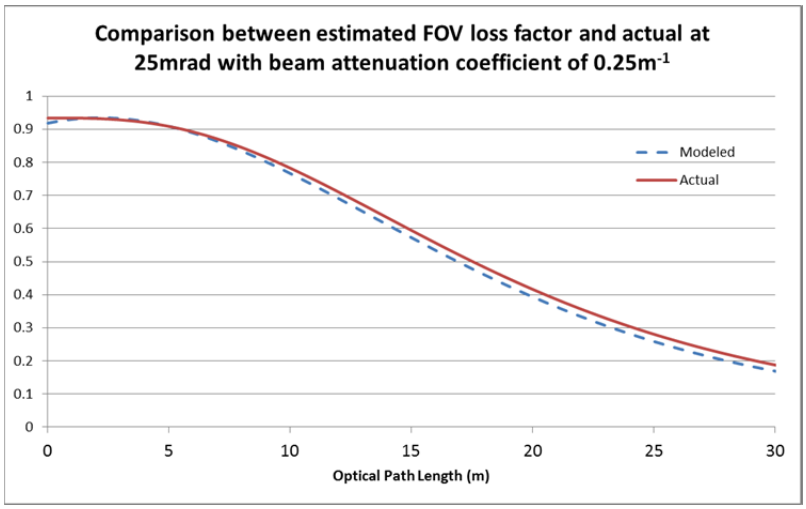

Figure A.8: Comparison between the Modeled FOV Loss Function and the Actual FOV Loss Function for an ALB system with a 25-mrad FOV surveying coastal water with $c=0.25m^{-1}$

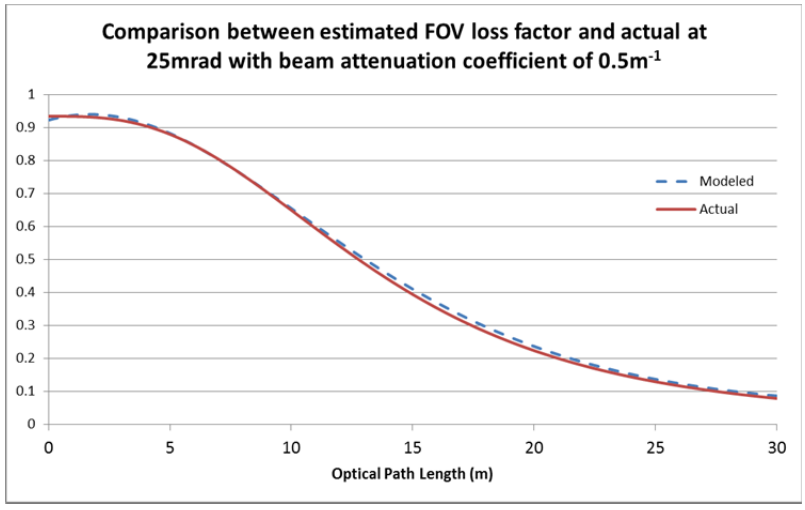

Figure A.9: Comparison between the Modeled FOV Loss Function and the Actual FOV Loss Function for an ALB system with a 25-mrad FOV surveying coastal water with $c=0.5m^{-1}$

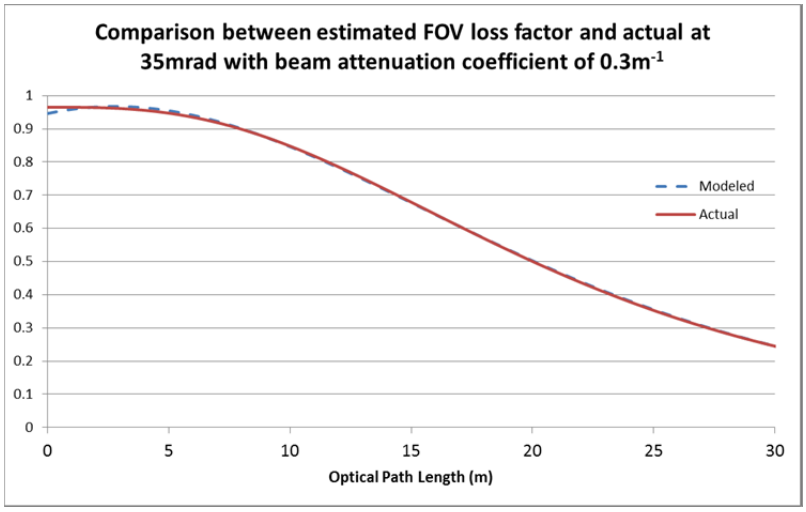

Figure A.10: Comparison between the Modeled FOV Loss Function and the Actual FOV Loss Function for an ALB system with a 35-mrad FOV surveying coastal water with $c=0.3m^{-1}$

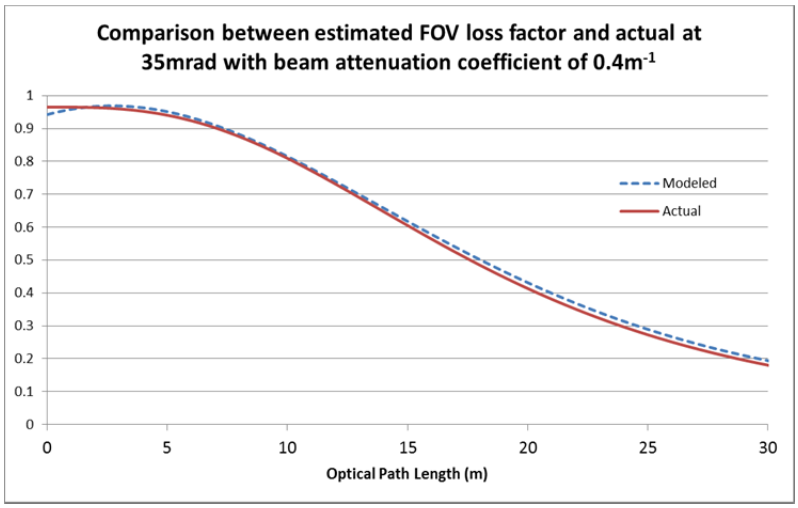

Figure A.11: Comparison between the Modeled FOV Loss Function and the Actual FOV Loss Function for an ALB system with a 35-mrad FOV surveying coastal water with $c=0.4m^{-1}$

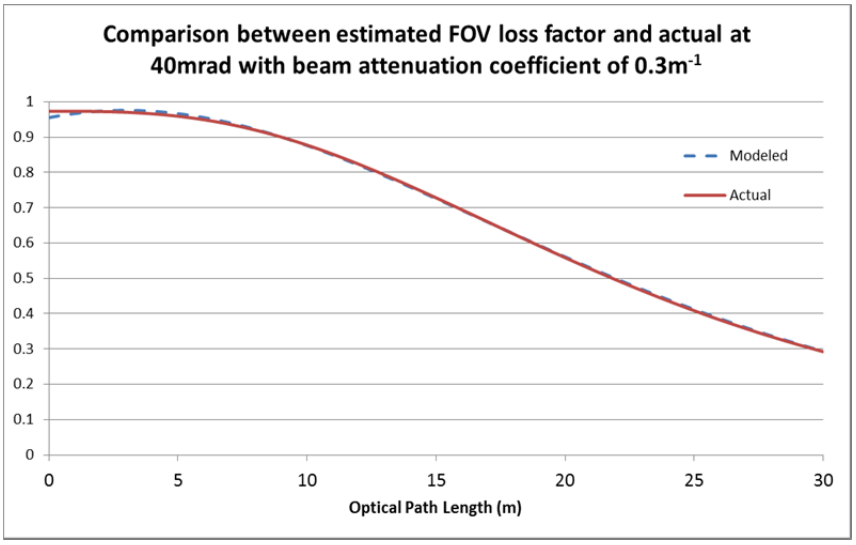

Figure A.12: Comparison between the Modeled FOV Loss Function and the Actual FOV Loss Function for an ALB system with a 40-mrad FOV surveying coastal water with $c=0.3m^{-1}$

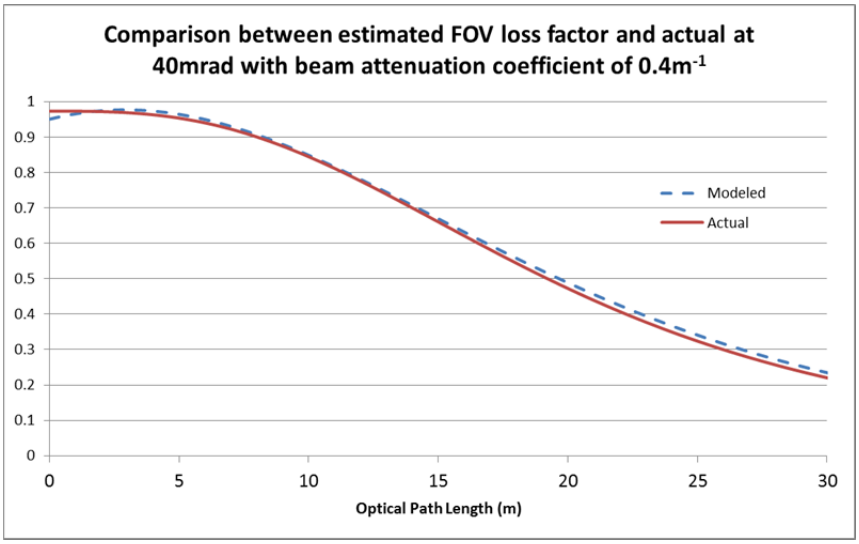

Figure A.13: Comparison between the Modeled FOV Loss Function and the Actual FOV Loss Function for an ALB system with a 40-mrad FOV surveying coastal water with $c=0.4m^{-1}$

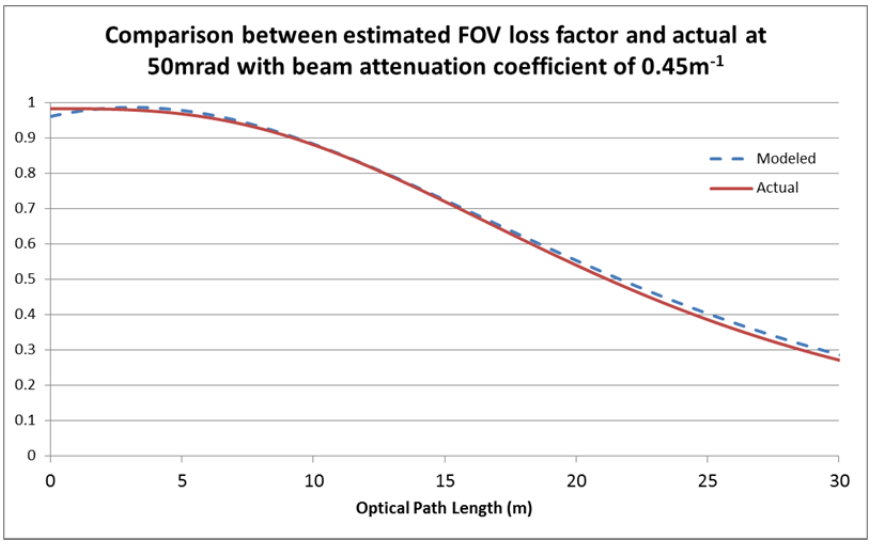

Figure A.14: Comparison between the Modeled FOV Loss Function and the Actual FOV Loss Function for an ALB system with a 50-mrad FOV surveying coastal water with $c=0.45m^{-1}$

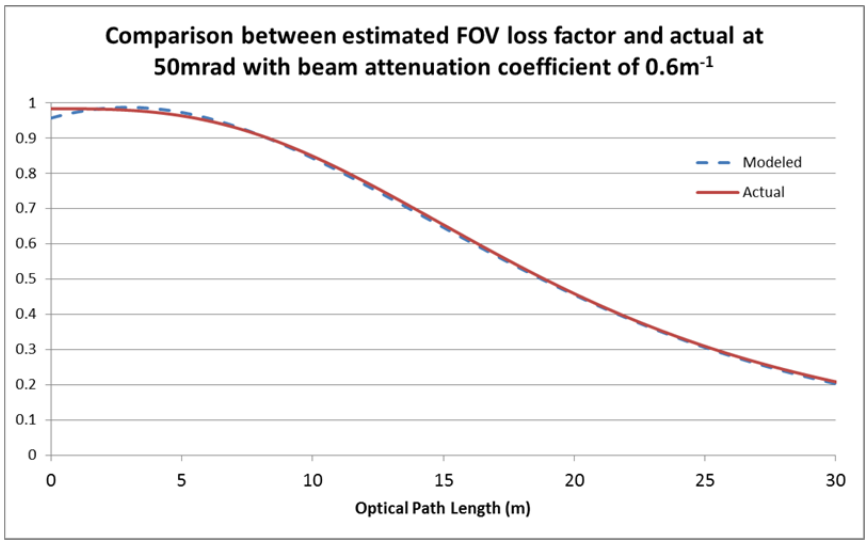

Figure A.15: Comparison between the Modeled FOV Loss Function and the Actual FOV Loss Function for an ALB system with a 50-mrad FOV surveying coastal water with $c=0.6m^{-1}$

The following two tables contain the data used in Figures 4.5 and 4.6, respectively.

Table A.1: Target Detection Probability versus the Number of Waveforms used in the Averaging Process

Waveforms	Detection Probability	Successful Detections	Total Trials
1	0.2933	44	150
2	0.2800	42	150
3	0.2800	42	150
4	0.2667	40	150
5	0.3267	49	150
6	0.3467	52	150
7	0.3133	47	150
8	0.3467	52	150
9	0.4600	69	150
10	0.3933	59	150
11	0.4600	69	150
12	0.4400	66	150
13	0.5133	77	150
14	0.4533	68	150
15	0.4667	70	150

Table A.2: False Alarm Probability versus the Number of Waveforms used in the Averaging Process

Waveforms	False Alarm Probability	False Detections	Total Trials
1	0.1267	19	150
2	0.0133	2	150
3	0.0000	0	150
4	0.0000	0	150
5	0.0067	1	150
6	0.0133	2	150
7	0.0067	1	150
8	0.0133	2	150
9	0.0200	3	150
10	0.0133	2	150
11	0.0000	6	150
12	0.0200	3	150
13	0.0400	6	150
14	0.0400	6	150
15	0.0333	5	150

The following four tables contain the data used to produce Figure 4.7.

Table A.3: Probability of Detecting a 3-meter, Cross-sectional Diameter Target versus in Waters ranging from Absorption Coefficients of $0.069m^{-1}$ to $0.109m^{-1}$

Target Depth (m)	Detection Probability	Successful Case-1 Detections	Successful Case-2 Detections	Total Trials
3	0.7333	33	0	45
4	0.8000	30	6	45
5	0.8000	26	10	45
6	0.8000	24	12	45
7	0.8000	25	11	45
8	0.8000	32	4	45
9	0.8000	31	5	45
10	0.8000	30	6	45
11	0.8000	30	6	45
12	0.8000	28	8	45
13	0.8000	26	10	45
14	0.8000	25	11	45
15	0.8000	24	12	45
16	0.7778	23	12	45
17	0.7111	20	12	45

Table A.4: Probability of Detecting a 2-meter, Cross-sectional Diameter Target in Waters ranging from Absorption Coefficients of $0.069m^{-1}$ to $0.109m^{-1}$

Target Depth (m)	Detection Probability	Successful Case-1 Detections	Successful Case-2 Detections	Total Trials
3	0.5333	24	0	45
4	0.8000	24	12	45
5	0.8000	24	12	45
6	0.8000	24	12	45
7	0.8000	24	12	45
8	0.8000	26	10	45
9	0.8000	25	11	45
10	0.8000	24	12	45
11	0.8000	25	11	45
12	0.8000	24	12	45
13	0.8222	24	13	45
14	0.7778	23	12	45
15	0.6444	17	12	45
16	0.6000	16	11	45
17	0.4889	8	14	45

Table A.5: The Probability of Successfully Detecting a Target with 1.5-meter Cross-sectional Diameter versus Target Depth in Waters ranging from Absorption Coefficients of $0.069m^{-1}$ to $0.109m^{-1}$

Target Depth (m)	Detection Probability	Successful Case-1 Detections	Successful Case-2 Detections	Total Trials
3	0.5333	24	0	45
4	0.8000	24	12	45
5	0.8000	24	12	45
6	0.8000	24	12	45
7	0.8000	24	12	45
8	0.8000	24	12	45
9	0.8000	24	12	45
10	0.8000	24	12	45
11	0.7778	23	12	45
12	0.7778	23	12	45
13	0.7333	23	10	45
14	0.7111	18	14	45
15	0.5333	13	11	45
16	0.3778	4	13	45
17	0.2444	2	9	45

Table A.6: The Probability of Successfully Detecting a Target with 1-meter Cross-sectional Diameter versus Target Depth in Waters ranging from Absorption Coefficients of $0.069m^{-1}$ to $0.109m^{-1}$

Target Depth (m)	Detection Probability	Successful Case-1 Detections	Successful Case-2 Detections	Total Trials
3	0.5333	24	0	45
4	0.8000	24	12	45
5	0.8000	24	12	45
6	0.7778	23	12	45
7	0.8000	24	12	45
8	0.8000	24	12	45
9	0.8000	24	12	45
10	0.7556	23	11	45
11	0.7556	22	12	45
12	0.5111	15	8	45
13	0.4889	9	13	45
14	0.2444	4	7	45
15	0.1778	0	8	45
16	0.0222	0	1	45
17	0.0000	0	0	45

The following four tables contain the data used to produce Figure 4.8.

Table A.7: The Probability of Successfully Detecting a 2-meter tall Target versus Target Depth in Waters ranging from Absorption Coefficients of $0.069m^{-1}$ to $0.109m^{-1}$

Target Depth (m)	Detection Probability	Successful Case-1 Detections	Successful Case-2 Detections	Total Trials
3	0.6000	27	0	45
4	0.8000	26	10	45
5	0.8000	24	12	45
6	0.7778	23	12	45
7	0.8000	24	12	45
8	0.8889	31	9	45
9	0.8444	30	8	45
10	0.8222	27	10	45
11	0.8000	28	8	45
12	0.7333	23	10	45
13	0.7111	21	11	45
14	0.6222	18	10	45
15	0.5333	14	10	45
16	0.4444	11	9	45
17	0.3556	7	9	45

Table A.8: The Probability of Successfully Detecting a 1.5-meter tall Target versus Target Depth in Waters ranging from Absorption Coefficients of $0.069m^{-1}$ to $0.109m^{-1}$

Target Depth (m)	Detection Probability	Successful Case-1 Detections	Successful Case-2 Detections	Total Trials
3	0.5778	26	0	45
4	0.8222	26	11	45
5	0.8000	25	11	45
6	0.8000	24	12	45
7	0.8000	24	12	45
8	0.8889	29	11	45
9	0.8444	27	11	45
10	0.8222	26	11	45
11	0.8000	25	11	45
12	0.7111	23	9	45
13	0.6667	19	11	45
14	0.5778	15	11	45
15	0.5111	12	11	45
16	0.4222	10	9	45
17	0.3333	6	9	45

Table A.9: The Probability of Successfully Detecting a 1-meter tall Target versus Target Depth in Waters ranging from Absorption Coefficients of 0.069m^{-1} to 0.109m^{-1}

Target Depth (m)	Detection Probability	Successful Case-1 Detections	Successful Case-2 Detections	Total Trials
3	0.5778	26	0	45
4	0.8000	25	11	45
5	0.8000	25	11	45
6	0.8000	24	12	45
7	0.8000	24	12	45
8	0.8444	27	11	45
9	0.8667	28	11	45
10	0.8000	25	11	45
11	0.7778	24	11	45
12	0.6889	22	9	45
13	0.6889	20	11	45
14	0.6444	18	11	45
15	0.5778	15	11	45
16	0.4222	10	9	45
17	0.3556	7	9	45

Table A.10: The Probability of Successfully Detecting a 0.5-meter tall Target versus Target Depth in Waters ranging from Absorption Coefficients of 0.069m^{-1} to 0.109m^{-1}

Target Depth (m)	Detection Probability	Successful Case-1 Detections	Successful Case-2 Detections	Total Trials
3	0.5778	26	0	45
4	0.8000	25	11	45
5	0.8000	24	12	45
6	0.8000	24	12	45
7	0.8000	24	12	45
8	0.8222	26	11	45
9	0.8444	25	13	45
10	0.7778	23	12	45
11	0.8000	24	12	45
12	0.7333	22	11	45
13	0.7111	20	12	45
14	0.6222	17	11	45
15	0.5333	13	11	45
16	0.4667	11	10	45
17	0.3333	7	8	45

The next six tables contain the data used to produce Figures 4.10 and 4.11.

Table A.11: The Probability of Successfully Detecting a 2-meter Target in Coastal Water with $K_d=0.08m^{-1}$

Optical Path Length (m)	Detection Probability	Successful Case-1 Detections	Successful Case-2 Detections	Total Trials
3.1058	1.0000	27	0	27
4.1411	1.0000	27	0	27
5.1764	1.0000	27	0	27
6.2117	1.0000	27	0	27
7.2469	1.0000	27	0	27
8.2822	1.0000	27	0	27
9.3175	1.0000	27	0	27
10.3528	1.0000	27	0	27
11.3880	1.0000	27	0	27
12.4233	0.9630	26	0	27
13.4586	1.0000	27	0	27
14.4939	1.0000	27	0	27
15.5291	0.8889	24	0	27
16.5644	0.8148	21	1	27
17.5997	0.9259	24	1	27
18.6350	0.7778	16	5	27
19.6702	0.0000	0	0	27
20.7055	0.0000	0	0	27
21.7408	0.0000	0	0	27
22.7761	0.0000	0	0	27
23.8114	0.0000	0	0	27
24.8466	0.0000	0	0	27
25.8819	0.0000	0	0	27

Table A.12: The Probability of Successfully Detecting a 1-meter Target in Coastal Water with $K_d=0.08m^{-1}$

Optical Path Length (m)	Detection Probability	Successful Case-1 Detections	Successful Case-2 Detections	Total Trials
3.1058	1.0000	27	0	27
4.1411	1.0000	27	0	27
5.1764	1.0000	27	0	27
6.2117	1.0000	27	0	27
7.2469	1.0000	27	0	27
8.2822	1.0000	27	0	27
9.3175	1.0000	27	0	27
10.3528	1.0000	27	0	27
11.3880	0.9259	24	1	27
12.4233	1.0000	25	2	27
13.4586	1.0000	24	3	27
14.4939	0.8519	21	2	27
15.5291	0.1852	5	0	27
16.5644	0.0000	0	0	27
17.5997	0.0000	0	0	27
18.6350	0.0000	0	0	27
19.6702	0.0000	0	0	27
20.7055	0.0000	0	0	27
21.7408	0.0000	0	0	27
22.7761	0.0000	0	0	27
23.8114	0.0000	0	0	27
24.8466	0.0000	0	0	27
25.8819	0.0000	0	0	27

Table A.13: The Probability of Successfully Detecting a 2-meter Target in Coastal Water with $K_d=0.12m^{-1}$

Optical Path Length (m)	Detection Probability	Successful Case-1 Detections	Successful Case-2 Detections	Total Trials
3.1058	1.0000	27	0	27
4.1411	1.0000	27	0	27
5.1764	1.0000	27	0	27
6.2117	1.0000	27	0	27
7.2469	1.0000	27	0	27
8.2822	1.0000	27	0	27
9.3175	1.0000	27	0	27
10.3528	1.0000	27	0	27
11.3880	1.0000	27	0	27
12.4233	0.9630	26	0	27
13.4586	0.9259	24	1	27
14.4939	0.2963	5	3	27
15.5291	0.0000	0	0	27
16.5644	0.0000	0	0	27
17.5997	0.0000	0	0	27
18.6350	0.0000	0	0	27
19.6702	0.0000	0	0	27
20.7055	0.0000	0	0	27
21.7408	0.0000	0	0	27
22.7761	0.0000	0	0	27
23.8114	0.0000	0	0	27
24.8466	0.0000	0	0	27
25.8819	0.0000	0	0	27

Table A.14: The Probability of Successfully Detecting a 1-meter Target in Coastal Water with $K_d=0.12m^{-1}$

Optical Path Length (m)	Detection Probability	Successful Case-1 Detections	Successful Case-2 Detections	Total Trials
3.1058	1.0000	27	0	27
4.1411	1.0000	27	0	27
5.1764	1.0000	27	0	27
6.2117	1.0000	27	0	27
7.2469	1.0000	27	0	27
8.2822	1.0000	27	0	27
9.3175	1.0000	27	0	27
10.3528	0.9259	25	0	27
11.3880	0.7407	16	4	27
12.4233	0.0000	0	0	27
13.4586	0.0000	0	0	27
14.4939	0.0000	0	0	27
15.5291	0.0000	0	0	27
16.5644	0.0000	0	0	27
17.5997	0.0000	0	0	27
18.6350	0.0000	0	0	27
19.6702	0.0000	0	0	27
20.7055	0.0000	0	0	27
21.7408	0.0000	0	0	27
22.7761	0.0000	0	0	27
23.8114	0.0000	0	0	27
24.8466	0.0000	0	0	27
25.8819	0.0000	0	0	27

Table A.15: The Probability of Successfully Detecting a 2-meter Target in Coastal Water with $K_d=0.25m^{-1}$

Optical Path Length (m)	Detection Probability	Successful Case-1 Detections	Successful Case-2 Detections	Total Trials
3.1058	1.0000	27	0	27
4.1411	1.0000	27	0	27
5.1764	1.0000	27	0	27
6.2117	1.0000	27	0	27
7.2469	1.0000	27	0	27
8.2822	1.0000	27	0	27
9.3175	0.0000	0	0	27
10.3528	0.0000	0	0	27
11.3880	0.0000	0	0	27
12.4233	0.0000	0	0	27
13.4586	0.0000	0	0	27
14.4939	0.0000	0	0	27
15.5291	0.0000	0	0	27
16.5644	0.0000	0	0	27
17.5997	0.0000	0	0	27
18.6350	0.0000	0	0	27
19.6702	0.0000	0	0	27
20.7055	0.0000	0	0	27
21.7408	0.0000	0	0	27
22.7761	0.0000	0	0	27
23.8114	0.0000	0	0	27
24.8466	0.0000	0	0	27
25.8819	0.0000	0	0	27

Table A.16: The Probability of Successfully Detecting a 1-meter Target in Coastal Water with $K_d=0.25m^{-1}$

Optical Path Length (m)	Detection Probability	Successful Case-1 Detections	Successful Case-2 Detections	Total Trials
3.1058	1.0000	27	0	27
4.1411	0.9630	26	0	27
5.1764	0.8889	24	0	27
6.2117	0.0000	0	0	27
7.2469	0.0000	0	0	27
8.2822	0.0000	0	0	27
9.3175	0.0000	0	0	27
10.3528	0.0000	0	0	27
11.3880	0.0000	0	0	27
12.4233	0.0000	0	0	27
13.4586	0.0000	0	0	27
14.4939	0.0000	0	0	27
15.5291	0.0000	0	0	27
16.5644	0.0000	0	0	27
17.5997	0.0000	0	0	27
18.6350	0.0000	0	0	27
19.6702	0.0000	0	0	27
20.7055	0.0000	0	0	27
21.7408	0.0000	0	0	27
22.7761	0.0000	0	0	27
23.8114	0.0000	0	0	27
24.8466	0.0000	0	0	27
25.8819	0.0000	0	0	27

The next twelve tables contain the data used to produce Figures 4.12, 4.13 and 4.14

Table A.17: The Probability of Successfully Detecting a 1-meter Target using a 20-mrad receiver FOV in Coastal Water with K_d=0.08m^{-1}

Optical Path Length (m)	Detection Probability	Successful Case-1 Detections	Successful Case-2 Detections	Total Trials
3.1058	1.0000	27	0	27
4.1411	1.0000	27	0	27
5.1764	1.0000	27	0	27
6.2117	1.0000	27	0	27
7.2469	1.0000	27	0	27
8.2822	1.0000	27	0	27
9.3175	1.0000	27	0	27
10.3528	0.9630	25	1	27
11.3880	0.9630	25	1	27
12.4233	0.9630	23	3	27
13.4586	0.7407	20	0	27
14.4939	0.0000	0	0	27
15.5291	0.0000	0	0	27
16.5644	0.0000	0	0	27
17.5997	0.0000	0	0	27
18.6350	0.0000	0	0	27
19.6702	0.0000	0	0	27
20.7055	0.0000	0	0	27
21.7408	0.0000	0	0	27
22.7761	0.0000	0	0	27
23.8114	0.0000	0	0	27
24.8466	0.0000	0	0	27
25.8819	0.0000	0	0	27

Table A.18: The Probability of Successfully Detecting a 1-meter Target using a 30-mrad receiver FOV in Coastal Water with K_d=0.08m^{-1}

Optical Path Length (m)	Detection Probability	Successful Case-1 Detections	Successful Case-2 Detections	Total Trials
3.1058	1.0000	27	0	27
4.1411	1.0000	27	0	27
5.1764	1.0000	27	0	27
6.2117	1.0000	27	0	27
7.2469	1.0000	27	0	27
8.2822	1.0000	27	0	27
9.3175	1.0000	27	0	27
10.3528	0.9630	26	0	27
11.3880	0.9630	25	1	27
12.4233	0.9259	23	2	27
13.4586	0.8889	17	7	27
14.4939	0.6667	15	3	27
15.5291	0.0000	0	0	27
16.5644	0.0000	0	0	27
17.5997	0.0000	0	0	27
18.6350	0.0000	0	0	27
19.6702	0.0000	0	0	27
20.7055	0.0000	0	0	27
21.7408	0.0000	0	0	27
22.7761	0.0000	0	0	27
23.8114	0.0000	0	0	27
24.8466	0.0000	0	0	27
25.8819	0.0000	0	0	27

Table A.19: The Probability of Successfully Detecting a 1-meter Target using a 40-mrad receiver FOV in Coastal Water with K_d=0.08m^{-1}

Optical Path Length (m)	Detection Probability	Successful Case-1 Detections	Successful Case-2 Detections	Total Trials
3.1058	1.0000	27	0	27
4.1411	1.0000	27	0	27
5.1764	1.0000	27	0	27
6.2117	1.0000	27	0	27
7.2469	1.0000	27	0	27
8.2822	1.0000	27	0	27
9.3175	1.0000	27	0	27
10.3528	1.0000	27	0	27
11.3880	0.9259	24	1	27
12.4233	1.0000	25	2	27
13.4586	1.0000	24	3	27
14.4939	0.8519	21	2	27
15.5291	0.1852	5	0	27
16.5644	0.0000	0	0	27
17.5997	0.0000	0	0	27
18.6350	0.0000	0	0	27
19.6702	0.0000	0	0	27
20.7055	0.0000	0	0	27
21.7408	0.0000	0	0	27
22.7761	0.0000	0	0	27
23.8114	0.0000	0	0	27
24.8466	0.0000	0	0	27
25.8819	0.0000	0	0	27

Table A.20: The Probability of Successfully Detecting a 1-meter Target using a 50-mrad receiver FOV in Coastal Water with K_d=0.08m^{-1}

Optical Path Length (m)	Detection Probability	Successful Case-1 Detections	Successful Case-2 Detections	Total Trials
3.1058	1.0000	27	0	27
4.1411	1.0000	27	0	27
5.1764	1.0000	27	0	27
6.2117	1.0000	27	0	27
7.2469	0.9630	26	0	27
8.2822	1.0000	27	0	27
9.3175	1.0000	27	0	27
10.3528	0.9630	26	0	27
11.3880	0.9630	26	0	27
12.4233	0.9630	26	0	27
13.4586	1.0000	25	2	27
14.4939	0.9259	24	1	27
15.5291	0.7037	13	6	27
16.5644	0.0000	0	0	27
17.5997	0.0000	0	0	27
18.6350	0.0000	0	0	27
19.6702	0.0000	0	0	27
20.7055	0.0000	0	0	27
21.7408	0.0000	0	0	27
22.7761	0.0000	0	0	27
23.8114	0.0000	0	0	27
24.8466	0.0000	0	0	27
25.8819	0.0000	0	0	27

Table A.21: The Probability of Successfully Detecting a 1-meter Target using a 20-mrad receiver FOV in Coastal Water with K_d=0.12m^{-1}

Optical Path Length (m)	Detection Probability	Successful Case-1 Detections	Successful Case-2 Detections	Total Trials
3.1058	1.0000	27	0	27
4.1411	1.0000	27	0	27
5.1764	1.0000	27	0	27
6.2117	0.9259	25	0	27
7.2469	1.0000	25	2	27
8.2822	0.9630	25	1	27
9.3175	0.9630	21	5	27
10.3528	0.0000	0	0	27
11.3880	0.0000	0	0	27
12.4233	0.0000	0	0	27
13.4586	0.0000	0	0	27
14.4939	0.0000	0	0	27
15.5291	0.0000	0	0	27
16.5644	0.0000	0	0	27
17.5997	0.0000	0	0	27
18.6350	0.0000	0	0	27
19.6702	0.0000	0	0	27
20.7055	0.0000	0	0	27
21.7408	0.0000	0	0	27
22.7761	0.0000	0	0	27
23.8114	0.0000	0	0	27
24.8466	0.0000	0	0	27
25.8819	0.0000	0	0	27

Table A.22: The Probability of Successfully Detecting a 1-meter Target using a 30-mrad receiver FOV in Coastal Water with K_d=0.12m^{-1}

Optical Path Length (m)	Detection Probability	Successful Case-1 Detections	Successful Case-2 Detections	Total Trials
3.1058	1.0000	27	0	27
4.1411	1.0000	27	0	27
5.1764	1.0000	27	0	27
6.2117	1.0000	27	0	27
7.2469	0.9630	24	2	27
8.2822	1.0000	26	1	27
9.3175	1.0000	24	3	27
10.3528	0.7778	18	3	27
11.3880	0.0000	0	0	27
12.4233	0.0000	0	0	27
13.4586	0.0000	0	0	27
14.4939	0.0000	0	0	27
15.5291	0.0000	0	0	27
16.5644	0.0000	0	0	27
17.5997	0.0000	0	0	27
18.6350	0.0000	0	0	27
19.6702	0.0000	0	0	27
20.7055	0.0000	0	0	27
21.7408	0.0000	0	0	27
22.7761	0.0000	0	0	27
23.8114	0.0000	0	0	27
24.8466	0.0000	0	0	27
25.8819	0.0000	0	0	27

Table A.23: The Probability of Successfully Detecting a 1-meter Target using a 40-mrad receiver FOV in Coastal Water with K_d=0.12m^{-1}

Optical Path Length (m)	Detection Probability	Successful Case-1 Detections	Successful Case-2 Detections	Total Trials
3.1058	1.0000	27	0	27
4.1411	1.0000	27	0	27
5.1764	1.0000	27	0	27
6.2117	1.0000	27	0	27
7.2469	1.0000	27	0	27
8.2822	1.0000	27	0	27
9.3175	1.0000	27	0	27
10.3528	0.9259	25	0	27
11.3880	0.7407	16	4	27
12.4233	0.0000	0	0	27
13.4586	0.0000	0	0	27
14.4939	0.0000	0	0	27
15.5291	0.0000	0	0	27
16.5644	0.0000	0	0	27
17.5997	0.0000	0	0	27
18.6350	0.0000	0	0	27
19.6702	0.0000	0	0	27
20.7055	0.0000	0	0	27
21.7408	0.0000	0	0	27
22.7761	0.0000	0	0	27
23.8114	0.0000	0	0	27
24.8466	0.0000	0	0	27
25.8819	0.0000	0	0	27

Table A.24: The Probability of Successfully Detecting a 1-meter Target using a 50-mrad receiver FOV in Coastal Water with K_d=0.12m^{-1}

Optical Path Length (m)	Detection Probability	Successful Case-1 Detections	Successful Case-2 Detections	Total Trials
3.1058	1.0000	27	0	27
4.1411	1.0000	27	0	27
5.1764	1.0000	27	0	27
6.2117	1.0000	27	0	27
7.2469	1.0000	27	0	27
8.2822	1.0000	27	0	27
9.3175	1.0000	27	0	27
10.3528	0.9630	25	1	27
11.3880	0.8889	21	3	27
12.4233	0.0000	0	0	27
13.4586	0.0000	0	0	27
14.4939	0.0000	0	0	27
15.5291	0.0000	0	0	27
16.5644	0.0000	0	0	27
17.5997	0.0000	0	0	27
18.6350	0.0000	0	0	27
19.6702	0.0000	0	0	27
20.7055	0.0000	0	0	27
21.7408	0.0000	0	0	27
22.7761	0.0000	0	0	27
23.8114	0.0000	0	0	27
24.8466	0.0000	0	0	27
25.8819	0.0000	0	0	27

Table A.25: The Probability of Successfully Detecting a 1-meter Target using a 20-mrad receiver FOV in Coastal Water with K_d=0.25m^{-1}

Optical Path Length (m)	Detection Probability	Successful Case-1 Detections	Successful Case-2 Detections	Total Trials
3.1058	0.8889	24	0	27
4.1411	0.6667	17	1	27
5.1764	0.0000	0	0	27
6.2117	0.0000	0	0	27
7.2469	0.0000	0	0	27
8.2822	0.0000	0	0	27
9.3175	0.0000	0	0	27
10.3528	0.0000	0	0	27
11.3880	0.0000	0	0	27
12.4233	0.0000	0	0	27
13.4586	0.0000	0	0	27
14.4939	0.0000	0	0	27
15.5291	0.0000	0	0	27
16.5644	0.0000	0	0	27
17.5997	0.0000	0	0	27
18.6350	0.0000	0	0	27
19.6702	0.0000	0	0	27
20.7055	0.0000	0	0	27
21.7408	0.0000	0	0	27
22.7761	0.0000	0	0	27
23.8114	0.0000	0	0	27
24.8466	0.0000	0	0	27
25.8819	0.0000	0	0	27

Table A.26: The Probability of Successfully Detecting a 1-meter Target using a 30-mrad receiver FOV in Coastal Water with K_d=0.25m^{-1}

Optical Path Length (m)	Detection Probability	Successful Case-1 Detections	Successful Case-2 Detections	Total Trials
3.1058	1.0000	27	0	27
4.1411	0.9259	25	0	27
5.1764	0.6296	15	2	27
6.2117	0.0000	0	0	27
7.2469	0.0000	0	0	27
8.2822	0.0000	0	0	27
9.3175	0.0000	0	0	27
10.3528	0.0000	0	0	27
11.3880	0.0000	0	0	27
12.4233	0.0000	0	0	27
13.4586	0.0000	0	0	27
14.4939	0.0000	0	0	27
15.5291	0.0000	0	0	27
16.5644	0.0000	0	0	27
17.5997	0.0000	0	0	27
18.6350	0.0000	0	0	27
19.6702	0.0000	0	0	27
20.7055	0.0000	0	0	27
21.7408	0.0000	0	0	27
22.7761	0.0000	0	0	27
23.8114	0.0000	0	0	27
24.8466	0.0000	0	0	27
25.8819	0.0000	0	0	27

Table A.27: The Probability of Successfully Detecting a 1-meter Target using a 40-mrad receiver FOV in Coastal Water with K_d=0.25m^{-1}

Optical Path Length (m)	Detection Probability	Successful Case-1 Detections	Successful Case-2 Detections	Total Trials
3.1058	1.0000	27	0	27
4.1411	0.9630	26	0	27
5.1764	0.8889	24	0	27
6.2117	0.0000	0	0	27
7.2469	0.0000	0	0	27
8.2822	0.0000	0	0	27
9.3175	0.0000	0	0	27
10.3528	0.0000	0	0	27
11.3880	0.0000	0	0	27
12.4233	0.0000	0	0	27
13.4586	0.0000	0	0	27
14.4939	0.0000	0	0	27
15.5291	0.0000	0	0	27
16.5644	0.0000	0	0	27
17.5997	0.0000	0	0	27
18.6350	0.0000	0	0	27
19.6702	0.0000	0	0	27
20.7055	0.0000	0	0	27
21.7408	0.0000	0	0	27
22.7761	0.0000	0	0	27
23.8114	0.0000	0	0	27
24.8466	0.0000	0	0	27
25.8819	0.0000	0	0	27

Table A.28: The Probability of Successfully Detecting a 1-meter Target using a 50-mrad receiver FOV in Coastal Water with K_d=0.25m^{-1}

Optical Path Length (m)	Detection Probability	Successful Case-1 Detections	Successful Case-2 Detections	Total Trials
3.1058	1.0000	27	0	27
4.1411	0.9259	25	0	27
5.1764	0.8148	20	2	27
6.2117	0.0370	1	0	27
7.2469	0.0000	0	0	27
8.2822	0.0000	0	0	27
9.3175	0.0000	0	0	27
10.3528	0.0000	0	0	27
11.3880	0.0000	0	0	27
12.4233	0.0000	0	0	27
13.4586	0.0000	0	0	27
14.4939	0.0000	0	0	27
15.5291	0.0000	0	0	27
16.5644	0.0000	0	0	27
17.5997	0.0000	0	0	27
18.6350	0.0000	0	0	27
19.6702	0.0000	0	0	27
20.7055	0.0000	0	0	27
21.7408	0.0000	0	0	27
22.7761	0.0000	0	0	27
23.8114	0.0000	0	0	27
24.8466	0.0000	0	0	27
25.8819	0.0000	0	0	27

REFERENCES

[1] Yang, E. and LaRocque, P., "SHOALS Object Detection," *International Hydrographic Review*, pp. 24-36, (2010).

[2] Gordon, H.R., "Interpretation of Airborne Ocean Lidar: Effects of Multiple Scattering," *Applied Optics*, vol. 21(16), pp. 2996-3001, (1982).

[3] Guenther, G.C., "Airborne Laser Hydrography: System Design and Performance Factors", *NOAA Professional Paper Series*, *National Ocean Service 1*, (1985).

[4] Petzold, T.J., "Volume Scattering Functions for Selected Ocean Waters," *Technical Report SIO, Scripps Institute of Oceanography*, pp. 72-78, (1972).

[5] Dolin, L.S., Levin, I.M., Kopelevich, O.V., Feigels, V.I., "Few-Parameter Models of Light Field at the Sea and Integral Parameters of Phase Functions of Water." *Izv. AN SSSR. Fizika atmosfery i okeana* (Izvestiya, Atmospheric and Oceanic Physics), vol.24(11), pp. 1217-1222, (1988).

[6] Kopelevich, O.V., "Small-parameter model of optical properties of sea water," *Ocean Opt., 1, Physical Ocean Optics*, ed. A.S. Monin, Nauka (in Russian), (1983).

[7] Sokolov, A., Chami, M., Dmitriev, E., and Khomenko, G., "Parameterization of Volume Scattering Function of Coastal Waters Based on the Statistical Approach," *Optics Express*, vol.18(5), pp. 4615-4636, (2010).

[8] Guenther, G.C., Cunningham, A.G., LaRocque, P.E., and Reid, D.J., "Meeting the Accuracy Challenge in Airborne Lidar Bathymetry", *Proceedings of 20th Workshop on Lidar Remote Sensing of Land and Sea*, pp.1-27, (2000).

[9] Tuell, G.H., and Park, J.Y., "Use of SHOALS Bottom Reflectance Images to Constrain the Inversion of a Hyperspectral Radiative Transfer Model," *Proc. SPIE, Laser Radar Technology and Applications IX*, vol. 5412, pp. 185-193, (2004).

[10] Tuell, G.H., Park., J.Y., Aitken, J., Ramnath, V., Feygels, V., Guenther, G.C., and Kopilevech,Y., "SHOALS-enabled 3D Benthic Mapping", *Proc. SPIE 5806, Algorithms and Technologies for Multispectral, Hyperspectral, and Ultraspectral Imagery XI*, pp. 816-826, (2005).

[11] Yang, E., Larocque, P., Guenther, G., Reid, D., Pan, W., and Francis, K, "Shallow Water Depth Extraction – Progress and Challenges", *2007 Hydrographic Conference,* pp. 1-13, (2007).

[12] Tuell, G.H, Barbor, K., and Wozencraft, J.M., "Overview of the Coastal Zone Mapping and Imaging Lidar (CZMIL): A New Multi-sensor Airborne Mapping Systems for the U.S. Army Corps of Engineers," *Proc. SPIE, Algorithms and Technologies for Multispectral, Hyperspectal, and Ultraspectral Imagery XVI,* vol. 7695, (2010).

[13] The Compact Hydrographic and Rapid Total Survey (CHARTS) system, from the website of the Joint Airborne Lidar Bathymetric Technical Center of Expertise: http://shoals.sam.usace.army.mil/Charts.aspx

[14] Pierce, J.W., Fuchs, E., Nelson, S., Feygels, V., and Tuell, G.H., "Development of a Novel Laser System for the CZMIL Lidar", *Proc. SPIE, Algorithms and Technologies for Multispectral, Hyperspectral, and Ultraspectral Imagery XVI,* vol. 7695, (2010).

[15] Fuchs, E., and Mathur, A., "Utilizing Circular Scanning in the CZMIL system", *Proc. SPIE, Algorithms and Technologies for Multispectral, Hyperspectral, and Ultraspectral Imagery XVI,* vol. 7695, (2010).

[16] Payment, A., Feygels, V., Fuchs, E., and Tuell, G.H., "Proposed Lidar Receiver Architecture of the CZMIL System", *Proc. SPIE, Algorithms and Technologies for Multispectral, Hyperspectral, and Ultraspectral Imagery XVI,* vol. 7695, (2010).

[17] Kopilevich, Y.I, Feygels, V.I, Tuell, G.H.,and Surkov, A., "Measurement of Ocean Water Optical Properties and Seafloor Reflectance with Scanning Hydrographic Operational Airborne Lidar Survey (SHOALS): I. Theoretical Background," *Proc. SPIE, Remote Sensing of the Coastal Oceanic Environment,* vol. 5885, (2005).

[18] Tuell, G.H., Feygels, V.I., Kopilevich, Y., Weidemann, A.D., Cunningham, A.G., Mani, R., Podoba, V., Ramnath, V., Park, J.Y., and Aitken, J., "Measurement of Ocean Water Optical Properties and Seafloor Reflectance with Scanning Hydrographic Operational Airborne Lidar Survey (SHOALS): II. Practical Results and Comparison with Independent Data," *Proc. SPIE, Remote Sensing of the Coastal Oceanic Environment*, vol. 5885, (2005).

[19] Ramnath, V., Feygels, V., Kopilevich, Y., Park, J.Y., and Tuell, G.H., "Predicted Bathymetric Lidar Performance of Costal Zone Mapping and Imaging Lidar

(CZMIL)", *Proc. SPIE, Algorithms and Technologies for Multispectral, Hyperspectral, and Ultraspectral Imagery XVI,* vol. 7695, (2010).

[20] Lake, T. K., Kemp, A. J., Friel, G. J., & Sinclair, B. D., "Comparison between Nd:YAG and Nd:YVO4 as gain media for a single-frequency micro-laser," *Inspec, CLEO,* p.463, (2000).

[21] Jerlov, N.G., Marine Optics. Amsterdam: Elsevier Scientific Pub. Co. (1976).

[22] Petri, K.J., "Laser Radar Reflectance of Chesapeake Bay Waters as a Function of Wind Speed," IEEE Trans. Geoscience Electronics, vol. 15(2), pp. 87-96, (1977).

[23] Tuell, G.H. and Park J.Y., "Use of SHOALS Bottom Reflectance Images to Constrain the Inversion of a Hyperspectral Radiative Transfer Model," *Proc. SPIE Laser Radar and Technology Applications IX*, vol. 5412, pp. 185-193., (2004).

[24] Guenther, G.C., and Thomas, R.W.L., "Prediction and Correction of Propagation-Induced Depth Measurement Biases plus Signal Attenuation and Beam Spreading for Airborne Laser Hydrography," *NOAA Technical Report*, nos. 106, cgs 2, p. 112, (1984).

[25] Kopilevich, Y., Tuell, G., Feygels, V., "Aspects of Resolution and Target Detection," *6th Annual Airborne Coastal Mapping and Charting Workshop*, (2005).

[26] Kopilevich, Y.I, and Surkov, A.G. "Mathematical Modeling of the Input Signals of Oceanological Lidars," *Journal of Opt. Technology*, vol. 75(5), pp. 321-326, (2008).

[27] Feygels, V.I., Kopilevich, Y.I, Surkov, A., and Yungel, J.K., "Airborne lidar system with variable field-of-view receiver for water optical properties measurement," *Proc. SPIE, Ocean Remote Sensing and Imaging II*, vol. 5155, pp. 12-21, (2003).

[28] Feigels, V.I, Evans, B., Feygels, L., Guenther, G.C., and Kopilevich, Y.I, "Prediction of bathymetric lidar performance with Ocean Scientific 2001 simulation code", *Proc. SPIE Ocean Optics: Remote Sensing and Underwater Imaging*, vol. 4488, pp. 61-70, (2002).

[29] Feygels, V.I., Wright, C.W., Kopilevich, Y.I, and Surkov, A., "Narrow field-of-view bathymetric lidar: theory and field test", *Proc. SPIE Ocean Remote Sensing and Imaging II*, Vol. 155, pp.1-11, (2003).

[30] Mobley, C.D., Light and Water: Radiative Transfer in Natural Waters. San Diego: Academic Press, (1994).

[31] International Hydrographic Organization, IHO Standards for Hydgrogaphic Surveys, Special Publication No. 44, 4th Edition, (1998).

[32] Guenther, G.C., Eisler, T.J. Riley, J.L. and Perez, S.W., "Obstruction detection and data decimation for airborne laser hydrography," *Proceedings Canadian Hydrographic Conference*, pp. 51-63, (1996).

[33] Cossio, T.K., Slatton, K.C., Carter, W.E., Shrestha, K.Y., Harding, D., "Predicting Small Target Detection Performance of Low-SNR Airborne Lidar", *IEEE Jounral of Selected Topics in Applied Earth Observations and Remote Sensing*, vol. 3(4), pp. 672-688, (2010).

[34] J. Wozencraft, "Requirements for the Coastal Zone Mapping and Imaging Lidar (CZMIL)," *Proc. SPIE Algorithms and Technologies for Multispectral, Hyperspectral, and Ultraspectral Imagery XVI,* vol. 7695, in press, (2010).

[35] Clarkson, E., Hurt. J., Zutty, J., Skeels, C., Parise, B., and Rohling, G., "Supporting Robust Performance Analysis with the Test Matrix Tool Framework", To appear in the *Proceedings of ACM Conference on Principles of Advanced Discrete Simulations (PADS),* (2013).